

# Testing Lepton Universality using One-Prong Hadronic Tau Decays

by

John Stephen White

B.Sc., University of Victoria, 1991.

M.Sc., University of Victoria, 1994.

A Dissertation Submitted in Partial Fulfillment of the  
Requirements for the Degree of  
DOCTOR OF PHILOSOPHY

in the Department of Physics and Astronomy.

We accept this thesis as conforming  
to the required standard.

---

*Dr. R. Sobie, Supervisor (Department of Physics and Astronomy)*

---

*Dr. M. Lefebvre, Supervisor (Department of Physics and Astronomy)*

---

*Dr. R. Keeler, Departmental Member (Department of Physics and Astronomy)*

---

*Dr. D. Harrington, Outside Member (Department of Chemistry)*

---

*Dr. J. Prentice, External Examiner*

© John White, 1998  
University of Victoria.

*All rights reserved. Thesis may not be reproduced in whole or in part,  
by photocopy or other means, without the permission of the author.*

Supervisor: Dr. R. Sobie and Dr. M. Lefebvre

## Abstract

The branching ratios of the  $\tau^- \rightarrow h^- \nu_\tau$ ,  $\tau^- \rightarrow h^- \pi^0 \nu_\tau$  and  $\tau^- \rightarrow h^- \geq 2\pi^0 \nu_\tau$  decays have been measured using the 1991-1995 data recorded with the OPAL detector at LEP. These branching ratios are measured simultaneously using three selection criteria and found to be  $B_{\tau^- \rightarrow h^- \nu_\tau} = (11.98 \pm 0.13 \pm 0.16) \%$ ,  $B_{\tau^- \rightarrow h^- \pi^0 \nu_\tau} = (25.89 \pm 0.17 \pm 0.29) \%$  and  $B_{\tau^- \rightarrow h^- \geq 2\pi^0 \nu_\tau} = (9.91 \pm 0.31 \pm 0.27) \%$  where the first error is statistical and the second is systematic. These results are in agreement with the current published world average measurements and improve on previous OPAL measurements. The strengths of the weak charged current coupling constants for  $\tau$ 's and muons was tested and their ratio was found to be  $g_\tau/g_\mu = 1.018 \pm 0.010$ .

Examiners:

---

*Dr. R. Sobie, Supervisor (Department of Physics and Astronomy)*

---

*Dr. M. Lefebvre, Supervisor (Department of Physics and Astronomy)*

---

*Dr. R. Keeler, Departmental Member (Department of Physics and Astronomy)*

---

*Dr. D. Harrington, Outside Member (Department of Chemistry)*

---

*Dr. J. Prentice, External Examiner*

# Contents

<b>Abstract</b>	<b>ii</b>
<b>Acknowledgements</b>	<b>xii</b>
<b>1 Introduction</b>	<b>1</b>
<b>2 The weak interaction and the <math>\tau</math> lepton</b>	<b>9</b>
2.1 The weak interaction . . . . .	9
2.2 $\tau^- \rightarrow \pi^- \nu_\tau$ and $\tau^- \rightarrow K^- \nu_\tau$ decay widths . . . . .	13
2.3 $\tau^- \rightarrow \pi^- \pi^0 \nu_\tau$ decay width . . . . .	16
2.4 Lepton universality . . . . .	17
<b>3 Experimental equipment</b>	<b>21</b>
3.1 The LEP accelerator . . . . .	21
3.1.1 Injection chain . . . . .	21
3.1.2 LEP ring . . . . .	23
3.2 The OPAL detector . . . . .	24
3.2.1 The inner tracking detectors . . . . .	26
3.2.2 Solenoid magnet and time of flight detector . . . . .	29
3.2.3 The calorimeters . . . . .	30

3.2.4	The muon chambers . . . . .	32
3.2.5	Luminosity monitors . . . . .	33
3.2.6	Data acquisition System . . . . .	33
3.2.7	OPAL performance . . . . .	34
<b>4</b>	<b>Selection of <math>\tau^+\tau^-</math> events</b>	<b>36</b>
4.1	OPAL data and Monte Carlo . . . . .	36
4.2	Selection of $e^+e^- \rightarrow \tau^+\tau^-$ events . . . . .	38
<b>5</b>	<b>Selection of one-prong <math>\tau</math>-decays</b>	<b>46</b>
5.1	One-prong definition . . . . .	46
5.2	One-prong selection . . . . .	47
5.3	Results . . . . .	48
<b>6</b>	<b><math>\pi^0</math> Identification</b>	<b>51</b>
6.1	Fine clustering algorithm . . . . .	52
6.2	Charged track-fine cluster matching . . . . .	53
6.3	Monte Carlo optimization . . . . .	53
6.3.1	Charged track corrections . . . . .	54
6.3.2	Energy smearing . . . . .	55
6.3.3	$E/p$ variable . . . . .	55
6.4	Neutral electromagnetic clusters . . . . .	56
6.5	$\pi^0$ topologies . . . . .	58
6.6	$\pi^0$ identification algorithm . . . . .	60
<b>7</b>	<b>Background rejection</b>	<b>66</b>
7.1	$\tau$ background rejection . . . . .	66

7.2	Estimation of $\tau$ backgrounds . . . . .	69
7.3	Background results . . . . .	70
<b>8</b>	<b>Results</b>	<b>74</b>
8.1	Branching ratio calculations . . . . .	74
8.1.1	Branching ratio for a single decay channel . . . . .	74
8.1.2	Branching ratio for multiple decay channels . . . . .	75
8.2	Results . . . . .	79
8.3	Systematic errors . . . . .	80
8.3.1	Monte Carlo systematic errors . . . . .	81
8.3.2	Instrumental systematic errors . . . . .	82
<b>9</b>	<b>Discussion</b>	<b>85</b>
<b>10</b>	<b>Conclusions</b>	<b>90</b>
<b>A</b>	<b>Muon geometry cuts</b>	<b>96</b>
<b>B</b>	<b>Background estimate</b>	<b>98</b>
B.1	$\tau^- \rightarrow e^- \bar{\nu}_e \nu_\tau$ background correction factor . . . . .	98
B.2	$\tau^- \rightarrow \mu^- \bar{\nu}_\mu \nu_\tau$ background correction factor . . . . .	100
B.3	$K_L^0$ backgrounds . . . . .	105
<b>C</b>	<b>Bias factor calculation</b>	<b>108</b>
<b>D</b>	<b>Statistical correlations</b>	<b>113</b>
<b>E</b>	<b>Error on inverse matrix</b>	<b>115</b>

<b>F</b>	<b>Cut variations</b>	<b>119</b>
<b>G</b>	<b>Anode plane effects</b>	<b>121</b>

# List of Figures

1.1	Couplings for each interaction in the Standard Model. . . . .	4
1.2	The tree-level Feynman diagrams for $\tau^- \rightarrow e^- \bar{\nu}_e \nu_\tau$ and $\tau^- \rightarrow \mu^- \bar{\nu}_\mu \nu_\tau$ decays. . . . .	7
2.1	The tree-level Feynman diagram for the $\tau^- \rightarrow \pi^- \nu_\tau$ decay. . . . .	14
2.2	The tree-level Feynman diagram for the $\tau^- \rightarrow \pi^- \pi^0 \nu_\tau$ decay. . . . .	17
2.3	The tree-level Feynman diagrams for the $\tau^- \rightarrow \pi^- \nu_\tau$ , $\tau^- \rightarrow K^- \nu_\tau$ , $\pi^- \rightarrow \mu^- \bar{\nu}_\mu$ and $K^- \rightarrow \mu^- \bar{\nu}_\mu$ decays. . . . .	18
3.1	Schematic diagram of the injector chain and LEP ring at CERN in Geneva, Switzerland. . . . .	22
3.2	Cut away drawing of the OPAL detector showing the major subdetector components. . . . .	25
3.3	Cut away drawing of the inner detector showing the arrangement of the major components. . . . .	27
3.4	The integrated luminosity collected by the OPAL detector as a function of time. . . . .	35
4.1	A schematic picture of the decay $e^+e^- \rightarrow \tau^+\tau^-$ where the $\tau^-$ decays to $\pi^- \nu_\tau$ and the $\tau^+$ decays to $e^+ \nu_e \bar{\nu}_\tau$ . . . . .	39

5.1	Conversion vertex radius of identified $e^+e^-$ pairs in good one-prong events. . . . .	49
5.2	The number of tracks in one-prong jets. . . . .	50
6.1	The energy of clusters unassociated to a charged track after all corrections are made. . . . .	56
6.2	$E/p$ distribution for events selected as good one-prongs. . . . .	57
6.3	The distribution of the number of neutral clusters per jet for one-prong selected jets. . . . .	58
6.4	Energy of the clusters identified as originating from radiative photons. . . . .	59
6.5	The three $\pi^0$ topologies considered in this analysis. . . . .	60
6.6	The fraction of $\pi^0$ 's that form one or two electromagnetic calorimeter clusters. . . . .	61
6.7	The $\pi^0$ mass distribution, for jets with two neutral clusters, in data and Monte Carlo. . . . .	62
6.8	The number of $\pi^0$ 's found in each one-prong jet and the type of $\pi^0$ 's found in all one-prong jets. . . . .	64
6.9	The energy distribution of reconstructed $\pi^0$ 's in the $\tau^- \rightarrow h^- \pi^0 \nu_\tau$ and $\tau^- \rightarrow h^- \geq 2\pi^0 \nu_\tau$ selections. . . . .	65
7.1	The $E/p$ distribution for $0\pi^0$ selected jets. . . . .	67
7.2	The acoplanarity distribution for $\tau^- \rightarrow h^- \nu_\tau$ selected jets in events where the primary track in each jet has $p > 30$ GeV. . . . .	68
7.3	The invariant mass distribution of jets identified as $\tau^- \rightarrow h^- \pi^0 \nu_\tau$ and $\tau^- \rightarrow h^- \geq 2\pi^0 \nu_\tau$ . . . . .	72



7.4	The $dE/dx$ distribution used to measure the $\tau^- \rightarrow e^- \bar{\nu}_e \nu_\tau$ background in the $\tau^- \rightarrow h^- \pi^0 \nu_\tau$ sample. . . . .	73
9.1	The branching ratios for the $\tau^- \rightarrow h^- \nu_\tau$ and $\tau^- \rightarrow h^- \pi^0 \nu_\tau$ decay modes for this work compared with previous measurements. . . . .	86
9.2	The $\tau^- \rightarrow h^- \nu_\tau$ branching ratio plotted against the tau lifetime. . . . .	87
B.1	The $dE/dx$ distributions used to measure the $\tau^- \rightarrow e^- \bar{\nu}_e \nu_\tau$ background in the $\tau^- \rightarrow h^- \nu_\tau$ and $\tau^- \rightarrow h^- \geq 2\pi^0 \nu_\tau$ samples. . . . .	99
B.2	MB response to the muon control sample used to estimate the $\tau^- \rightarrow \mu^- \bar{\nu}_\mu \nu_\tau$ correction factor in the $\tau^- \rightarrow h^- \nu_\tau$ sample. . . . .	101
B.3	The number of muon barrel layers hit for each of the $\tau^- \rightarrow h^- \pi^0 \nu_\tau$ hadron and muon samples. . . . .	104
B.4	The $\tau^- \rightarrow h^- \nu_\tau$ control sample distributions. . . . .	107
E.1	The individual elements of the inverse efficiency matrix as calculated from the modified efficiency matrix. . . . .	117
F.1	The $\tau^- \rightarrow h^- \nu_\tau$ , $\tau^- \rightarrow h^- \pi^0 \nu_\tau$ and $\tau^- \rightarrow h^- \geq 2\pi^0 \nu_\tau$ branching ratios as a function of the one-cluster $\pi^0$ energy cut. . . . .	120
F.2	The $\tau^- \rightarrow h^- \nu_\tau$ , $\tau^- \rightarrow h^- \pi^0 \nu_\tau$ and $\tau^- \rightarrow h^- \geq 2\pi^0 \nu_\tau$ branching ratios as a function of the two-cluster $\pi^0$ energy cut. . . . .	120
G.1	The $\phi$ coordinate of all charge signed primary tracks with in each CJ sector in each sample. . . . .	122

# List of Tables

1.1	Leptons and quarks arranged in generations of increasing mass. . . . .	2
1.2	Bosons that mediate the forces of the Standard Model. . . . .	3
2.1	The first generation of fermions in the Standard Model arranged in weak isospin doublets and singlets. . . . .	11
4.1	Integrated luminosity per year. . . . .	36
4.2	Table of subdetector and trigger status levels required by the $\tau$ pair selection. . . . .	37
4.3	Good charged track and ECAL cluster definitions for the $\tau$ pair selection.	40
4.4	The requirements for a good $\tau$ pair event and rejection of $e^+e^- \rightarrow q\bar{q}$ , $e^+e^- \rightarrow e^+e^-$ and $e^+e^- \rightarrow \mu^+\mu^-$ backgrounds. . . . .	42
4.5	The requirements for rejecting the backgrounds from two-photon and cosmic processes. . . . .	43
4.6	Non- $\tau$ background in the $\tau$ pair sample. . . . .	45
5.1	The various decay modes for each selection. . . . .	47
7.1	Correction factors used to scale the $\tau^- \rightarrow e^- \bar{\nu}_e \nu_\tau$ and $\tau^- \rightarrow \mu^- \bar{\nu}_\mu \nu_\tau$ backgrounds. . . . .	70
7.2	The corrected backgrounds as a percentage of each selection. . . . .	71

8.1	Tables showing the efficiency to detect each signal channel, the number of jets and fractions for each data selection, the branching ratio results and the statistical correlations between each branching ratio. . . . .	77
8.2	Systematic errors. . . . .	80
B.1	Data and Monte Carlo values used to calculate the $\tau^- \rightarrow e^- \bar{\nu}_e \nu_\tau$ correction factors. . . . .	100
B.2	Values used to calculate $R$ in the $\tau^- \rightarrow h^- \nu_\tau$ selection. . . . .	102
B.3	The final number of $\tau^- \rightarrow h^- K_L^0 X \nu_\tau$ decays in each sample. . . . .	105
B.4	The various contributions to the $\tau^- \rightarrow h^- K_L^0 X \nu_\tau$ background systematic error. . . . .	106
C.1	The various Monte Carlo samples used in the bias factor calculations. . . . .	108
C.2	The bias factors for all decay modes in each Monte Carlo sample. The errors shown are statistical. . . . .	111
C.3	The $\tau^- \rightarrow h^- \nu_\tau$ , $\tau^- \rightarrow h^- \pi^0 \nu_\tau$ and $\tau^- \rightarrow h^- \geq 2\pi^0 \nu_\tau$ bias factors. . . . .	112
D.1	The correlation coefficients between each measurement. . . . .	114
E.1	Efficiency matrix. . . . .	116
E.2	Mean values and RMS errors of the modified inverse efficiency matrix. . . . .	118
E.3	The Inverse of the efficiency matrix. . . . .	118

# Acknowledgements

I would like to thank the many people that made this analysis possible. I thank the other members of the OPAL collaboration whose expertise and creativity makes it possible to run such a complex experiment. I would also like to thank Randy Sobie for his patient explanations and insight during this analysis. I would also like to thank the Victoria High Energy Physics group under the leadership of Richard Keeler for providing such a good working environment. Also I would like to acknowledge the support of my parents and sisters who probably puzzled over what I have been doing for such a long time. Finally I would like to thank my wife, Maicci, for her support and understanding throughout this work.

# Chapter 1

## Introduction

The interaction between two particles can be classically described by a potential or field due to one particle acting on the other. As the size of the particle decreases this classical description of their interaction is no longer appropriate. Instead a quantum mechanical description is used where the particles interact via an intermediary quanta. The quanta that mediate the interactions are governed by the Heisenberg Uncertainty principle hence the range of the interaction is inversely proportional to the mass of the quanta. The strength of the interaction is governed by the coupling of the mediating quanta to matter.

The Standard Model [1] of particle physics embodies our knowledge of the properties and interactions of particles at the fundamental scale. In the Standard Model the fundamental particles interact through the electroweak and strong forces. This thesis investigates an aspect of the coupling of matter to the quanta that mediate the electroweak force, the charged weak bosons or  $W^\pm$  particles.

There are two types of particle in nature: the fermions that constitute all matter, and the bosons that mediate the forces. Fermions have a total spin of one-half and obey Fermi-Dirac statistics. They are divided into two groups: six leptons and six quarks. Leptons carry integer electric charge and interact through the electromagnetic

Leptons			Quarks		
Name	Mass (MeV)	Charge ( $e$ )	Name	Mass (MeV)	Charge ( $e$ )
electron ( $e$ )	0.511	-1	up	$5.0 \pm 3.0$	+2/3
$\nu_e$	< 0.000017	0	down	$10 \pm 5$	-1/3
muon ( $\mu$ )	106	-1	charm	$1.3 \pm 0.3$	+2/3
$\nu_\mu$	< 0.27	0	strange	$199 \pm 33$	-1/3
tau ( $\tau$ )	1777	-1	top	$174.1 \pm 5.4$ GeV	+2/3
$\nu_\tau$	< 35	0	bottom	$4.3 \pm 0.3$ GeV	-1/3

Table 1.1: Leptons and quarks arranged in generations of increasing mass [2]. The top mass is from reference [3]. Each pair of rows corresponds to a lepton and quark generation. All the fermions have corresponding antifermions.

and weak force. Quarks carry colour charge and non-integer electric charge and interact through the electromagnetic, weak and strong forces. A single free quark has never been observed and it is believed that this is due to the form of the strong force. Instead quarks appear in the Standard Model in combinations called hadrons, that are colour singlets with integer or zero electric charge. Hadrons are particles composed of a quark and an anti-quark (mesons) or three quarks or anti-quarks (baryons). The leptons and quarks are each arranged, by mass<sup>1</sup>, into three generations. The physical properties between each fermion generation are identical except for the masses of the particles. The fermion generations are shown in Table 1.1.

The forces that govern the interaction of the fermions are transmitted by bosons which have an integer spin value and obey Bose-Einstein statistics (see Table 1.2). The electromagnetic force is transmitted by the massless *photon*; the strong force by one of eight massless *gluons*; and the weak force by the massive  $Z^0$ ,  $W^+$  and  $W^-$  particles<sup>2</sup> [5, 6].

---

<sup>1</sup>Natural units with  $\hbar = c = 1$  are used throughout unless otherwise stated.

<sup>2</sup>In this paper the negative charge state is referred to exclusively but charge conjugation is implied throughout.

Force	Mediator	Mass (GeV)	Spin
EM	photon	0	1
Strong	gluon	0	1
Weak (neutral)	$Z^0$	$91.188 \pm 0.007$	1
Weak (charged)	$W^\pm$	$80.32 \pm 0.19$	1

Table 1.2: Bosons that mediate the forces of the Standard Model. The  $W^\pm$  and  $Z^0$  masses are from reference [4].

The range of each force can be illustrated by recalling the Heisenberg Uncertainty principle which states that the uncertainty on the energy and time of a particle must be at least  $\Delta E \Delta t = \hbar$ . Therefore some energy  $\Delta E$  may be “borrowed” without violating energy conservation for a maximum time of  $\Delta t \leq \hbar/mc^2$  where  $mc^2$  is the mass of the virtual boson that is exchanged. The range  $R$  of the virtual boson is

$$R \equiv c\Delta t = \frac{\hbar}{\Delta mc}$$

where  $c$  is the speed of light. Therefore the photon can be created with essentially no energy and can thus exist for a significant time with the result that the electromagnetic force can act over large distances. The gluon is massless but due to the strong force potential that increases linearly at large distances, the quarks and gluons are confined exclusively to hadrons. The relatively large masses of the  $W^-$  and  $Z^0$  bosons of the weak force imply that energy may be used for a very short period of time to create these mediating particles hence the range of the weak force is limited.

The strength of each force depends on the nature of the coupling between matter (fermions) and the mediating particles (bosons). The Standard Model predicts the form of the interactions but not the strength, so the coupling constants must be measured experimentally. An electromagnetic coupling between a fermion and a photon is shown in figure 1.1(a). The strength of the electromagnetic coupling, which can

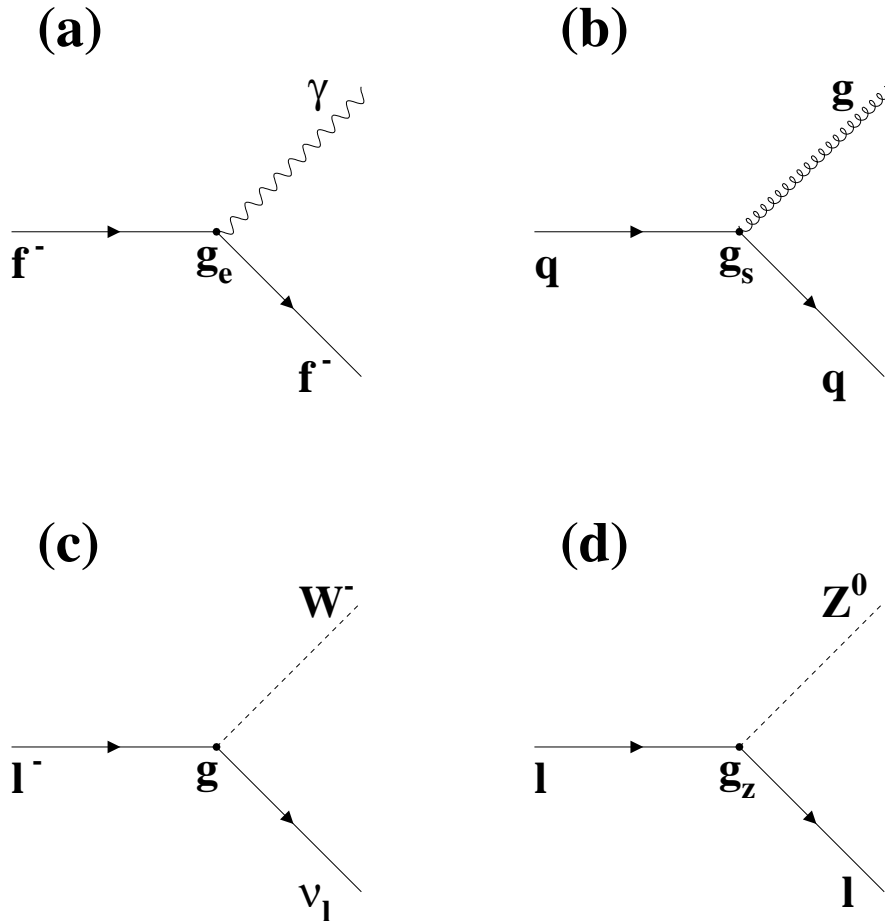


Figure 1.1: Couplings for each interaction in the Standard Model. (a) shows the electromagnetic coupling, strength  $g_e$ , between a charged fermion ( $f^-$ ) and a photon. (b) shows the strong coupling, strength  $g_s$ , between a quark ( $q$ ) and a gluon. (c) shows the charged weak coupling, strength  $g$ , between a lepton-neutrino pair and a  $W^-$  boson. (d) shows the neutral weak coupling, strength  $g_z$ , between a fermion (charged or neutrino) and a  $Z^0$  boson.



be estimated by examining the splitting of the electron energy levels in the hydrogen atom, is given by the fine structure constant<sup>3</sup>

$$\alpha = \frac{g_e^2}{4\pi} \approx \frac{1}{137}$$

where  $g_e$  is the electromagnetic coupling strength.

Figure 1.1(b) shows the strong force coupling between a quark and gluon. An estimate of the relative strength of the strong force, made by comparing the lifetimes of similar strong and electromagnetic decay processes at similar values of momentum transfer, gives

$$\frac{\alpha_s}{\alpha} \simeq 100$$

where  $\alpha_s$  is the strong force structure constant.

Figure 1.1(c) shows a weak interaction that involves the coupling of a  $W^-$  boson to fermions, known as the charged current weak interaction. The strength of the weak force can be estimated from the muon to electron decay rate ( $\mu^- \rightarrow e^- \bar{\nu}_e \nu_\mu$ ) and a value for the coupling,  $\alpha_w$ , analogous to the fine structure constant of

$$\alpha_w \equiv \frac{g^2}{4\pi} \approx \frac{1}{29}$$

is obtained where  $g$  is the coupling strength of the charged current weak interaction. This result suggests that the weak force is actually stronger than the electromagnetic force. Thus the intrinsic coupling of the weak force is not small but the large mass of the mediating bosons reduces this force at large distances.

There is also a neutral current weak interaction that involves no transfer of electric charge that is shown in figure 1.1(d). The coupling strength of the  $Z^0$  boson to

---

<sup>3</sup>The best measurement of  $\alpha$  is made using the quantum Hall effect, for example see reference [2].

fermions ( $g_z$ ) differs from the charged weak interaction constant. This difference is caused by the mixing of the underlying fields in the theory that mediate the neutral interaction and is parameterized by the Weinberg or *weak mixing* angle ( $\theta_w$ ). The neutral weak interaction coupling constant is related to the charged current interaction coupling by  $g_z = g / \cos \theta_w$  and is given by

$$\alpha_z \equiv \frac{g_z^2}{4\pi} \approx \frac{1}{23}.$$

The Standard Model has been tested by many experimental results and has proven to be a model capable of precise predictions. However it is universally accepted that the Standard Model cannot be the last word, although no experimentally verified extension of the Standard Model has emerged.

The work presented in this thesis tests the Standard Model postulate that the  $W^-$  boson couples to each lepton generation with equal strength (*lepton universality*). The third-generation  $\tau^-$  lepton is used to measure the ratio of the strengths of the  $W^-$  boson coupling to  $\mu^-$  and  $\tau^-$  leptons. The  $\tau^-$  lepton is the heaviest lepton (see Table 1.1) and can decay to leptonic final states (Feynman diagrams given in figure 1.2)

$$\tau^- \rightarrow e^- \bar{\nu}_e \nu_\tau$$

$$\tau^- \rightarrow \mu^- \bar{\nu}_\mu \nu_\tau$$

or semi-leptonic final states, addressed in chapter 2 of this thesis, such as

$$\tau^- \rightarrow h^- \nu_\tau$$

$$\tau^- \rightarrow h^- \pi^0 \nu_\tau$$

$$\tau^- \rightarrow h^- 2\pi^0 \nu_\tau$$

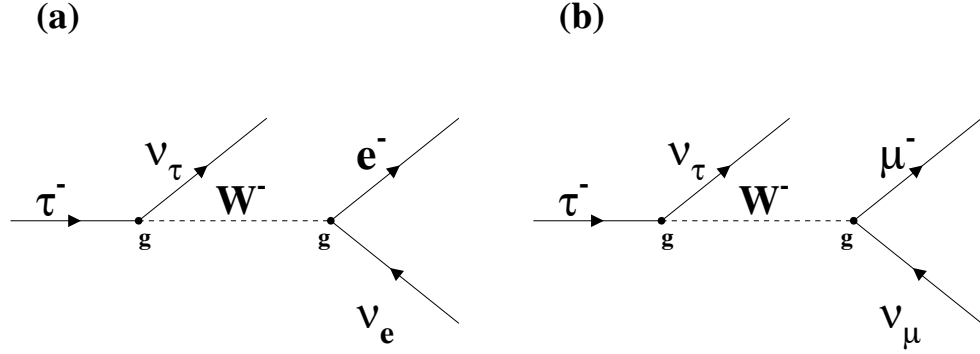


Figure 1.2: (a) shows the Feynman diagram for the decay  $\tau^- \rightarrow e^- \bar{\nu}_e \nu_\tau$ . (b) shows the Feynman diagram for the decay  $\tau^- \rightarrow \mu^- \bar{\nu}_\mu \nu_\tau$ .

where the symbol  $h^-$  is used to indicate either a  $\pi^-$  or  $K^-$  meson. Any new physics effects may preferentially appear in  $\tau^-$  lepton decays, rather than electron or muon decays because the  $\tau$  has a very large mass,  $m_\tau \simeq 3600m_e$ . Therefore the  $\tau^-$  lepton is expected to couple strongly to the underlying vacuum potential that generates the fermion and boson masses, an area of possible new physics. The observation of any new physics effects is possible through precise measurements of the decay rates of the  $\tau^-$  lepton to various final states.

The work presented in this thesis measures the rate at which the  $\tau^-$  lepton decays to one charged hadron ( $h^-$ ) accompanied by 0, 1 or  $\geq 2$   $\pi^0$ 's. The decay rate of the  $\tau$  to a single charged hadron ( $\tau^- \rightarrow h^- \nu_\tau$ ) can be compared to the decay rate of  $h^- \rightarrow \mu^- \bar{\nu}_\mu$  to test the relative coupling strength of the  $W$  boson to  $\mu$  and  $\tau$  leptons.

A more detailed description of the weak interaction that mediates these decays of the  $\tau^-$  lepton is presented in Chapter 2. Chapter 2 also outlines the properties of the  $\tau^-$  lepton that make it an attractive option for testing the  $W^-$  boson coupling

strength. Chapter 3 gives a description of the LEP collider and the OPAL detector data-taking stream and subdetectors. The data obtained by OPAL from LEP and the sample of simulated events used to describe the data are presented in Chapter 4. Chapter 4 also details the requirements on the selection of a pure sample of  $\tau$  pair events. In Chapter 5 the individual  $\tau$  events are examined and events with a one charged track topology are selected. Chapter 6 describes how the electromagnetic calorimeter clusters are formed and matched to charged tracks and also shows how the electromagnetic calorimeter cluster energies and track momentum in the Monte Carlo sample is optimized to the data. In Chapter 6 the possible  $\pi^0$  topologies are described and the  $\pi^0$  identification algorithm is shown. In Chapter 7 the  $\tau$  backgrounds in each selection are identified and measured. Chapter 8 presents the method of determining of the  $\tau$  branching ratios and the results of this analysis are given. The branching ratio results are compared to previous and current results in Chapter 8. Chapter 9 contains the final discussion of the results obtained from this work.

# Chapter 2

## The weak interaction and the $\tau$ lepton

The first section of this chapter reviews the weak interaction. While the second section discusses the  $\tau^- \rightarrow \pi^- \nu_\tau$  and  $\tau^- \rightarrow K^- \nu_\tau$  decay widths and the third section derives the  $\tau^- \rightarrow h^- \pi^0 \nu_\tau$  decay width. The last section shows how the  $\tau^- \rightarrow h^- \nu_\tau$  branching ratio can be used to test lepton universality.

### 2.1 The weak interaction

The Standard Model is a theory based upon *local gauge invariance*. This implies the global symmetries of the forces are also true locally. For example, exchanging plus charges with minus charges throughout the whole universe leaves the electromagnetic force unchanged. The principle of local gauge invariance allows this rotation of charges to be made at all space-time points independently. The symmetry is preserved through the introduction of a force whose specific characteristics depend on the symmetry group. The corresponding force is mediated by gauge bosons. A requirement of local gauge invariance is that the gauge bosons are massless.

In the Standard Model the interaction of two fermions with a gauge boson is

represented as a Dirac current. The strength of the fermion to boson coupling is dictated by the fermion's quantum numbers, such as its electric charge.

The  $SU_L(2)$  gauge group describes the weak interaction with the quantum number weak isospin ( $T$ ). This group carries the subscript  $L$  to indicate the charged weak isospin current involves a coupling, of strength  $g$ , between  $W^-$  bosons and the left-handed *chiral* component of fermions only. The chiral state of a particle is the same as its helicity<sup>1</sup> for massless particles. The group structure of  $SU_L(2)$  dictates three generators that are interpreted as three weak isospin interaction *currents*. These currents represent the interactions of the  $SU_L(2)$  massless gauge bosons ( $W_\mu^1, W_\mu^2, W_\mu^3$ ) with the left-handed chiral component of fermions. A full weak isospin symmetry of  $SU_L(2)$  could be realised if the weak isospin currents corresponded to the couplings of fermions to the  $W^-$ ,  $W^+$  and  $Z^0$  bosons of the weak interaction. But this assumption is not correct since the  $Z^0$  boson, which mediates the neutral weak current, has couplings to the right-handed component of particles. Furthermore both the  $W^\pm$  and  $Z^0$  bosons of the weak interaction are massive.

These difficulties of the  $SU_L(2)$  theory are resolved in the theory of Glashow, Salam and Weinberg (GSW) that unifies the weak and electromagnetic interactions. It is observed that the electromagnetic interaction, generated by the  $U(1)$  group with quantum number  $e$  (electric charge), couples to both the left and right-handed chiral components of particles with strength  $g_e$ . The  $U(1)$  group is combined with  $SU_L(2)$  to account for the right-handed chiral couplings of the neutral weak current

---

<sup>1</sup>A particle with positive (negative) helicity is known as right (left)-handed where helicity  $\mathcal{H}$  is defined as  $\mathcal{H} \equiv 2\vec{J} \cdot \hat{p}$  where  $\vec{J}$  is the spin and  $\hat{p}$  is a unit vector in the direction of the momentum of the particle.

by associating the  $U(1)$  group to weak hypercharge ( $Y$ ), defined as

$$Y \equiv 2(Q - T^3)$$

where  $Q$  is the electric charge of the particle and  $T^3$  is the  $\hat{z}$  component of weak isospin. This leads to a weak hypercharge current of the  $U_Y(1)$  group mediated by a boson ( $B_\mu$ ) that couples with strength  $g'$ . The relationship between weak hypercharge and weak isospin indicates that the  $U_Y(1)$  and  $SU_L(2)$  groups are parts of the underlying group  $SU_L(2) \times U_Y(1)$ . Table 2.1 reviews the weak isospin and weak hypercharge assignments for the first generation of leptons and quarks.

Fermions	$T$	$T^3$	$Y$
$\begin{pmatrix} \nu_e \\ e \end{pmatrix}_L$	1/2	$\pm 1/2$	-1
$\begin{pmatrix} u \\ d \end{pmatrix}_L$	1/2	$\pm 1/2$	1/3
$e_R$	0	0	-2
$u_R$	0	0	4/3
$d_R$	0	0	-2/3

Table 2.1: The first generation of fermions in the Standard Model arranged in weak isospin doublets and singlets. The total weak isospin ( $T$ ),  $\hat{z}$  component of weak isospin ( $T^3$ ) and weak hypercharge ( $Y$ ) assignments are shown. The subscripts  $L$  and  $R$  refer to left and right-handed chiral states respectively.

The  $SU_L(2) \times U_Y(1)$  group is made to be locally gauge invariant in the Standard Model. This implies that the gauge bosons of this group ( $W_\mu^1, W_\mu^2, W_\mu^3, B_\mu$ ) are massless yet the  $W^\pm$  and  $Z^0$ , the bosons of the weak interaction, are massive [5, 6]. The mass problem can be solved if some of the symmetries of the  $SU_L(2) \times U_Y(1)$  group are “spontaneously broken”. The weak isospin and weak hypercharge symmetries are broken by adding a new field, the *Higgs field* [7] that has  $Y = 1$  and  $T = 1/2$ , that

couples to the bosons and fermions in the  $SU_L(2) \times U_Y(1)$  group. The potential of this field is such that the ground state is non-zero and does not preserve the weak hypercharge and weak isospin symmetries of  $SU_L(2) \times U_Y(1)$  but does preserve the electric charge symmetry of the electromagnetic interaction. Now that the symmetry of weak isospin is broken the  $W^\pm$  bosons, the weak charged current mediators, acquire a mass given by

$$M_W = \frac{v}{2}g$$

where  $v$  is a parameter that sets the scale of  $SU_L(2) \times U_Y(1)$  spontaneous symmetry breaking. The physical  $Z^0$  boson, the weak charged current mediator that has both right and left handed chiral couplings, is produced by mixing of weak isospin  $W_\mu^3$  and weak hypercharge  $B_\mu$  bosons,

$$Z_\mu = \cos \theta_w W_\mu^3 - \sin \theta_w B_\mu.$$

The Weinberg or weak mixing angle  $\theta_w$  parameterizes the level of mixing between  $SU_L(2)$  and  $U_Y(1)$  and is given by

$$\tan \theta_w \equiv \frac{g'}{g}.$$

The  $Z^0$  boson mass, generated as a result of  $SU_L(2) \times U_Y(1)$  symmetry breaking is given by

$$M_Z = \frac{v}{2}\sqrt{g'^2 + g^2}.$$

The physical photon exists as the mixed state, orthogonal to  $Z_\mu$ , of the weak isospin  $W_\mu^3$  and weak hypercharge  $B_\mu$  bosons as

$$A_\mu = \sin \theta_w W_\mu^3 + \cos \theta_w B_\mu$$



but keeps its zero mass since the electric charge symmetry is unbroken by the Higgs field.

A result of  $SU_L(2) \times U_Y(1)$  local gauge invariance is that the coupling strengths of the photon and the weak gauge bosons to fermions can be related. A comparison between the photon interaction written in the electroweak ( $SU_L(2) \times U_Y(1)$ ) and electromagnetic ( $U(1)$ ) forms leads to a relationship between the coupling strength of  $W^\pm$  bosons to fermions,  $g$ , and the electromagnetic coupling constant,  $g_e$ , of

$$g = \frac{g_e}{\sin \theta_w}.$$

A value for  $g_z$ , the coupling strength of the  $Z^0$  boson to fermions, is found using a transformation of the weak hypercharge current to the weak isospin and electric charge currents within the neutral weak interaction and is given by

$$g_z = \frac{g_e}{\cos \theta_w \sin \theta_w}.$$

Thus the GWS theory predicts that the weak and electromagnetic coupling constants are related through the weak mixing angle.

## 2.2 $\tau^- \rightarrow \pi^- \nu_\tau$ and $\tau^- \rightarrow K^- \nu_\tau$ decay widths

The  $\tau^-$ , the charged lepton of the third generation weak isospin doublet, is the heaviest known lepton ( $m_\tau = 1777.0 \pm 0.3$  MeV) [2] and decays via the charged current weak interaction. The total width of the  $\tau^-$  ( $\Gamma_\tau$ ) is given by the sum of the widths of the individual decays ( $\Gamma_i$ ) and is inversely proportional to the  $\tau^-$  lifetime ( $\tau_\tau$ ). The general formula for a  $\tau$  with lifetime  $\tau_\tau$  and total width  $\Gamma_\tau$  is

$$\tau_\tau = \frac{1}{\Gamma_\tau}. \tag{2.1}$$

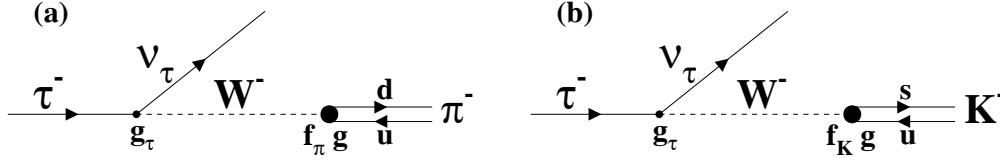


Figure 2.1: The tree-level Feynman diagram for the  $\tau^- \rightarrow \pi^- \nu_\tau$  decay. The constant  $g$  refers to the coupling strength between the  $W^-$  boson and fermions.  $f_\pi$  is the pion form factor.

The *branching ratio* of the  $\tau^-$  lepton to a given final state is defined as the ratio of the given decay width to the total decay width,

$$B(\tau^- \rightarrow h^- \nu_\tau) = \frac{\Gamma(\tau^- \rightarrow h^- \nu_\tau)}{\Gamma_\tau}. \quad (2.2)$$

The differential decay width ( $d\Gamma$ ) for a particle, with mass  $m$ , can be written as

$$d\Gamma = \frac{1}{2m} |\overline{\mathcal{M}}|^2 d\mathcal{L}ips \quad (2.3)$$

where  $|\overline{\mathcal{M}}|^2$  is the squared spin-averaged matrix element and  $\mathcal{L}ips$  is the *Lorentz invariant phase space* factor. The matrix element for a decay contains the dynamical information about the decay and can be evaluated from a Feynman diagram. The Lorentz invariant phase space factor contains the kinematic information of the decay.

Figure 2.1 shows the lowest order Feynman diagrams for the  $\tau^- \rightarrow \pi^- \nu_\tau$  and  $\tau^- \rightarrow K^- \nu_\tau$  decays. The matrix element for the  $\tau^- \rightarrow \pi^- \nu_\tau$  decay can be written as

$$\mathcal{M}_{\pi\nu_\tau} = \frac{g_\tau g}{8m_W^2} [\overline{u}(\overline{\nu}_\tau) \gamma^\mu (1 - \gamma^5) u(\tau^-)] \langle 0 | J_\mu^+ | \pi^- \rangle \quad (2.4)$$

and the matrix element for the  $\tau^- \rightarrow K^- \nu_\tau$  decay is

$$\mathcal{M}_{K\nu_\tau} = \frac{g_\tau g}{8m_W^2} [\overline{u}(\overline{\nu}_\tau) \gamma^\mu (1 - \gamma^5) u(\tau^-)] \langle 0 | J_\mu^+ | K^- \rangle \quad (2.5)$$

where  $u$  and  $\bar{u}$  are Dirac spinor and  $g_\tau$  is the charged weak coupling strength at the  $W^- \tau^-$  vertex. The factor  $\langle 0 | J_\mu^+ | \pi^- \rangle$  is the hadronic current for the  $\tau^- \rightarrow h^- \nu_\tau$  decay and has the form

$$\langle 0 | J_\mu^+ | \pi^- \rangle = i V_{ud} f_\pi p_\mu^\pi \quad (2.6)$$

and  $\langle 0 | J_\mu^+ | K^- \rangle$  is the hadronic current for the  $\tau^- \rightarrow K^- \nu_\tau$  decay and is given by

$$\langle 0 | J_\mu^+ | K^- \rangle = i V_{us} f_K p_\mu^K. \quad (2.7)$$

where  $f_\pi$  and  $f_K$  are decay constants,  $V_{ud}$  and  $V_{us}$  are elements of the Cabibbo-Kobayashi-Maskawa (CKM) matrix and  $p_\pi^\mu$  and  $p_K^\mu$  are the four-vectors of the pion and kaon respectively.

The decay constants,  $f_\pi = 130.7 \pm 0.4$  MeV [2] and  $f_K = 159.8 \pm 1.5$  MeV [2], parameterize the non-perturbative colour force effects at the  $W^- \pi^-$  and  $W^- K^-$  vertices. These decay constants are determined for pions and kaons by measuring the  $h^- \rightarrow \mu^- \bar{\nu}_\mu$  decay widths, where  $h^- = \pi^-$  or  $K^-$ .

As stated above,  $V_{ud}$  and  $V_{us}$  are elements of the CKM matrix. The CKM matrix [8] gives the mixing between the mass eigenstates and the weak eigenstates of the  $-e/3$  charged quarks. By convention, the  $2e/3$  charged quarks are unmixed. The element  $V_{ud}$  is measured by comparing nuclear beta decay to muon decay and is found to be  $|V_{ud}| = 0.9736 \pm 0.0010$  [2]. A value of  $V_{us} = 0.2196 \pm 0.0023$  [2] is found by analyzing the decay  $K^- \rightarrow \pi^0 e^- \bar{\nu}_e$ .

The Lorentz invariant phase space factor,  $d\mathcal{L}ips_{\pi\nu}$ , for the  $\tau^- \rightarrow \pi^- \nu_\tau$  decay is evaluated as

$$d\mathcal{L}ips_{\pi\nu} = \frac{1}{2(2\pi)^2} \left( 1 - \frac{m_\pi^2}{m_\tau^2} \right) d\Omega \quad (2.8)$$

and likewise for the  $\tau^- \rightarrow K^- \nu_\tau$  decay is

$$d\mathcal{L}ip_{s_{K\nu}} = \frac{1}{2(2\pi)^2} \left(1 - \frac{m_K^2}{m_\tau^2}\right) d\Omega. \quad (2.9)$$

where  $m_\tau$  is the mass of the  $\tau^-$  lepton,  $m_\pi = 139.56995(35)$  MeV ( $m_K = 493.667 \pm 0.0013$  MeV) is the mass of the  $\pi^-$  ( $K^-$ ) meson [2] and  $d\Omega$  is the solid angle element.

The individual decay widths are evaluated by integrating equation 2.3, averaging over the initial spin of the  $\tau^-$ , summing over the final state  $\nu_\tau$  spin. This procedure gives a  $\tau^- \rightarrow \pi^- \nu_\tau$  width of

$$\Gamma(\tau^- \rightarrow \pi^- \nu_\tau) = \frac{g_\tau^2 g^2 f_\pi^2 V_{ud}^2 m_\tau^3}{512 \pi m_W^4} \left(1 - \frac{m_\pi^2}{m_\tau^2}\right)^2 \quad (2.10)$$

and a  $\tau^- \rightarrow K^- \nu_\tau$  width of

$$\Gamma(\tau^- \rightarrow K^- \nu_\tau) = \frac{g_\tau^2 g^2 f_K^2 V_{us}^2 m_\tau^3}{512 \pi m_W^4} \left(1 - \frac{m_K^2}{m_\tau^2}\right)^2. \quad (2.11)$$

The radiative corrections to equations 2.10 and 2.11 will be discussed later in this chapter.

### 2.3 $\tau^- \rightarrow \pi^- \pi^0 \nu_\tau$ decay width

The  $\tau^- \rightarrow \pi^- \pi^0 \nu_\tau$  decay, shown in figure 2.2, proceeds through the hadronic weak vector current. The coupling strength of the weak vector current to  $\pi^- \pi^0$  is related to the coupling strength of the electromagnetic current to  $\pi^+ \pi^-$  by the conserved vector current (CVC) hypothesis [9]. The electromagnetic coupling can be calculated from the measured  $e^+e^- \rightarrow \pi^+ \pi^-$  cross section and neglecting radiative corrections, the decay width,  $\Gamma(\tau^- \rightarrow \pi^- \pi^0 \nu_\tau)$  is related to the cross section by [10]

$$\begin{aligned} \Gamma(\tau^- \rightarrow \pi^- \pi^0 \nu_\tau) &= \frac{g_\tau^2 g^2 V_{ud}^2}{\alpha^2 (8\pi m_W)^4} \int_0^{m_\tau^2} \left(1 - \frac{q^2}{m_\tau^2}\right)^2 \left(1 + \frac{2q^2}{m_\tau^2}\right) \\ &\quad \times \sigma_{e^+e^- \rightarrow \pi^+\pi^-}^{I=1}(q^2) q^2 dq^2 \end{aligned} \quad (2.12)$$

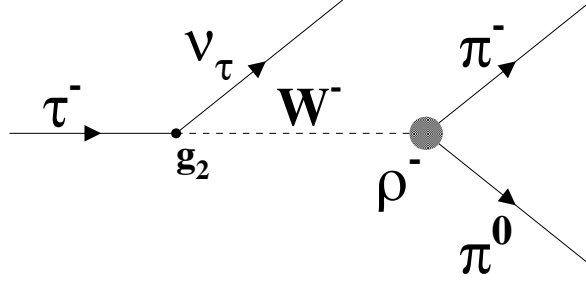


Figure 2.2: The tree-level Feynman diagram for the  $\tau^- \rightarrow \pi^- \pi^0 \nu_\tau$  decay. The  $\rho^-$  resonance is indicated by the large dot on the right and the  $\rho^-$  decay products are shown as the  $\pi^-$  and  $\pi^0$  mesons.

where  $q^2$  is the square of the invariant mass of the  $\pi^-, \pi^0$  system and  $\sigma_{e^+e^- \rightarrow \pi^+\pi^-}^{I=1}(q^2)$  is the isospin 1 part of the low energy  $e^+e^- \rightarrow \pi^+\pi^-$  cross section. This prediction is compared in chapter 9 to the measurement reported in this thesis.

## 2.4 Lepton universality

Lepton universality in the Standard Model requires that, after corrections for differences in mass, the electron, muon and tau leptons have the same properties. Thus the  $SU_L(2) \times U_Y(1)$  group quantum numbers and transformation properties are identical for these three charged leptons. In particular, the weak (charged and neutral) couplings of the charged leptons are expected to be identical, ie.

$$g = g_e = g_\mu = g_\tau$$

$$g' = g'_e = g'_\mu = g'_\tau$$

where  $g_i$  and  $g'_i$  are the  $SU_L(2)$  and  $U_Y(1)$  couplings respectively. Any significant deviation from these relations would imply new physics.

The universality of the charged weak couplings is tested by comparing decays

that have the same general form, but involve couplings to different leptons. Figure 2.3 shows the Feynman diagrams for the  $\tau^- \rightarrow h^- \nu_\tau$  and  $h^- \rightarrow \mu^- \bar{\nu}_\mu$  decays for both cases where  $h^- = \pi^-$  or  $K^-$ . The charged weak current coupling constant,  $g$ , is

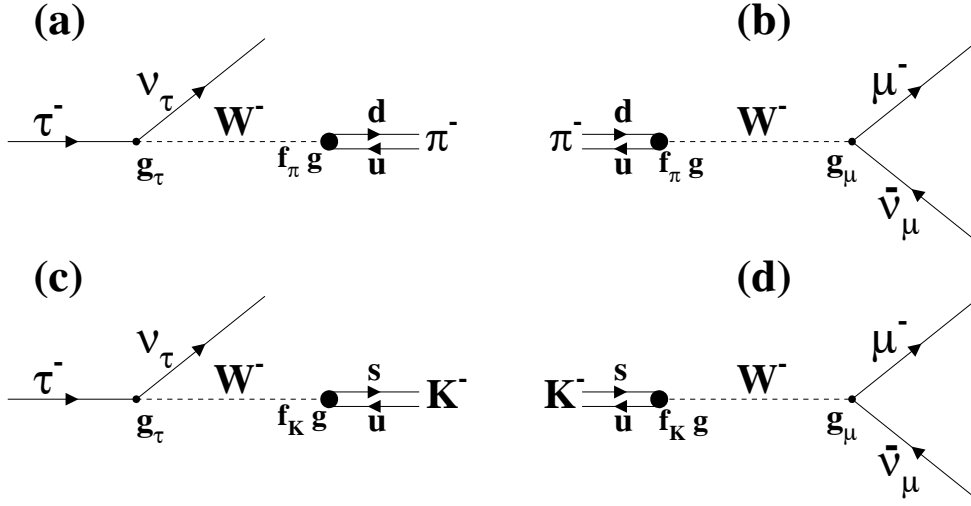


Figure 2.3: Figures (a) and (c) show the tree level Feynman diagrams for the  $\tau^- \rightarrow \pi^- \nu_\tau$  and  $\tau^- \rightarrow K^- \nu_\tau$  decays respectively. Figures (b) and (d) show the tree level Feynman diagrams for the  $\pi^- \rightarrow \mu^- \bar{\nu}_\mu$  and  $K^- \rightarrow \mu^- \bar{\nu}_\mu$  decays respectively. The possibility of different couplings at the lepton- $W^-$  boson vertices are indicated by the coupling constants  $g_\tau$  and  $g_\mu$ .

expressed as  $g_\tau$  and  $g_\mu$  at the  $W^- \tau^-$  and  $W^- \mu^-$  vertices respectively to illustrate the different possible couplings. The width for the  $\pi^- \rightarrow \mu^- \bar{\nu}_\mu$  decay is given by

$$\Gamma(\pi^- \rightarrow \mu^- \bar{\nu}_\mu) = \frac{g^2 g_\mu^2 f_\pi^2 V_{ud}^2 m_\pi m_\mu^2}{256 \pi m_W^4} \left(1 - \frac{m_\mu^2}{m_\pi^2}\right)^2 \quad (2.13)$$

and for the  $K^- \rightarrow \mu^- \bar{\nu}_\mu$  decay is

$$\Gamma(K^- \rightarrow \mu^- \bar{\nu}_\mu) = \frac{g^2 g_\mu^2 f_K^2 V_{us}^2 m_K m_\mu^2}{256 \pi m_W^4} \left(1 - \frac{m_\mu^2}{m_K^2}\right)^2 \quad (2.14)$$

The general forms of the  $\tau^- \rightarrow \pi^- \nu_\tau$  and  $\pi^- \rightarrow \mu^- \bar{\nu}_\mu$  decays (figs 2.3(a) and 2.3(b)) are the same, they differ in the type of lepton ( $\tau^-$  vs.  $\mu^-$  respectively) that couples to

the  $W^-$  boson. The same observation is made for the  $\tau^- \rightarrow K^- \nu_\tau$  and  $K^- \rightarrow \mu^- \bar{\nu}_\mu$  decays shown in figures 2.3(c) and 2.3(d).

An expression for  $g_\tau^2/g_\mu^2$  can be obtained from the  $\tau^- \rightarrow h^- \nu_\tau$  decay widths (equations 2.10 and 2.11) and  $h^- \rightarrow \mu^- \bar{\nu}_\mu$  decay widths (equations 2.13 and 2.14) and equation 2.2. The sum of the  $\tau^- \rightarrow \pi^- \nu_\tau$  branching ratio and  $\tau^- \rightarrow K^- \nu_\tau$  branching ratio can be expressed, using equations 2.2 and 2.1, as

$$B(\tau^- \rightarrow \pi^- \nu_\tau) + B(\tau^- \rightarrow K^- \nu_\tau) = \tau_\tau [\Gamma(\tau^- \rightarrow \pi^- \nu_\tau) + \Gamma(\tau^- \rightarrow K^- \nu_\tau)] \quad (2.15)$$

where  $\tau_\tau$  is the  $\tau$  lifetime. The  $\tau^- \rightarrow \pi^- \nu_\tau$  and  $\tau^- \rightarrow K^- \nu_\tau$  decay widths can be re-expressed in terms of the  $\pi^- \rightarrow \mu^- \bar{\nu}_\mu$  and  $K^- \rightarrow \mu^- \bar{\nu}_\mu$  decay widths as

$$\frac{\Gamma(\tau^- \rightarrow \pi^- \nu_\tau)}{\Gamma(\pi^- \rightarrow \mu^- \bar{\nu}_\mu)} = \frac{2 m_\tau^3 g_\tau^2 [1 - m_\pi^2/m_\tau^2]^2}{m_\pi m_\mu^2 g_\mu^2 [1 - m_\mu^2/m_\pi^2]^2} (1 + \delta_\pi) \quad (2.16)$$

and

$$\frac{\Gamma(\tau^- \rightarrow K^- \nu_\tau)}{\Gamma(K^- \rightarrow \mu^- \bar{\nu}_\mu)} = \frac{2 m_\tau^3 g_\tau^2 [1 - m_K^2/m_\tau^2]^2}{m_K m_\mu^2 g_\mu^2 [1 - m_\mu^2/m_K^2]^2} (1 + \delta_K) \quad (2.17)$$

using equations 2.10 and 2.11 and equations 2.13 and 2.14. The factors  $\delta_\pi$  and  $\delta_K$  are electromagnetic radiative corrections [11]. The radiative effects in  $h^- \rightarrow \mu^- \bar{\nu}_\mu$  are not the same as those in  $\tau^- \rightarrow h^- \nu_\tau$  due to the difference in energy scale and so the ratios of the decay widths are corrected by the factors [11]

$$\delta_\pi = (0.16 \pm 0.14)\%$$

$$\delta_K = (0.90 \pm 0.22)\%.$$

The expressions in equations 2.16 and 2.17 are now inserted into equation 2.15 to give

$$B(\tau^- \rightarrow \pi^- \nu_\tau) + B(\tau^- \rightarrow K^- \nu_\tau) = \frac{g_\tau^2 m_\tau^2}{g_\mu^2 2m_\mu^2} (H_\pi + H_K) \quad (2.18)$$

where

$$H_\pi = (1 + \delta_\pi) \left( \frac{\tau_\tau m_\tau}{\tau_\pi m_\pi} \right) \left[ \frac{1 - (m_\pi/m_\tau)^2}{1 - (m_\mu/m_\pi)^2} \right]^2 \text{B}(\pi^- \rightarrow \mu^- \bar{\nu}_\mu)$$

and

$$H_K = (1 + \delta_K) \left( \frac{\tau_\tau m_\tau}{\tau_K m_K} \right) \left[ \frac{1 - (m_K/m_\tau)^2}{1 - (m_\mu/m_K)^2} \right]^2 \text{B}(K^- \rightarrow \mu^- \bar{\nu}_\mu)$$

where  $\tau_\pi = 2.60 \times 10^{-8}$  s [2] is the pion lifetime and  $\tau_K = 1.24 \times 10^{-8}$  s [2] is the kaon lifetime. The branching ratios of  $\pi^- \rightarrow \mu^- \bar{\nu}_\mu$  ( $\text{B}(\pi^- \rightarrow \mu^- \bar{\nu}_\mu) = 99.98770(4)\%$ ) and  $K^- \rightarrow \mu^- \bar{\nu}_\mu$  ( $\text{B}(K^- \rightarrow \mu^- \bar{\nu}_\mu) = 63.51 \pm 0.18\%$ ) are available from reference [2]. Rearranging equation 2.18 to solve for  $g_\tau^2/g_\mu^2$  gives

$$\frac{g_\tau^2}{g_\mu^2} = \left\{ \frac{2m_\mu^2 m_\pi}{m_\tau^2} \right\} \frac{\text{B}(\tau^- \rightarrow h^- \nu_\tau)}{H_\pi + H_K} \quad (2.19)$$

where  $\text{B}(\tau^- \rightarrow \pi^- \nu_\tau) + \text{B}(\tau^- \rightarrow K^- \nu_\tau) = \text{B}(\tau^- \rightarrow h^- \nu_\tau)$ . Equation 2.19 shows that a measurement of the  $\tau^- \rightarrow h^- \nu_\tau$  branching ratio, with all the other constants as inputs, can test the universality of the charged weak current couplings to  $\tau$ 's and  $\mu$ 's.

It is interesting to note that both the  $\pi^-$  and  $K^-$  mesons are spin-0 particles. Hence the  $\tau^- \rightarrow h^- \nu_\tau$  and  $h^- \rightarrow \mu^- \bar{\nu}_\mu$  decays are only sensitive to the spin-0 part of the charged weak current. Thus the  $W^-$  boson, that carries spin of 1, must be in a state with a  $\hat{z}$  spin component of 0, known as *longitudinally* polarized. The test of  $g_\tau/g_\mu$  could reveal the presence of a scalar (spin-0) Yukawa-like coupling that depends on the lepton mass.



# Chapter 3

## Experimental equipment

This chapter gives a description of the experimental equipment used to produce, observe and record the electron-positron collisions studied in this thesis. The first section describes the design and operating parameters of the Large Electron Positron (LEP) collider at the European Nuclear Research Centre (CERN) in Geneva, Switzerland. In the second section a general description of the Omni Purpose Detector at LEP (OPAL) is presented. A review of the design and performance of the OPAL subdetectors relevant to the analysis presented in this thesis are given.

### 3.1 The LEP accelerator

The LEP accelerator complex, shown in figure 3.1, consists of several accelerators that make up the injector chain and the LEP storage ring where the electrons ( $e^-$ ) and positrons ( $e^+$ ) are collided at instrumented interaction areas.

#### 3.1.1 Injection chain

The injection chain of the LEP accelerator uses two of CERN's existing accelerators: the 1970's era Proton Synchrotron (PS) that played a part in the discovery of neutral current weak interactions [15]; and the Super Proton Synchrotron (SPS) used in the

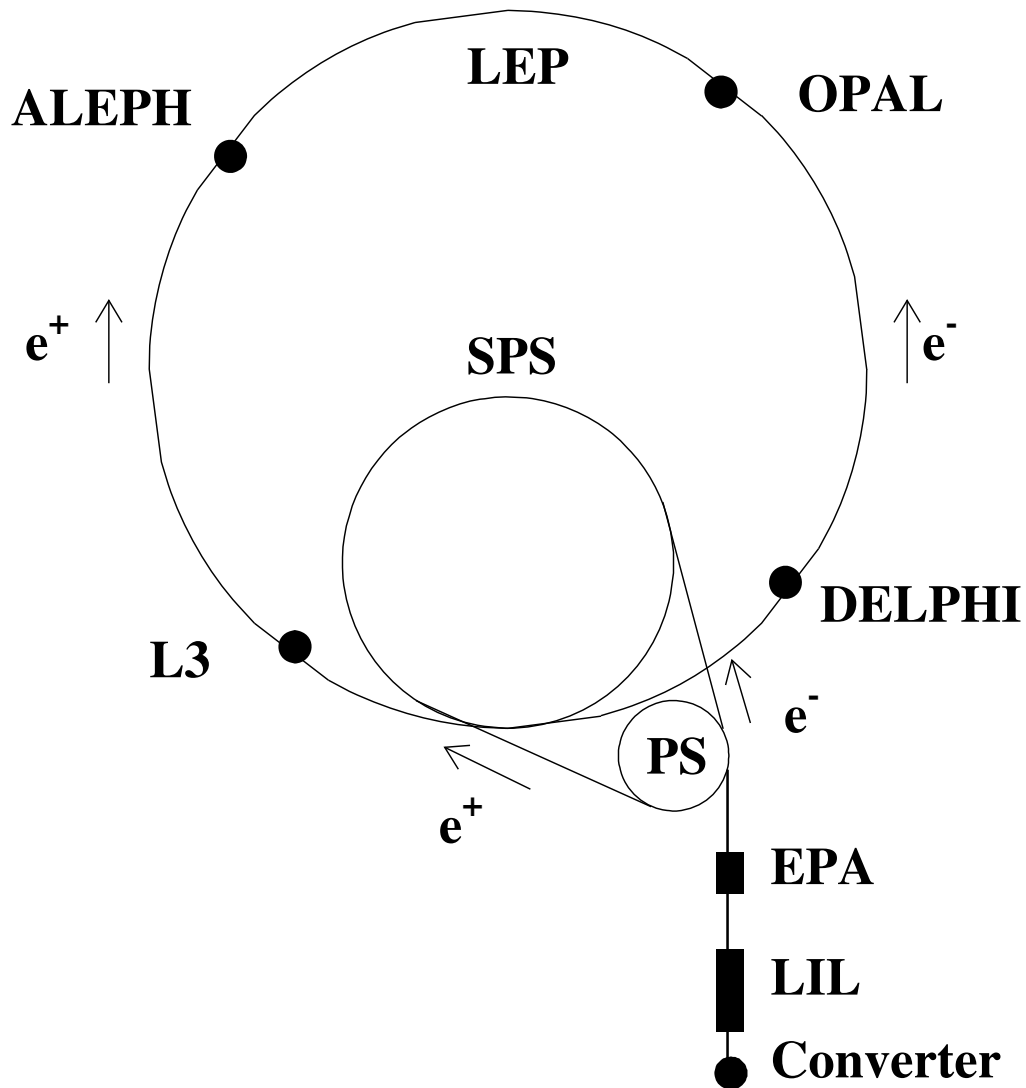


Figure 3.1: Schematic diagram of the injector chain and LEP ring at CERN in Geneva, Switzerland. The LEP ring has a circumference of approximately 27 km. There are four instrumented interaction points on the LEP ring: ALEPH [12], DELPHI [13], L3 [14] and OPAL.

1980's to discover the  $Z^0$  and  $W^\pm$  bosons [5, 6].

The injection sequence starts with a 200 MeV linear accelerator that directs an electron beam onto a converter target to produce positrons. At the same time electrons destined for LEP are produced by another electron gun near the converter target. The electrons and positrons are then accelerated to 600 MeV by another linear accelerator (LIL) and directed to the Electron-Positron Accumulator [16] (EPA). The EPA acts as a buffer between the high frequency linear accelerators and the lower frequency synchrotrons by storing 100 LIL pulses before the next stage. The beams are then fed into the PS and accelerated to 3500 MeV (3.5 GeV). Then the electrons and positrons are sent to the SPS where the beam energies are increased to 20 GeV. Finally, the electron and positron beams are transferred to the LEP storage ring and accelerated to energies of approximately 45 GeV before being steered into collision with each other.

### 3.1.2 LEP ring

The LEP  $e^+e^-$  storage ring consists of a repeating set of horizontally deflecting dipole magnets and alternating focusing and defocusing quadrupole magnets. This arrangement forms a strong focusing lattice that keeps the beams circulating in opposite directions on closed stable orbits around the ring. Radio frequency (RF) cavities provide the accelerating force on each beam. Once the beams reach their operating energy, set by the bending field of the dipole magnets, the RF cavities compensate for synchrotron radiation losses.

The electron and positron beams are each introduced to the LEP ring as four equally spaced bunches ( $4 \times 4$  mode). Each bunch of approximately  $4 \times 10^{11}$  particles completes a revolution of the LEP ring with a period of  $8.9 \times 10^{-5}$  s.

The beams are collided in the four instrumented interaction points (see figure 3.1). The rate,  $R$ , of a process is given by  $R = \sigma\mathcal{L}$  where  $\sigma$  is the *cross section* and  $\mathcal{L}$  is the luminosity. A typical luminosity for LEP is  $1.6 \times 10^{31} \text{ cm}^{-2} \text{ s}^{-1}$ . For the process  $e^+e^- \rightarrow Z^0$  at the  $Z^0$  pole, the cross section is approximately  $42 \times 10^{-33} \text{ cm}^2$  and therefore a  $Z^0$  boson is produced about every 2 seconds.

The LEP collider operated in the  $4 \times 4$  mode from 1989 to 1992. After 1992 the ring was upgraded to operate in an  $8 \times 8$  mode. Over the years 1989 to 1995 the LEP collider has operated at centre-of-mass energies at and around the  $Z^0$  pole (91.2 GeV). Approximately 89.6% of data was collected at the  $Z^0$  pole centre of mass energy, 4.43% are approximately 2 GeV below the  $Z^0$  pole and 5.95% are approximately 2 GeV above the  $Z^0$  pole. The LEP beam energy is monitored, using the resonant depolarization method [17], to a precision of about 10 ppm.

## 3.2 The OPAL detector

A detailed description of the OPAL detector is given in reference [18] and references therein. The OPAL detector was designed as a hermetic magnetic spectrometer able to detect all types of interactions occurring in the  $e^+e^-$  collisions at LEP. Figure 3.2 shows an isometric view the OPAL detector. The detector is constructed cylindrically and coaxial with the LEP beam pipe<sup>1</sup> with a barrel region that covers approximately  $|\cos\theta| \leq 0.81$  and endcap regions that extend down to  $|\cos\theta| \leq 0.98$ .

The  $e^+e^-$  interactions take place in a 10.7 cm diameter beryllium beam pipe surrounded by the inner tracking detectors (see figure 3.3) that measure the direction

---

<sup>1</sup>The OPAL coordinate system defines the  $+z$  axis in the  $e^-$  beam direction. The angle  $\theta$  is measured from the  $+z$  axis and  $\phi$  is measured about the  $z$  axis from the  $+x$  axis which points to the centre of the LEP ring.

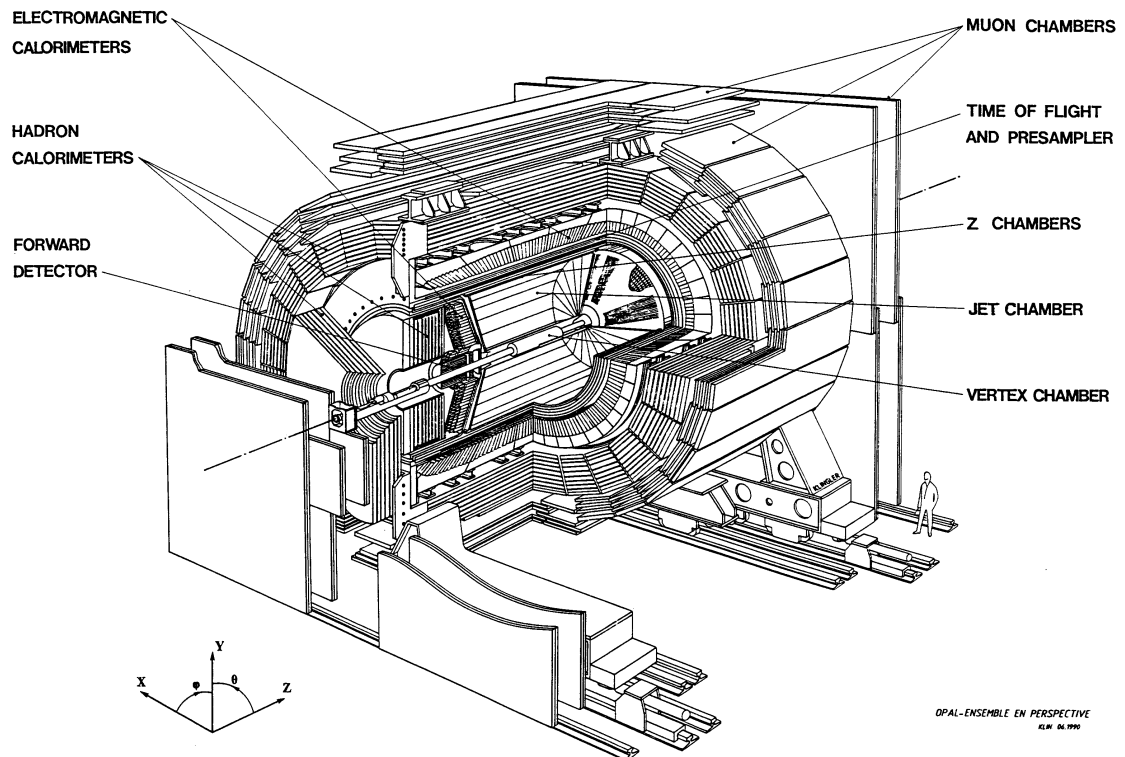


Figure 3.2: Cut away drawing of the OPAL detector showing the major subdetector components. The electron beam runs along the  $+z$  axis and the  $+x$  axis points to the centre of the LEP ring.

and energy loss ( $dE/dx$ ) of charged particles. A solenoidal magnet, located outside the the inner tracking detectors provides a magnetic field of 0.435 T in the direction of the electron beam allows the measurement of the momenta of charged particles. Outside the inner tracking detectors are calorimeters that measure the energy of all particles and a set of detectors for detecting muons. The following sections describe the OPAL detector components in order of increasing radius from the beam.

### 3.2.1 The inner tracking detectors

Immediately surrounding the beam pipe is the silicon (SI) microvertex detector [19] that consists of two concentric cylinders of detectors. The inner cylinder is divided azimuthally into 11 “ladders”, each with three pairs of back-to-back detectors, where one measures in the  $\phi$  direction and the other in the  $z$  direction. The outer cylinder has 14 similar ladders. The inner and outer ladders are arranged to avoid gaps in  $\phi$  coverage. The SI detector covers a solid angle of  $|\cos \theta| \leq 0.80$  and has a track position resolution in  $\phi$  of  $10 \mu\text{m}$  and in  $z$  of  $15 \mu\text{m}$ .

After the SI detector there are three drift chambers that operate in a common gas mixture (88.2% argon, 9.8% methane, 2.0% isobutane) held at a pressure of 4 bar that optimizes the  $dE/dx$  separation between particles yet minimizes the effects due to multiple scattering and diffusion [20].

The innermost drift chamber is the 1 m long cylindrical central vertex detector [21] (CV), with an inner radius of 88 mm and an outer radius of 235 mm, used to detect the secondary vertices of short-lived decay particles from  $e^+e^-$  collisions. The detector consists of an inner cylinder of 36 cells with 12 axial anode wires each and an outer layer of 36 similar cells with 6 stereo ( $4^\circ$ ) anode wires. Charged particles ionize the gas mixture and the resulting charge “trail” or “track” is collected on the anode

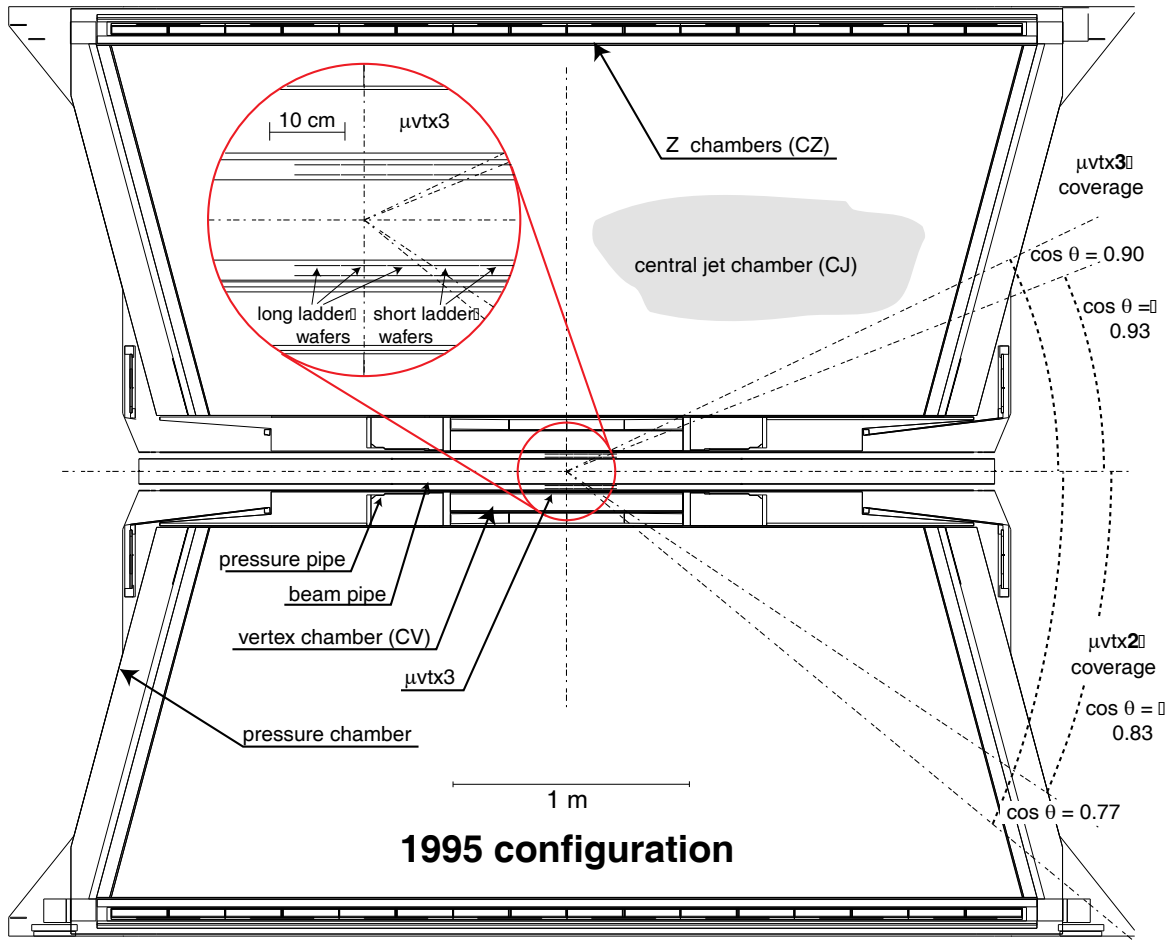


Figure 3.3: Cut away drawing of the inner detector showing the arrangement of the major components. From the centre outwards there are: the silicon microvertex detector (SI); the central vertex (CV) detector; central jet (CJ) chamber and the  $z$  chambers (CZ).

wires. Measurements in the  $r$ - $\phi$  plane and  $z$  direction are obtained by measuring the absolute charge collected on each anode wire and the time difference between the ends of each anode wire respectively. The stereo wires improve the measurement of a track's polar angle and thus allow a precision measurement of its  $z$  coordinate. This detector measures charged track position with resolutions of  $55 \mu\text{m}$  in  $\phi$  and  $700 \mu\text{m}$  in  $z$  [18].

The next detector is the large volume central jet chamber [22] (CJ). This detector is 4 m long and has an inner radius of 250 mm and an outer radius of 1850 mm. The chamber is divided into 24 sectors in  $\phi$  each with 159 anode wires separated by two cathode planes. The wires form radial planes within each sector and run parallel to the beam. This coverage results in at least 8 measured points on a track in 98% of the solid angle. The average number of CJ hits for the tracks used in this thesis is 150. A measurement of the ionization charge collected per wire is made at the ends of each anode wire. The wire position, the drift time to a wire and the ratio of the charge collected at each end of a wire provides information on the  $r$ ,  $\phi$  and  $z$  of a track respectively. CJ has an  $r$ - $\phi$  resolution of  $135 \mu\text{m}$  and a  $z$  resolution of 6 cm. Tracks that curve through the CJ chamber under the influence of the magnetic field are sampled by up to 159 wires. The radius of curvature of tracks can be measured and, knowing the strength of the magnetic field, their momentum can be measured with the following resolution of

$$\sigma_p/p^2 = 2.2 \times 10^{-3} \text{ GeV}^{-1} \quad (3.1)$$

where momentum,  $p$ , is in GeV.

The ionization energy loss of a particle as it travels through the gas mixture,  $dE/dx$ , is calculated using the total charge collected on all wires. The rate of energy



loss is given by the Bethe-Bloch equation [23] and is dependent on the particle velocity. Simultaneous measurement by CJ of the  $dE/dx$  and momentum of a particle gives a measure of the particle mass.

The  $z$ -chambers (CZ) measure the  $z$  position of particle tracks and are the last of the inner detectors in the gas pressure vessel. This detector consists of twenty four 4 m long drift chambers divided in the  $z$  direction into 8 cells. Each cell has six anode wires that run in the  $\phi$  direction and are located at different radii. Measurements of the drift time to a wire and the wire position give a  $z$  measurement with a resolution of  $300 \mu\text{m}$ .

The resolution of the combined CV-CJ-CZ tracking system [18] is  $75 \mu\text{m}$  in the  $r$ - $\phi$  direction and 2 mm (2.7 cm) in the  $r$ - $z$  direction with (without) CV stereo wire information.

### 3.2.2 Solenoid magnet and time of flight detector

The OPAL magnet [18] consists of a solenoid coil and an iron return yoke. The coil surrounds the inner detectors (described in section 3.2.1) and provides a magnetic field, aligned with the LEP electron beam direction, of 0.435 T used to make momentum measurements in the inner detectors. The magnetic flux is returned through the multi-layer iron yoke that forms the absorber for the hadron calorimeter (described in section 3.2.3).

Immediately outside the solenoid is the time of flight (TOF) detector that consists of 160, 6.84 m long scintillation counters that are arranged as a 2.36 m radius cylinder coaxial with the solenoid. The scintillation light is measured at each end of the counters and a timing resolution of 360 ps is achieved. The TOF detector is used to reject cosmic ray events that have an expected flight time across the detector of

7.87 ns. Also the TOF detector is included in the OPAL trigger, a TOF signal within 50 ns of a known beam crossing time is required for a good event.

### 3.2.3 The calorimeters

The calorimeters primarily measure the energy of charged and neutral particles. Energy from electrons and photons is measured with an electromagnetic shower presampler and calorimeter combination. Energy from hadrons (eg,  $\pi^-$ ,  $K^-$  or protons) is measured not only using the electromagnetic presampler and calorimeter but also the hadron calorimeter.

Since there is material in front of the electromagnetic calorimeter, due mostly to the pressure vessel and the solenoid, most electromagnetic showers are initiated<sup>2</sup> well before the electromagnetic calorimeter itself. A high granularity presampler is placed in front of the electromagnetic calorimeter to try to improve the position and energy measurements of these showers. The presampler is divided into the barrel (PB) and endcap parts (PE). The PB detector consists of 16 wire chambers operating in limited streamer mode [24], 6623 mm long, arranged in a cylinder of radius 2388 mm. Each chamber has two layers of 24 cells that run axially and are read out by cathode strips oriented at 45° to provide both  $\phi$  and  $z$  position measurements.

The electromagnetic calorimeter is separated into three parts: a barrel section (EB) that covers  $|\cos\theta| \leq 0.82$  and two endcap sections (EE) that cover  $0.81 \leq |\cos\theta| \leq 0.98$ . If an event deposits energy near the boundaries of EB then EE is checked to see if any energy has leaked across the boundary.

---

<sup>2</sup>Material is measured in *radiation lengths*,  $X_0$ , for electromagnetic particles. One  $X_0$  is the distance that an electron travels in a material such that its energy is reduced by a factor of  $e$  by bremsstrahlung. The *conversion length*  $l_\gamma \equiv 9X_0/7$  is the depth of material that a photon traverses with a 68% probability of converting to an  $e^+e^-$  pair and starting an electromagnetic shower.

The barrel electromagnetic calorimeter consists of 9440 SF57 [25] lead glass blocks arranged as a cylinder, with 160 (59) blocks in the  $z$  ( $\phi$ ) direction. Each lead glass block has a depth of  $24.6 X_0$ , dimensions  $10 \times 10 \text{ cm}^2$  ( $40 \times 40 \text{ mrad}^2$ ) at the inner face and the Čerenkov light from the particle showers is detected by a phototube. The longitudinal axes of the blocks point to the interaction region to minimize the possibility of a particle traversing many blocks. Additionally the blocks are offset slightly in the  $z$  and  $\phi$  directions to prevent a neutral particle from completely escaping through the small inter-block gaps.

Relativistic particles that enter a lead glass block undergo electromagnetic interactions that produce a shower of secondary particles. Charged particles within the shower produce Čerenkov light if their velocity is greater than  $c/n$  where  $n$  is the index of refraction of the lead glass blocks. This light is collected by phototubes. The intrinsic energy resolution of the lead glass calorimeter is  $\sigma_E/E = 0.2\% + 6.3\%/\sqrt{E}$  [18] where  $E$  is in GeV. The  $\sim 2 X_0$  of material that causes early showering in front of the electromagnetic calorimeter degrades the resolution to  $\sigma_E/E = 1.1\% + 18.8\%/\sqrt{E}$  [18]. Each endcap electromagnetic calorimeter consists of 1132 CEREN-25 [26] lead glass blocks mounted axially in a dome shape to conform to the ends of the pressure vessel.

The hadron calorimeter (HCAL) is situated behind the electromagnetic calorimeter and measures the energy deposited by hadronic showers and assists in identifying muons. To achieve coverage of 99% of the solid angle the HCAL is made up of a barrel segment, two endcap segments and two pole tip segments. Hadronic showers tend to extend in depth<sup>3</sup> beyond electromagnetic showers and most muons are able

---

<sup>3</sup>Hadronic shower dimensions are characterized in materials by the *interaction length*  $\lambda_{\text{int}}$  which scales with  $A^{1/3}$  where  $A$  is the atomic weight of the medium.  $\lambda_{\text{int}}$  tends to be much larger than  $X_0$ . An interaction length is defined as the mean free path of a particle before undergoing a nuclear

penetrate through the whole OPAL detector.

This analysis uses information from the barrel section of HCAL (HB) that consists of 9 layers of limited streamer mode wire chambers interspersed with the eight 10 cm thick iron layers (a total of  $4 \lambda_{\text{int}}$ ) of the magnet return yoke. HB divides the region  $|\cos \theta| \leq 0.81$  with nine hundred and seventy six  $3.4^\circ \times 7.5^\circ$  areas in  $\theta \times \phi$ . The energy resolution of HB is estimated to be [27]  $\sigma_E/E = 20\% + 63\%/\sqrt{E}$ . The chambers are able to detect the energy of a minimum ionizing muon to help identify these particles.

### 3.2.4 The muon chambers

The muon chambers are located outside the HCAL detectors and are designed to detect and, in this analysis, reject muons against a background of hadrons. Muons are not strongly interacting and do not shower electromagnetically at LEP energies hence muons above 3 GeV emerge from the HCAL. In contrast 99.9% of hadrons are contained in the HCAL. The small number of hadrons or hadronic products that reach the muon chambers do so by one of three methods: in-flight decay of a hadron to a muon; “punchthrough” where the hadron interacts in the HCAL and secondary particles enter the muon chambers; and “sneakthrough” where the hadron fails to interact in the HCAL.

The muon chambers are divided into the barrel region (MB) that covers  $|\cos \theta| \leq 0.72$  and the endcap (ME) sections that cover  $0.67 \leq |\cos \theta| \leq 0.98$ . The MB detector has 110 large area drift chambers arranged in four approximately cylindrical layers, and the ME detector has four layers of limited streamer mode drift tubes positioned perpendicular to the beam. Muons are identified by matching tracks in the inner tracking chambers to tracks in the muon chambers. These tracks can be matched

---

collision.

with spatial resolutions of 1.5 mm in the  $\phi$  direction and 2 mm in the  $z$  direction.

### 3.2.5 Luminosity monitors

The luminosity of the LEP beams is determined by measuring small angle Bhabha scattering processes ( $e^+e^- \rightarrow e^+e^-$ ) close to the beam line in the far forward and backward regions of the OPAL detector. The first luminosity detector in OPAL was a lead-scintillator forward detector [28] (FD) that provided a luminosity measurement with an uncertainty of 0.6%. A high precision silicon-tungsten (SW) sampling calorimeter [29] was installed in 1993 which reduced the luminosity error to 0.1%.

### 3.2.6 Data acquisition System

The OPAL trigger system is synchronized to the LEP beam and selects beam crossings that likely have  $e^+e^-$  interactions. The trigger system [18] detects basic physics topologies by imposing conditions on the subdetector signals and it also rejects backgrounds caused by cosmic rays, interactions of the  $e^+$  or  $e^-$  particles with gas inside the beam pipe or the beam pipe walls. For trigger purposes the  $4\pi$  solid angle of the OPAL detector is divided into 144 bins (6 in  $\theta$  and 24 in  $\phi$ ) that provide fast signals for each beam crossing. A central trigger logic identifies coincidences and back-to-back hits using these fast signals. Events that might contain interesting physics are formed into a single data structure created by the “event builder”.

These events are sent to a filter processor that performs a first analysis and classification of the complete events and rejects undesired background events. After the filter stage the accepted events are sent to a buffered online event reconstruction system (ROPE) that performs a full reconstruction of all events. At the ROPE stage the raw events are archived to magnetic tape and the reconstructed events are

archived to an optical medium (CD).

### 3.2.7 OPAL performance

The OPAL detector has collected LEP phase 1 data (at or near to the  $Z^0$  pole) from August 1989 to October 1995. During this period 5.1 million  $Z^0$  decays to detectable particles were produced at the OPAL interaction point for a total integrated luminosity of  $173 \text{ pb}^{-1}$ . The integrated luminosity as a function of time collected at OPAL is shown in figure 3.4. The analysis in this thesis studies the  $e^+e^- \rightarrow \tau^+\tau^-$  events collected at OPAL between 1991 and 1995.

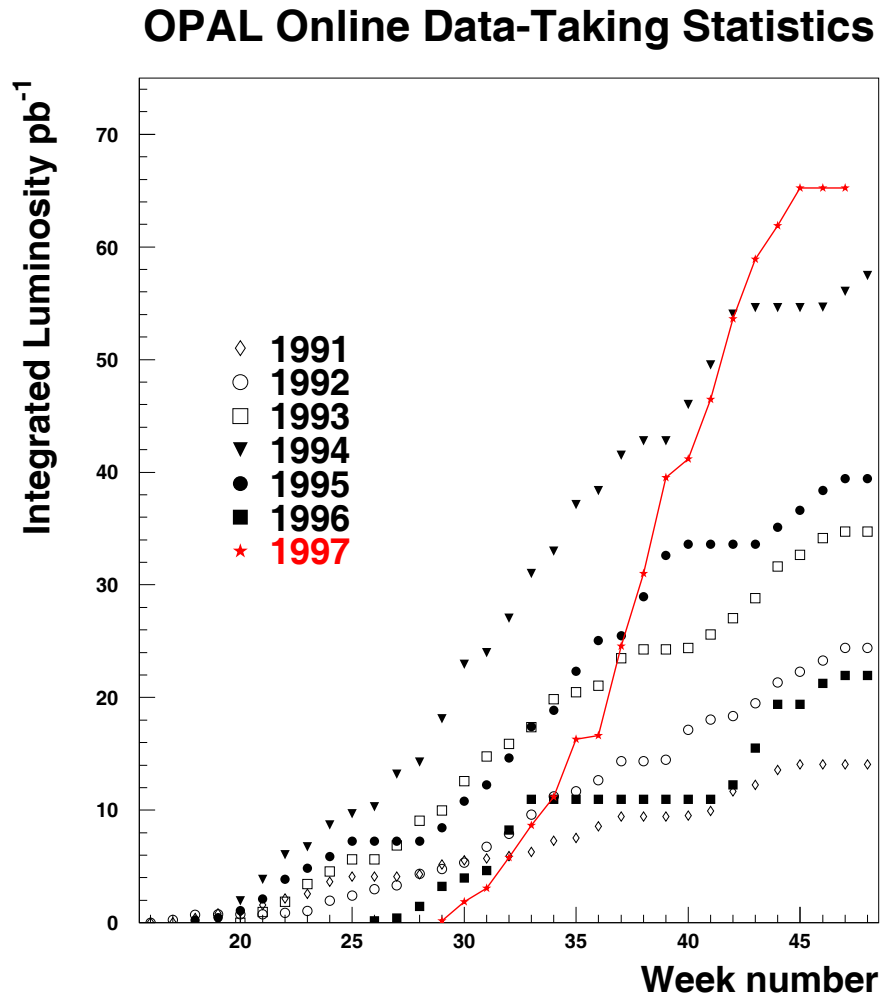


Figure 3.4: The integrated luminosity collected by the OPAL detector as a function of time. The week number is referenced to the LEP start date each year.

# Chapter 4

## Selection of $\tau^+\tau^-$ events

In this chapter we describe the OPAL data set and the simulated data (Monte Carlo) samples that represent our best understanding of the detector response. In the second section the selection of  $e^+e^- \rightarrow \tau^+\tau^-$  events ( $\tau$  pairs) is described.

### 4.1 OPAL data and Monte Carlo

The results presented are based on the data taken between 1991 and 1995 with the OPAL detector at LEP. The integrated luminosity per year is given in Table 4.1. Approximately 89.6% of data was collected at the  $Z^0$  peak centre of mass energy ( $E_{\text{CM}} = 91.2$  GeV), 4.4% are approximately 2 GeV below the  $Z^0$  peak and 6.0% are

Year	Integrated Luminosity
1991	13 pb <sup>-1</sup>
1992	24 pb <sup>-1</sup>
1993	34 pb <sup>-1</sup>
1994	59 pb <sup>-1</sup>
1995	39 pb <sup>-1</sup>
Total	169 pb <sup>-1</sup>

Table 4.1: Integrated luminosity per year.



	CV	CJ	PB	EB	EE	HS	MB	FD
Detector Status	3	3	2	3	3	3	3	3
Trigger Status		2		2	3			

Table 4.2: Table of subdetector and trigger status levels required by the  $\tau$  pair selection. The status levels were developed by each OPAL subdetector working group.

approximately 2 GeV above the  $Z^0$  peak.

The OPAL subdetectors that measure the quantities used for the selection process are required to be in good working order at the time the data are collected. Similarly the detectors used in the trigger logic have to be in a working state to trigger on the types of events required. There are four status levels defined for each detector and trigger: 0 warns that the subdetector is in an unknown state; 1 denotes that the subdetector is off; 2 indicates the subdetector is partly on (for example, some detectors may have regions that no longer operate); 3 means the detector is fully on. Table 4.2 shows the status levels required for each detector used in the analysis. An unspecified trigger status in Table 4.2 implies no requirement is made on that particular trigger.

Simulated events (Monte Carlo) are used to estimate the efficiency for selecting the signal and to estimate the size of the backgrounds in this analysis. The Monte Carlo samples used in this analysis are 300,000  $\tau$  pair events generated at the  $Z^0$  centre-of-mass energy (on-peak) and two samples of 100,000  $\tau$  pair events generated at 2 GeV above and below the  $Z^0$  centre-of-mass energy (off-peak). For this analysis an appropriate number of events from each of the off-peak Monte Carlo runs are added to the on-peak events to reflect the distribution of centre of mass energies in the 1991-1995 data set. These Monte Carlo samples are generated with KORALZ 4.0 [30] and TAUOLA 2.0 [31]. The  $\tau$  pair generator, KORALZ 4.0, takes into account

the following radiative effects:

1. Multiple QED hard bremsstrahlung from the initial state  $e^\pm$  and final state  $\tau^\pm$ ;
2.  $\mathcal{O}(\alpha)$  bremsstrahlung in the  $\tau$  leptonic decay modes and single bremsstrahlung in the other decay channels (leading logarithmic approximation).

The  $\tau$  branching ratios input to KORALZ were the best estimate at the time the Monte Carlo was produced. Over time, more precise measurements have been made (compiled in reference [2]) and we use these newer branching ratios in this work. Each background decay channel is weighted by the ratio of the current world average branching ratio to the Monte Carlo input branching ratio.

The output from KORALZ is then processed by GOPAL [32] that uses the standard CERN package GEANT [33] to track particles through a simulation of the OPAL detector. This stage produces an output of simulated detector responses in exactly the same format as the OPAL data collected from LEP. These samples are then passed through the same reconstruction program (ROPE) as the data. The results are made available to the user through the OPAL (OD) package [34].

It was found that the Monte Carlo unsatisfactorily modelled the dynamics of the  $\tau$  decaying to  $\pi^- 2\pi^0 \nu_\tau$  through the  $a_1$  resonance. Therefore these events in the Monte Carlo sample were reweighted following the procedure described in reference [35].

## 4.2 Selection of $e^+e^- \rightarrow \tau^+\tau^-$ events

An  $e^+e^- \rightarrow Z^0 \rightarrow \tau^+\tau^-$  or  $\tau$  pair *event* recorded in the OPAL detector has a distinctive signature of two back-to-back regions of charged track and electromagnetic calorimeter activity. The  $Z^0$ 's from  $e^+e^-$  collisions are produced at rest and two highly relativistic  $\tau$ 's ( $\beta = 0.9992$ ) are produced “back-to-back” or opposite in momentum

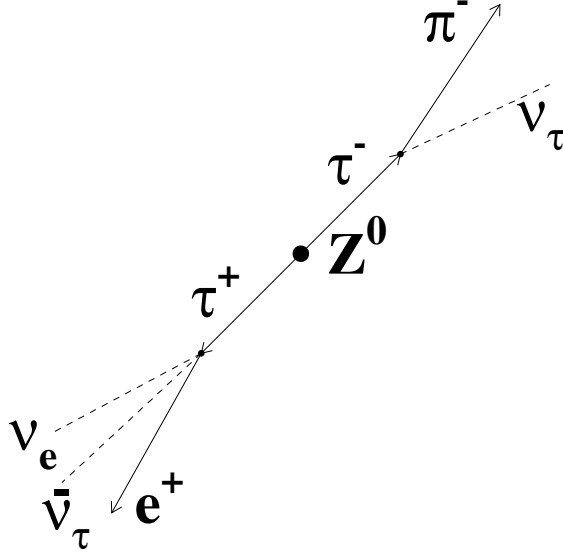


Figure 4.1: A schematic picture of the decay  $e^+e^- \rightarrow \tau^+\tau^-$  where the  $\tau^-$  decays to  $\pi^-\nu_\tau$  and the  $\tau^+$  decays to  $e^+\nu_e\bar{\nu}_\tau$ . The  $\tau$ 's are produced back-to-back and their decay products follow in much the same direction.

(see figure 4.1). The mean lifetime of the  $\tau$  is  $\tau_\tau = 291.0 \pm 1.5$  fs [2] and hence travels an average distance of  $\gamma c\tau_\tau = 2.24$  mm before decaying. The decay products of a highly relativistic  $\tau$  are contained in a narrow cone about the  $\tau$  direction of motion. The charged decay products produce tracks in the inner tracking detectors while both the charged and neutral decay products deposit energy in the electromagnetic and possibly hadronic calorimeters.

It is possible for cosmic rays or beam-gas interactions to create charged tracks or leave energy in the calorimeters. Hence a set of criteria are applied to identify good tracks and clusters. These requirements, shown in Table 4.3, require that the tracks have at least 20 hits in the CJ detector and that the tracks point back to the interaction point. Electromagnetic calorimeter clusters are required to have a

	Requirement	Variable definition
Good track definition	$N_{\text{CJ}}^{\text{hits}} \geq 20$	$N_{\text{CJ}}^{\text{hits}}$ : number of hits in the jet chamber.
	$P_{\text{T}} \geq 0.1 \text{ GeV}$	$P_{\text{T}}$ : the momentum transverse to the beam direction.
	$ d_0  \leq 2 \text{ cm}$	$ d_0 $ : distance to the beam axis at the point of closest approach.
	$ z_0  \leq 75 \text{ cm}$	$ z_0 $ : track displacement along the beam axis from the interaction point.
	$R_{\text{min}} \leq 75 \text{ cm}$	$R_{\text{min}}$ : radius of the first hit in the jet chamber.
Good Barrel ECAL cluster	$N_{\text{blocks}} \geq 1$	$N_{\text{blocks}}$ : number of ECAL blocks in cluster.
	$E_{\text{clusters}} \geq 0.1 \text{ GeV}$	$E_{\text{clusters}}$ : total energy in cluster.
Good end-cap ECAL cluster	$N_{\text{blocks}} \geq 2$	$N_{\text{blocks}}$ : number of ECAL blocks in cluster.
	$E_{\text{clusters}} \geq 0.2 \text{ GeV}$	$E_{\text{clusters}}$ : total energy in cluster.

Table 4.3: Good charged track and ECAL cluster definitions for the  $\tau$  pair selection.

minimum energy of 0.1 GeV in the barrel and 0.2 GeV in the endcap.

The individual  $\tau$ 's in the  $e^+e^- \rightarrow \tau^+\tau^-$  event are identified using a jet finding algorithm [36]. A *jet* is defined to be a narrow or collimated concentration of activity in the detector caused by the passage of energetic particles. Typically 2 jets are found in these events, corresponding to the  $\tau$ 's.

The jet direction is initially set to the direction defined by the highest energy good track or electromagnetic calorimeter fine cluster. Afterwards the next highest energy track or cluster within a cone of half-angle of  $35^\circ$  is added and the jet direction redefined by the vector sum. This second step is repeated until no more tracks or clusters are left. This jet finding algorithm is applied to all events in the 1991-1995 OPAL data set.

The  $\tau$  pair selection [37], summarised in Tables 4.4 and 4.5, starts by selecting

events with two jets, each with at least one good charged track and

$$E_{\text{ECAL}} + E_{\text{track}} > 0.01 E_{\text{CM}},$$

where  $E_{\text{track}}$  is the scalar sum of the momenta of the good charged tracks,  $E_{\text{ECAL}}$  is the total energy of the good clusters in the ECAL,  $E_{\text{CM}}$  is the centre-of-mass energy of the  $e^+e^-$  beams. The average value of  $|\cos\theta|$  for the two jets must be less than 0.68, restricting the analysis to the well-understood barrel region of the OPAL detector.

Cosmic and beam backgrounds are rejected by placing requirements on the time of flight detector. Additional requirements are needed to separate the  $\tau^+\tau^-$  events from other two fermion background ( $e^+e^- \rightarrow f^+f^-$ ) events:

- Multihadronic events ( $e^+e^- \rightarrow q\bar{q}$ ) at the LEP energy are characterised by large track and cluster multiplicities. These events are rejected by requiring  $2 \leq N_{\text{track}} \leq 6$  and  $N_{\text{ECAL}} \leq 10$  where  $N_{\text{track}}$  is the number of good charged tracks per event and  $N_{\text{ECAL}}$  is the number of good ECAL clusters per event.
- Bhabha events ( $e^+e^- \rightarrow e^+e^-$ ) are characterised by back-to-back high energy charged particles that deposit close to the centre-of-mass energy ( $E_{\text{CM}}$ ) in the ECAL. Bhabha events are rejected by requiring the  $\tau$  pair candidates to have  $E_{\text{ECAL}} \leq 0.8E_{\text{CM}}$  or  $E_{\text{ECAL}} + 0.3E_{\text{track}} \leq E_{\text{CM}}$ .
- Muon pair events ( $e^+e^- \rightarrow \mu^+\mu^-$ ) are identified as two high momentum back-to-back charged tracks that leave little energy in the ECAL. These events are removed if the charged tracks have associated activity in the muon detectors or hadronic calorimeter and  $E_{\text{ECAL}} + E_{\text{track}} > 0.6E_{\text{CM}}$ .

	Requirements	Variable definition
Good event	$N_{\text{jet}} = 2$ $ \overline{\cos \theta}  < 0.68$ $E_{\text{jet}} \geq 0.01 E_{\text{beam}}$	$N_{\text{jet}}$ : number of jets satisfying the total energy requirement. $ \overline{\cos \theta} $ : average value of $ \cos \theta $ for the two jets. $E_{\text{jet}}$ : total track and cluster energy in jet. $E_{\text{beam}}$ : the energy of the LEP beam.
$e^+e^- \rightarrow q\bar{q}$ Rejection	$1 \leq N_{\text{tracks}} \leq 6$ $N_{\text{clusters}} \leq 10$	$N_{\text{tracks}}$ : number of good tracks in the $\tau$ pair event. $N_{\text{clusters}}$ : the number of good clusters in the $\tau$ pair event.
$e^+e^- \rightarrow e^+e^-$ Rejection	$\sum E_{\text{cluster}} \leq 0.8 E_{\text{CM}}$	$E_{\text{cluster}}$ : energy of ECAL clusters in event. $E_{\text{track}}$ : energy of charged tracks in event.
	or $\sum E_{\text{cluster}} + 0.3 \sum E_{\text{track}} \leq E_{\text{CM}}$	$E_{\text{CM}} = 2 E_{\text{beam}}$
$e^+e^- \rightarrow \mu^+\mu^-$ Rejection	$\sum_{\text{jets}} (E_{\text{cluster}} + E_{\text{track}}) \leq 0.6 E_{\text{CM}}$ and both jets are muons.	
	A jet is found to be a muon if one of the following applies:	
	$N_{\text{layers}}^{\text{MB or ME}} \geq 2$	$N_{\text{layers}}^{\text{MB or ME}}$ : total layers hit in the barrel or end-cap muon detectors associated to the jet.
	$E_{\text{cluster}}^{\text{charged}} < 2.0 \text{ GeV}$	$E_{\text{cluster}}^{\text{charged}}$ : energy of the ECAL cluster associated to the charged track.
	$N_{\text{layers}}^{\text{HCAL}} \geq 4$ $N_{\text{last 3 layers}}^{\text{HCAL}} \geq 1$ $N_{\text{hits/layer}}^{\text{HCAL}} < 2.0$	$N_{\text{layers}}^{\text{HCAL}}$ : number of hit HCAL layers associated to the track. $N_{\text{last 3 layers}}^{\text{HCAL}}$ : number of layers hit in the outer HCAL. $N_{\text{hits/layer}}^{\text{HCAL}}$ : average number of hits per layer for the whole jet.

Table 4.4: The requirements for a good  $\tau$  pair event and rejection of  $e^+e^- \rightarrow q\bar{q}$ ,  $e^+e^- \rightarrow e^+e^-$  and  $e^+e^- \rightarrow \mu^+\mu^-$  backgrounds.

	Requirements	Variable definition
Two-photon Rejection	$\theta_{\text{acol}} \leq 15^\circ$	$\theta_{\text{acol}}$ : the supplement of the angle between the two jets in the $\tau$ pair event.
	$E_{\text{vis}} \geq 0.03E_{\text{CM}}$	$E_{\text{vis}} = \sum_{\text{jet}} \text{Max}(E_{\text{cluster}}, E_{\text{jet}})$
	If $E_{\text{vis}} \leq 0.2E_{\text{CM}}$ then	
	$P_{\text{T}}^{\text{tracks}} > 2.0 \text{ GeV}$ $P_{\text{T}}^{\text{clusters}} > 2.0 \text{ GeV}$	$P_{\text{T}}^{\text{tracks}}$ : scalar sum of track momenta in the event $P_{\text{T}}^{\text{clusters}}$ : sum of ECAL energy in the event.
Cosmic ray Rejection	$ d_0  \leq 5 \text{ mm}$	$ d_0 $ : average distance of all tracks to interaction point.
	$ z_0 _{\text{min}} \leq 20 \text{ cm}$	$ z_0 _{\text{min}}$ : the minimum distance of a track to the interaction point in the $z$ direction.
	$ z_0 _{\text{ave}} \leq 20 \text{ cm}$	$ z_0 _{\text{ave}}$ : average $ z_0 $ of tracks with a good $ z_0 _{\text{min}}$ .
	$ t_{\text{meas}} - t_{\text{exp}}  \leq 10 \text{ ns}$	$t_{\text{meas}}$ and $t_{\text{exp}}$ : the measured and expected times of flight assuming the event is created at the origin.
	If $ \phi_i - \phi_j  \geq 165^\circ$ then reject the event if $ t_{\text{meas}} - t_{\text{exp}}  \geq 10 \text{ ns}$ .	

Table 4.5: The requirements for rejecting the backgrounds from two-photon and cosmic processes.

In addition to the background from two fermion events, there are also two-photon events ( $e^+e^- \rightarrow (e^+e^-)X$ , where  $X = e^+e^-, \mu^+\mu^-, \tau^+\tau^-, q\bar{q}$ ) that must be rejected. Two photon events leave little energy in the detector as the  $e^+$  and  $e^-$  particles are emitted at angles close to the beam and are often undetected. In addition, the detected particles tend to have a large acolinearity<sup>1</sup> angle with respect to each other. These events are rejected by requiring

$$\theta_{\text{acol}} \leq 15^\circ,$$

$$E_{\text{vis}} \geq 0.03E_{\text{CM}},$$

where  $\theta_{\text{acol}}$  is the acolinearity between the two jets and  $E_{\text{vis}}$  is the visible energy and defined as the greater of either  $\sum E_{\text{ECAL}}$  or  $\sum E_{\text{track}}$ . If  $E_{\text{vis}} \leq 0.20E_{\text{CM}}$  then events are rejected if they satisfy

$$P_{\text{T}}^{\text{tracks}} > 2.0 \text{ GeV or } P_{\text{T}}^{\text{clusters}} > 2.0 \text{ GeV}$$

where  $P_{\text{T}}^{\text{tracks}}$  ( $P_{\text{T}}^{\text{clusters}}$ ) is the vector sum of momentum (energy) of all charged tracks (ECAL clusters).

The  $\tau$  pair selection applied to all data collected between 1991 and 1995 yields 95364  $\tau$  pair candidates. The non- $\tau$  background contributions in the sample have been investigated in [38] and are shown in Table 4.6. The  $e^+e^- \rightarrow q\bar{q}$  estimate has been improved [39].

---

<sup>1</sup>The acolinearity angle is the supplement of the angle between two vectors.



Background	Contamination (%)
$e^+e^- \rightarrow \mu^+\mu^-$	$0.72 \pm 0.05$
$e^+e^- \rightarrow e^+e^-$	$0.41 \pm 0.07$
$e^+e^- \rightarrow q\bar{q}$	$0.28 \pm 0.04$
$e^+e^- \rightarrow (e^+e^-)e^+e^-$	$0.07 \pm 0.02$
$e^+e^- \rightarrow (e^+e^-)\mu^+\mu^-$	$0.08 \pm 0.02$
Total	$1.56 \pm 0.10$

Table 4.6: Non- $\tau$  background in the  $\tau$  pair sample.

# Chapter 5

## Selection of one-prong $\tau$ -decays

This chapter describes the selection of jets with one-prong  $\tau$  decays. In the first section, a one-prong decay is defined. The second section gives the requirements that classify a jet as a one-prong and outlines how photon conversions are identified. The last section gives the results of the one-prong selection.

### 5.1 One-prong definition

A *one-prong* decay is defined as a  $\tau$  lepton decaying into the final state of one charged particle plus any number of accompanying neutral particles. This definition of a one-prong decay includes the leptonic  $\tau$  decays and semi-leptonic decays with one charged hadron in the final state.

In Table 5.1 we list the  $\tau$  decays that are included in each channel studied in this thesis. We use the PDG definitions for these signal channels [2]. Note that not all modes were included in the Monte Carlo simulation. A systematic error is assigned to account for the effect of the unmodelled decay modes on the branching ratio measurements.

Selection	Decay mode	Weight	Comment
$\tau^- \rightarrow h^- \nu_\tau$	$\tau^- \rightarrow \pi^- \nu_\tau$		
	$\tau^- \rightarrow K^- \nu_\tau$		
$\tau^- \rightarrow h^- \pi^0 \nu_\tau$	$\tau^- \rightarrow \pi^- \pi^0 \nu_\tau$		
	$\tau^- \rightarrow K^- \pi^0 \nu_\tau$		
$\tau^- \rightarrow h^- \geq 2\pi^0 \nu_\tau$	$\tau^- \rightarrow \pi^- 2\pi^0 \nu_\tau$		
	$\tau^- \rightarrow K^- 2\pi^0 \nu_\tau$		
	$\tau^- \rightarrow \pi^- 3\pi^0 \nu_\tau$		
	$\tau^- \rightarrow K^- 3\pi^0 \nu_\tau$		Not modelled
	$\tau^- \rightarrow h^- 4\pi^0 \nu_\tau$		Not modelled
	$\tau^- \rightarrow \pi^- \bar{K}^0 \nu_\tau$	0.157 <sup>†</sup>	
	$\tau^- \rightarrow K^- \bar{K}^0 \nu_\tau$	0.157 <sup>†</sup>	Not modelled
	$\tau^- \rightarrow \pi^- \bar{K}^0 \pi^0 \nu_\tau$	0.157 <sup>†</sup>	
	$\tau^- \rightarrow K^- K^0 \pi^0 \nu_\tau$	0.157 <sup>†</sup>	Not modelled
	$\tau^- \rightarrow \pi^- K^0 \bar{K}^0 \nu_\tau$	0.0246 <sup>†</sup>	
	$\tau^- \rightarrow \pi^- \pi^0 \eta \nu_\tau$	0.319*	

<sup>†</sup> Only the  $K_S^0 \rightarrow 2\pi^0$  decay included.

\* Only the  $\eta \rightarrow 3\pi^0$  decay included.

Table 5.1: The various possible decay modes for each signal selection. The weights reflect the fraction of each decay that contributes to the signal. The weight is equal to unity when no number is explicitly given. A number of the decay modes were not simulated in the Monte Carlo and these are indicated in the last column.

## 5.2 One-prong selection

Jets with one good track are identified as one-prong decays. Jets with 2 or 3 good tracks may also be identified as one-prong decays if the additional tracks are associated with a photon conversion. The track not identified as a conversion electron is henceforth called the *primary track*.

Occasionally a  $\pi^0$  may decay to an  $e^+e^-\gamma$  final state (Dalitz decay) or one of the photons from a  $\pi^0 \rightarrow \gamma\gamma$  decay may convert to an  $e^+e^-$  pair, also resulting in an  $e^+e^-\gamma$  final state. In the case of Dalitz decays, the  $e^+e^-$  will originate at the point of

the  $\tau$  decay, while an  $e^+e^-$  pair from a photon conversion will likely originate from a location in the detector where there is material present.

Conversion pairs, including  $e^+e^-$  from Dalitz decays ( $\pi^0 \rightarrow \gamma e^+e^-$ ), are identified in  $\tau$  jets using a standard OPAL conversion finding algorithm [40]. All jets with 2 or 3 good tracks are considered as candidates to contain conversion pairs. If a jet has 2 or 3 good charged tracks, then each track is individually subjected to the conversion finding algorithm. For each input track, the algorithm searches through all the tracks in the jet and returns the identity of a candidate that has the highest probability of forming a conversion pair with the input track. A conversion pair is identified if the conversion finding routine indicates a probability greater than 95%. The candidate track is not necessarily a good track; the only quality requirement being that the candidate track have at least 20 CJ hits and points to the primary vertex. This means there are jets with only two “good” tracks, one of them an electron from a conversion that has been paired with a track segment not normally considered as “good” track.

The radial distance of the conversion origin is shown in figure 5.1. The discrepancies between data and Monte Carlo at low radii are due to inaccuracies in the Monte Carlo modelling of material in the OPAL detector and inadequacies in the modelling of Dalitz decays. The systematic error due to Dalitz decays of the  $\pi^0$  is eliminated by a requirement that all the conversion pair candidates have a vertex with a radial distance greater than 4 cm.

### 5.3 Results

A total of 158971 one-prong jets are selected of which 5960 are jets with 2 tracks and 1903 are jets with 3 tracks. Figure 5.2 shows the number of tracks per one-prong jet.

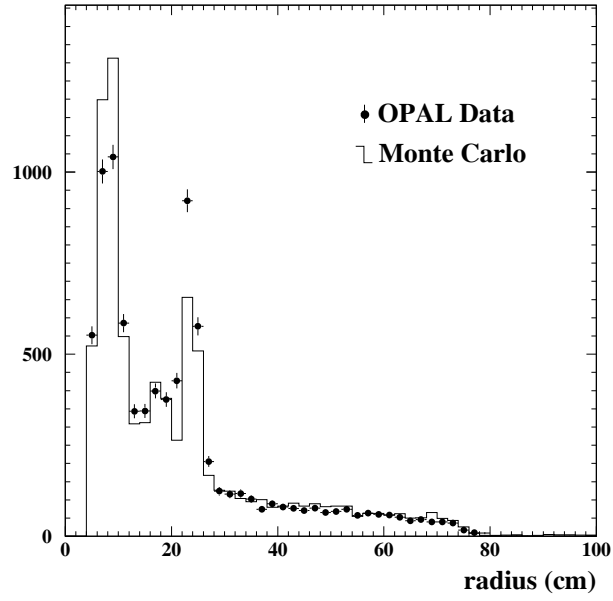


Figure 5.1: Conversion vertex radius of identified  $e^+e^-$  pairs in good one-prong events.

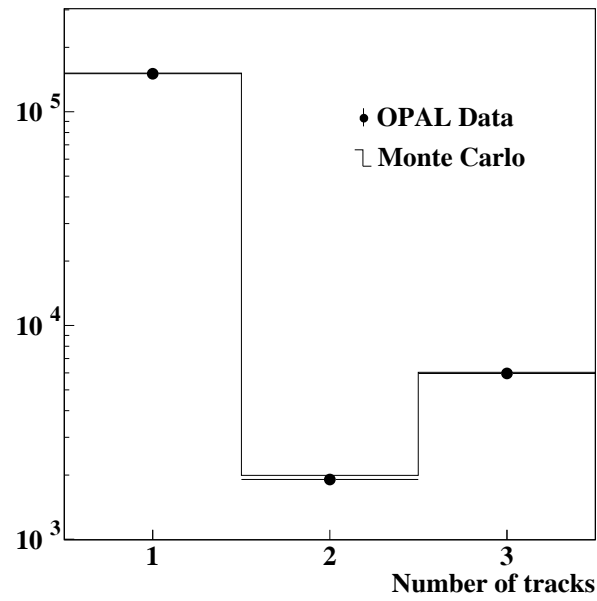


Figure 5.2: The number of tracks in one-prong jets. Jets with more than one track have an identified conversion  $e^+e^-$  pair.

# Chapter 6

## $\pi^0$ Identification

The jets identified as one-prong decays are now classified as jets with 0, 1 or  $\geq 2$   $\pi^0$ 's. The  $\pi^0$ 's decay predominantly to two photons ( $\pi^0 \rightarrow \gamma\gamma$ ) and we need an accurate estimate of the energy and position of each  $\gamma$ . A fine clustering algorithm, outlined in the first section, is used to find localized depositions of energy in the electromagnetic calorimeter. After the fine clustering algorithm a matching routine, described in the second section, is used to see whether the electromagnetic calorimeter clusters are associated to the charged track(s) in each one-prong jet. The next section describes the corrections made to the electromagnetic calorimeter clusters, charged tracks and  $E/p$  variable in the Monte Carlo sample to improve the agreement with the data. The fourth section of this chapter gives the definition of neutral clusters in the electromagnetic calorimeter. Using the information above, the  $\pi^0$ 's are counted in each one-prong jet and the jets are classified as having 0, 1 or  $\geq 2$   $\pi^0$ . In the fifth section the basic topologies of the  $\pi^0 \rightarrow \gamma\gamma$  decay are presented. The last section of this chapter outlines the algorithm that identifies the  $\pi^0$ 's in one-prong jets.

## 6.1 Fine clustering algorithm

As discussed in section 3.2.3, the electromagnetic calorimeter consists of 9440 lead-glass blocks each of which subtend a solid angle of  $40 \times 40 \text{ mrad}^2$  with a depth of  $24.6X_0$ . Electrons and photons will deposit almost all of their energy in the electromagnetic calorimeter whereas hadrons deposit about one third of their energy in the electromagnetic calorimeter with the remaining energy appearing in the hadron calorimeter [41].

A shower from an electron or photon is narrow and well defined and greater than 99% of the particle's energy is deposited and contained in the  $24.6 X_0$  lead-glass electromagnetic calorimeter. Electromagnetic showers are almost entirely contained within a cluster of  $2 \times 2$  blocks. The shape of a shower produced by a hadron varies widely [42] but it is found that a  $2 \times 2$  block cluster will contain approximately 95% of the energy deposited in the electromagnetic calorimeter.

A fine clustering algorithm [43, 44] is used to form the energy clusters from the blocks in the barrel electromagnetic calorimeter. This clustering algorithm replaces the standard algorithm used in the OPAL OD [34] package which does not search for local maxima, limiting the power to resolve individual particles.

The fine clustering algorithm searches for electromagnetic calorimeter blocks that are local energy maxima. Clusters limited to  $2 \times 2$  block size are formed around these maxima according to criteria detailed in reference [43]. The position of these clusters is determined using a cube-root energy weighting scheme [43, 45]. The energy and polar angle ( $\theta$ ) of all electromagnetic calorimeter clusters are corrected for the material in front of the electromagnetic calorimeter with a standard OPAL energy correction routine.



## 6.2 Charged track-fine cluster matching

A cluster from a photon or other neutral particle is distinguished from a cluster created by a charged particle by examining whether any track points to the cluster.

The cluster-track matching is made using a  $\chi^2$  variable that uses the position and uncertainty in position in  $\theta$  and  $\phi$  of the electromagnetic calorimeter clusters  $(\theta_{\text{clust}}, \phi_{\text{clust}})$  and the extrapolation of tracks to the electromagnetic calorimeter face  $(\theta_{\text{track}}, \phi_{\text{track}})$ . This variable is defined in  $\theta$  and  $\phi$

$$\chi_{\theta}^2 \equiv \frac{(\theta_{\text{clust}} - \theta_{\text{track}})^2}{(\sigma_{\text{clust}}^{\theta})^2 + (\sigma_{\text{track}}^{\theta})^2} \quad \chi_{\phi}^2 \equiv \frac{(\phi_{\text{clust}} - \phi_{\text{track}})^2}{(\sigma_{\text{clust}}^{\phi})^2 + (\sigma_{\text{track}}^{\phi})^2}$$

where  $\sigma_{\text{clust}}^{\theta}$  ( $\sigma_{\text{track}}^{\theta}$ ) and  $\sigma_{\text{clust}}^{\phi}$  ( $\sigma_{\text{track}}^{\phi}$ ) are the uncertainty in  $\theta$  and  $\phi$  of electromagnetic calorimeter clusters (tracks). The uncertainty in  $\theta$  and  $\phi$  of electromagnetic calorimeter clusters was measured to be 9 mrad [44].

An electromagnetic calorimeter cluster and track are considered association candidates if both  $\chi_{\theta}^2 < 16$  and  $\chi_{\phi}^2 < 16$  ( $4\sigma$  agreement). Each track may be associated to a maximum of one electromagnetic calorimeter cluster. If more than one track points to a single cluster then the track-cluster pair with the smallest  $\chi_{\text{total}}^2$  is considered associated where

$$\chi_{\text{total}}^2 \equiv \sqrt{(\chi_{\theta}^2)^2 + (\chi_{\phi}^2)^2}.$$

## 6.3 Monte Carlo optimization

The Monte Carlo sample is a close approximation of the data, however a number of variables in the Monte Carlo are adjusted in order to improve the agreement with the data.

### 6.3.1 Charged track corrections

The momentum resolution of the tracks in the Monte Carlo is slightly better than observed in the data. As a result the transverse momentum ( $p_T$ ) of Monte Carlo tracks is smeared<sup>1</sup> by

$$\frac{\Delta p_T}{p_T^2} = 0.0009$$

to match the data momentum spectrum. This factor was determined by studying the momentum resolution of  $e^+e^- \rightarrow \mu^+\mu^-$  events [46] (a similar result was found later in [47]).

In addition, if a charged particle passes close to the anode plane it is possible that the resulting track is split across the plane and a track segment on one side is not associated to the opposite segment(s). Thus a single track can be split into two tracks and can cause a good  $\tau$  jet to be rejected later in the analysis.

Tracks that appear to be split by the anode plane are identified and corrected by requiring:

- Jets with exactly two (at least one track is good) tracks are considered;
- The sum of CJ hits for the two tracks must be less than 200;
- The  $\phi$  position of the highest momentum track must be within  $1.7^\circ$  of the sector anode plane (located at  $7.5^\circ$  within each  $15^\circ$  CJ sector);

If the requirements above are met then the track with fewer CJ hits is discarded. The systematic effect of the anode plane on the final results is considered later in section 8.3.

---

<sup>1</sup>The smearing procedure assumes that the data and Monte Carlo resolutions are gaussian. Smearing is achieved by convoluting the Monte Carlo quantity with an appropriate gaussian distribution in order to match the data.

### 6.3.2 Energy smearing

It is noted [47] that the electromagnetic calorimeter energy resolution is better in the Monte Carlo than the data. Hence all the Monte Carlo cluster energies are smeared by the quadratic difference in data and Monte Carlo energy resolutions given by [47]

$$\left(\frac{\sigma_E}{E}\right)_{\text{data}} = 0.011 + \frac{0.188}{\sqrt{E}}$$

$$\left(\frac{\sigma_E}{E}\right)_{\text{MC}} = 0.01 + \frac{0.170}{\sqrt{E}}$$

where  $E$  is the electromagnetic calorimeter cluster energy in GeV.

The resulting agreement between data and Monte Carlo in the electromagnetic calorimeter cluster energies is shown in Figure 6.1<sup>2</sup>. Figure 6.1 shows the energy of the highest and second highest energy clusters unassociated to a charged track for both Monte Carlo and data after the energy corrections and smearing. The good agreement in energies after the energy correction and Monte Carlo smearing gives us confidence that the electromagnetic cluster forming routines are well understood.

### 6.3.3 $E/p$ variable

The association of tracks and electromagnetic calorimeter clusters allows the formation of the  $E/p$  variable, defined as the energy ( $E$ ) of the electromagnetic calorimeter cluster associated to a charged track divided by the track momentum ( $p$ ). This variable is used to reject  $\tau^- \rightarrow e^- \bar{\nu}_e \nu_\tau$  decays from the  $\tau^- \rightarrow h^- \nu_\tau$  sample and identify  $\pi^0$ 's that are close to the charged track in the  $\tau^- \rightarrow h^- \geq 2\pi^0 \nu_\tau$  sample. The  $E/p$  distribution for events selected as one-prongs (section 5.2) is shown in figure 6.2. The

---

<sup>2</sup>The Monte Carlo distributions shown in all figures are normalized to the number of events after the  $\tau$  pair selection. The  $\tau$  branching ratios used are those published in the PDG [2] except for the signal channels where the results of this analysis are used.

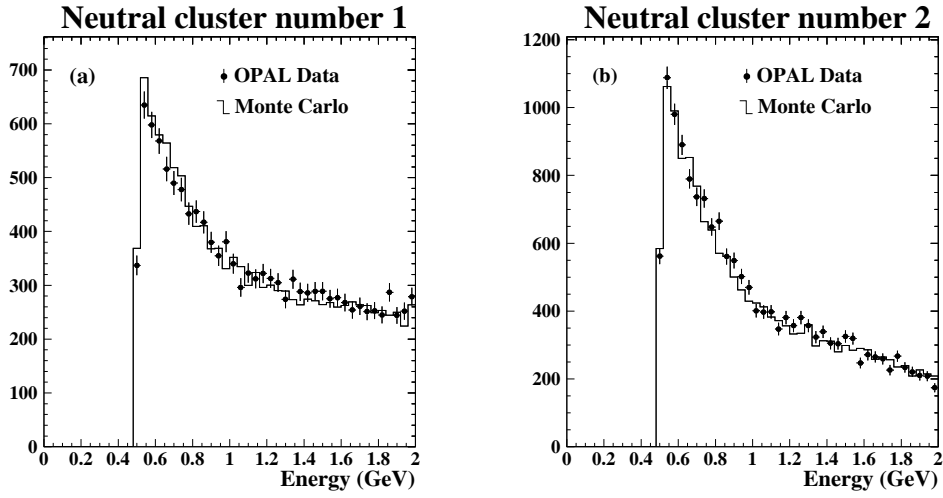


Figure 6.1: The energy of clusters unassociated to a charged track after all corrections are made. Figures (a) and (b) show the energy of the highest energy and second highest energy neutral clusters in both data and Monte Carlo respectively.

width of  $E/p$  for Monte Carlo  $\tau^- \rightarrow e^- \bar{\nu}_e \nu_\tau$  decays is observed to be too narrow when compared to data and a smearing factor is introduced. The  $E/p$  for Monte Carlo  $\tau^- \rightarrow e^- \bar{\nu}_e \nu_\tau$  decays is modified by smearing the electromagnetic calorimeter energy by

$$\sigma_E = 0.015 + \frac{0.08}{\sqrt{E_{\text{raw}}}}$$

where  $E_{\text{raw}}$  is the associated cluster energy before the smearing described in section 6.3.2.

## 6.4 Neutral electromagnetic clusters

An electromagnetic calorimeter cluster that is not associated to a charged track and has an energy<sup>3</sup> of at least 0.5 GeV is called a *neutral cluster*. Figure 6.3 shows the

---

<sup>3</sup>The energy and momentum cuts presented here are the values used for the  $Z^0$  peak samples. The energy and momentum requirements for the off-peak data and Monte Carlo are scaled by a factor

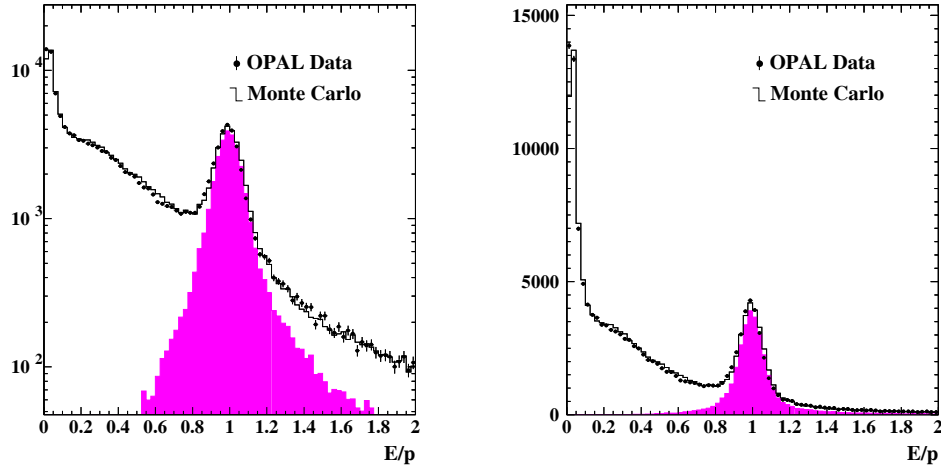


Figure 6.2:  $E/p$  distribution for events selected as good one-prongs. The  $\tau^- \rightarrow e^- \bar{\nu}_e \nu_\tau$  events have been smeared as described in the text and are shown as the shaded area in both plots.

number of neutral clusters per one-prong jet.

A pair of tracks identified as a conversion pair are also considered a neutral electromagnetic cluster. The energy and momentum of the neutral cluster is calculated from the momentum of the conversion tracks.

In about one in a hundred  $\tau$  decays there is a neutral cluster in the jet that is created by a radiative photon from the  $\tau$ . If the invariant mass of the primary track and any cluster is greater than 3.0 GeV (much larger than the  $\tau$  mass), then that cluster is not considered a neutral cluster. Figure 6.4 shows the energy of neutral clusters removed by this requirement.

---

dependent on beam energy to correspond with peak values.

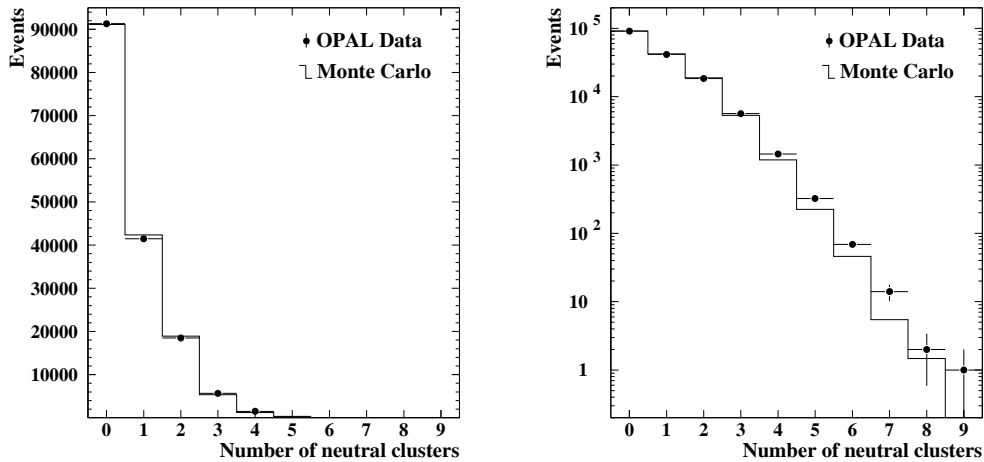


Figure 6.3: The distribution of the number of neutral clusters per jet for one-prong selected jets. The distribution is shown in both a linear vertical scale (left plot) and a logarithmic vertical scale (right plot).

## 6.5 $\pi^0$ topologies

The  $\pi^0$  decays 98.8% of the time into two photons with most of the remaining 1.2% of the decays into an  $e^+e^-\gamma$  final state (Dalitz decay). The  $\pi^0$ 's from  $\tau$  decays at LEP are highly relativistic and the two photons from the  $\pi^0 \rightarrow \gamma\gamma$  decay will usually be very close to each other. For example, 90% of the two  $\gamma$ 's from a 9.0 GeV  $\pi^0$  are within 43 mrad of each other. Since an electromagnetic calorimeter block is typically 40 mrad in both the  $\theta$  and  $\phi$  directions, both of these  $\gamma$ 's are likely to enter one or two electromagnetic calorimeter blocks and form a single cluster as shown in figure 6.5(a). As the  $\pi^0$  energy decreases the angle between the  $\gamma$ 's increases and eventually they can be resolved into two electromagnetic calorimeter clusters as shown in figure 6.5(b). Another  $\pi^0$  possible topology occurs when the photons from the  $\pi^0 \rightarrow \gamma\gamma$  decay travel close to the charged hadron in a one-prong jet. The energy deposited in the

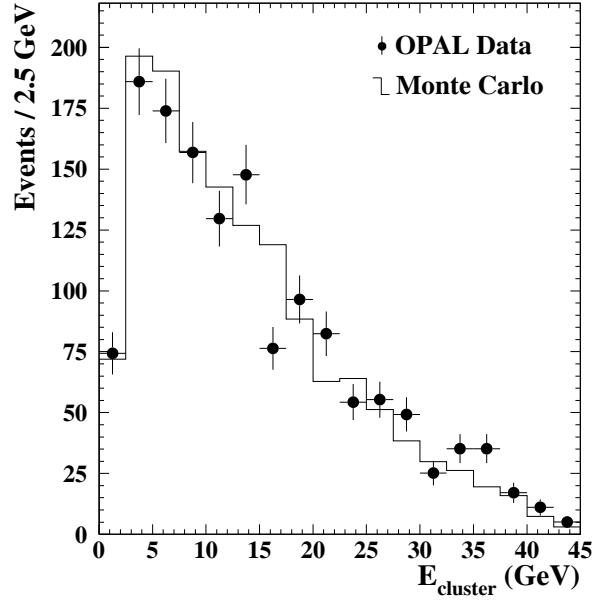


Figure 6.4: Energy of the clusters identified as originating from radiative photons.

electromagnetic calorimeter by the  $\gamma$ 's and the hadron merges and forms a single cluster that is associated to the track as shown in figure 6.5(c).

The behaviour of  $\pi^0$ 's in the electromagnetic calorimeter was studied by creating a sample of 70,000 Monte Carlo  $\pi^0$ 's ( $\pi^0$  Monte Carlo) with momentum 2 GeV to 15 GeV in the barrel region of the OPAL detector. This sample was used to aid in the determination of the energy thresholds in the  $\pi^0$  identification algorithm. Figure 6.6 shows the fraction of  $\pi^0$ 's that form one or two electromagnetic calorimeter clusters as a function of the  $\pi^0$  energy. The clusters are required to have a minimum of 0.5 GeV in energy. At  $\pi^0$  energies below 2 GeV the fraction of  $\pi^0$ 's that are detected with two electromagnetic calorimeter clusters is small since the probability of one cluster falling below the 0.5 GeV threshold is high. As the  $\pi^0$  energy exceeds 2 GeV the number of clusters that fall below the 0.5 GeV threshold is reduced and the  $\pi^0$ 's are resolved as

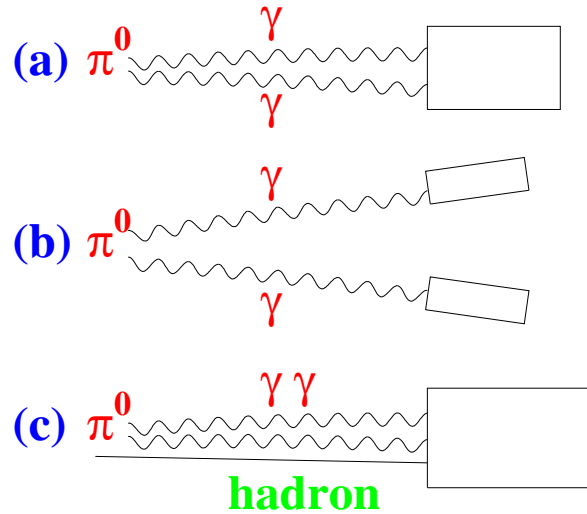


Figure 6.5: (a) shows the photons from a  $\pi^0$  decay forming one electromagnetic calorimeter cluster only. (b) shows a  $\pi^0$  that decays into two photons that deposit two well separated clusters of energy in the electromagnetic calorimeter. (c) shows the photons from the  $\pi^0$  travelling close to the hadronic track and forming a cluster with the energy deposited by the hadron.

two electromagnetic calorimeter clusters. When the  $\pi^0$  energy has reached 9.0 GeV the fraction of  $\pi^0$ 's that can be resolved as two electromagnetic calorimeter clusters has fallen below 20%. Clusters with energy greater than 9.0 GeV are considered  $\pi^0$ 's in the  $\pi^0$  identification algorithm.

## 6.6 $\pi^0$ identification algorithm

The  $\pi^0$  identification algorithm is applied to each one-prong jet. It uses a set of requirements to identify the  $\pi^0$  topologies described above. The number of  $\pi^0$ 's per one-prong jet is not limited but a certain level of interdependency exists between the



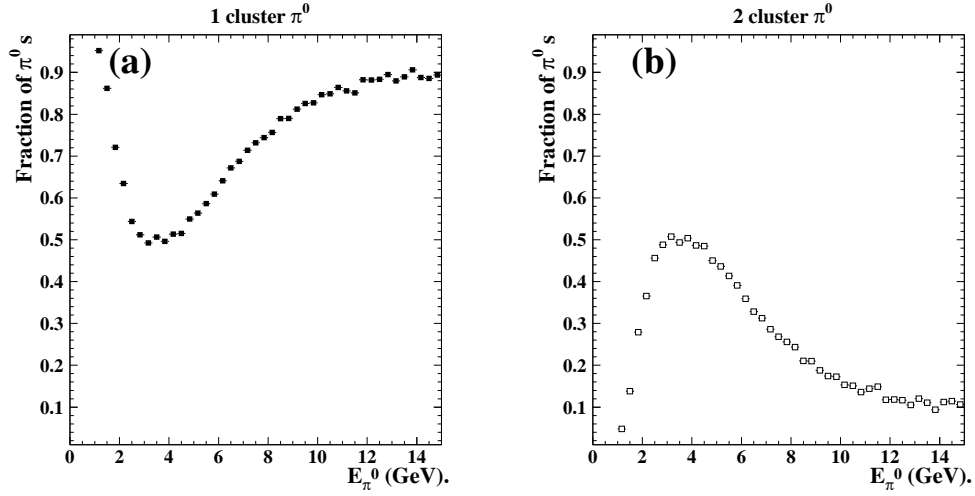


Figure 6.6: (a) shows the fraction of  $\pi^0$ 's with both photons forming a single electromagnetic calorimeter cluster as a function of the  $\pi^0$  energy. (b) shows the fraction of  $\pi^0$ 's with both photons forming two electromagnetic calorimeter clusters as a function of the  $\pi^0$  energy.

topologies. The algorithm used to identify  $\pi^0$ 's in each jet is as follows:

1. Any neutral cluster in the jet with energy ( $E_{NC}$ ) greater than 9.0 GeV is identified as a  $\pi^0$ . In the data-selected samples of  $\tau^- \rightarrow h^- \pi^0 \nu_\tau$  and  $\tau^- \rightarrow h^- \geq 2\pi^0 \nu_\tau$  jets, approximately 56% and 34% of the  $\pi^0$ 's, respectively, are identified by this criterion.
2. Pairs of neutral clusters, or a neutral cluster and photon conversion, each with neutral cluster or photon conversion energy less than 9.0 GeV, are candidates to form a  $\pi^0$ . The pair is considered a  $\pi^0$  candidate if its energy is at least 3 GeV and its invariant mass ( $m_{\gamma\gamma}$ ) is consistent with the  $\pi^0$  mass using a  $\chi_{\pi^0}^2$  requirement. The  $\chi_{\pi^0}^2$  variable is defined as

$$\chi_{\pi^0}^2 \equiv \frac{(m_{\gamma\gamma} - m_{\pi^0})^2}{\sigma_{m_{\gamma\gamma}}^2},$$

where  $m_{\pi^0}$  is the mass of the  $\pi^0$  meson and  $\sigma_{m_{\gamma\gamma}}$  is the calculated uncertainty on  $m_{\gamma\gamma}$ . A pair is considered a  $\pi^0$  if  $\chi_{\pi^0}^2 < 9.0$ .

The number of  $\pi^0$ 's formed in each jet using this method is not limited. If there is an ambiguity between neutral clusters and photon conversion, the combination that gives the best  $\chi_{\pi^0}^2$  is chosen. Figure 6.7 shows the invariant mass distribution of two neutral clusters before and after this selection criterion is applied. In the data-selected samples of  $\tau^- \rightarrow h^- \pi^0 \nu_\tau$  and  $\tau^- \rightarrow h^- \geq 2\pi^0 \nu_\tau$

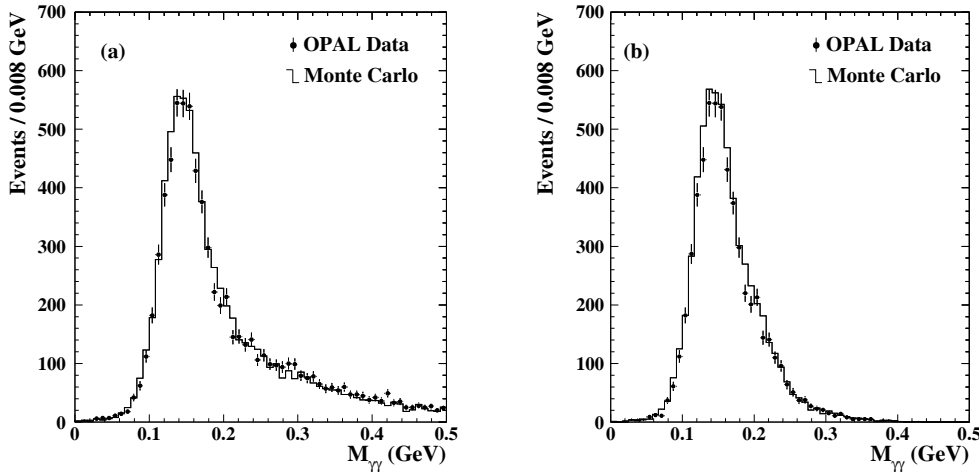


Figure 6.7: (a) The invariant mass distribution of two neutral clusters in data and Monte Carlo for jets with two neutral clusters with energy between 0.5 and 9.0 GeV. (b) The invariant mass distribution for the neutral cluster pairs selected by the  $\pi^0$  algorithm.

jets, approximately 18% and 14% of the  $\pi^0$ 's, respectively, are identified by this criterion.

- Any remaining neutral clusters with  $E_{\text{NC}} > 2.2$  GeV are classified as  $\pi^0$ 's. In the data-selected samples of  $\tau^- \rightarrow h^- \pi^0 \nu_\tau$  and  $\tau^- \rightarrow h^- \geq 2\pi^0 \nu_\tau$  jets, approximately 26% and 33% of the  $\pi^0$ 's, respectively, are identified by this criterion.

4. Frequently the  $\pi^0$  cannot be resolved from a track. If the cluster associated to the track satisfies both

$$E/p > 1.0 ,$$

$$\text{and } E - 0.3p > 2.2 \text{ GeV} ,$$

then we consider the cluster to be an overlap  $\pi^0$ . The energy of the  $\pi^0$  is estimated to be  $E - 0.3p$  where  $E$  is the energy of the cluster (charged hadron plus  $\pi^0$ ). The energy deposited by the charged hadron in the electromagnetic calorimeter is on average one-third of its momentum ( $0.3p$ ). These  $\pi^0$ 's are only permitted in jets where one or more  $\pi^0$ 's are identified by any of cases (1) to (3) above. One-prong jets that reconstruct a single  $\pi^0$  that is an overlap are rejected to reduce the cross-sample contamination from the  $\tau^- \rightarrow h^- \geq 2\pi^0 \nu_\tau$  signal. If one or more conversion tracks point to the electromagnetic calorimeter cluster associated to the primary track then the cluster energy ( $E$ ) is modified by subtracting the momenta of the conversion track(s). In the data-selected samples of  $\tau^- \rightarrow h^- \geq 2\pi^0 \nu_\tau$  jets, approximately 19% of the  $\pi^0$ 's are identified by this criterion.

Each one-prong jet is classified as either  $\tau^- \rightarrow h^- \nu_\tau$ ,  $\tau^- \rightarrow h^- \pi^0 \nu_\tau$  or  $\tau^- \rightarrow h^- \geq 2\pi^0 \nu_\tau$ . Figure 6.8 shows the distributions of the number of  $\pi^0$ 's per jet and the types of  $\pi^0$ 's identified by this algorithm after background rejection (described in chapter 7). The energy distribution of  $\pi^0$ 's in  $\tau^- \rightarrow h^- \pi^0 \nu_\tau$  and  $\tau^- \rightarrow h^- \geq 2\pi^0 \nu_\tau$  jets is shown in figure 6.9.

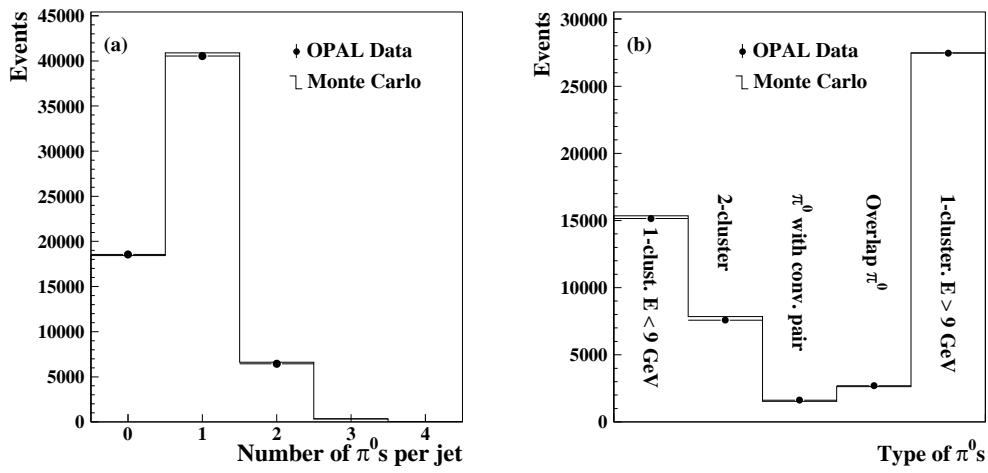


Figure 6.8: (a) The distribution of the number of  $\pi^0$ 's in each one-prong jet identified by the  $\pi^0$  finding algorithm. (b) The distribution of the types of  $\pi^0$ 's identified in one-prong jets.

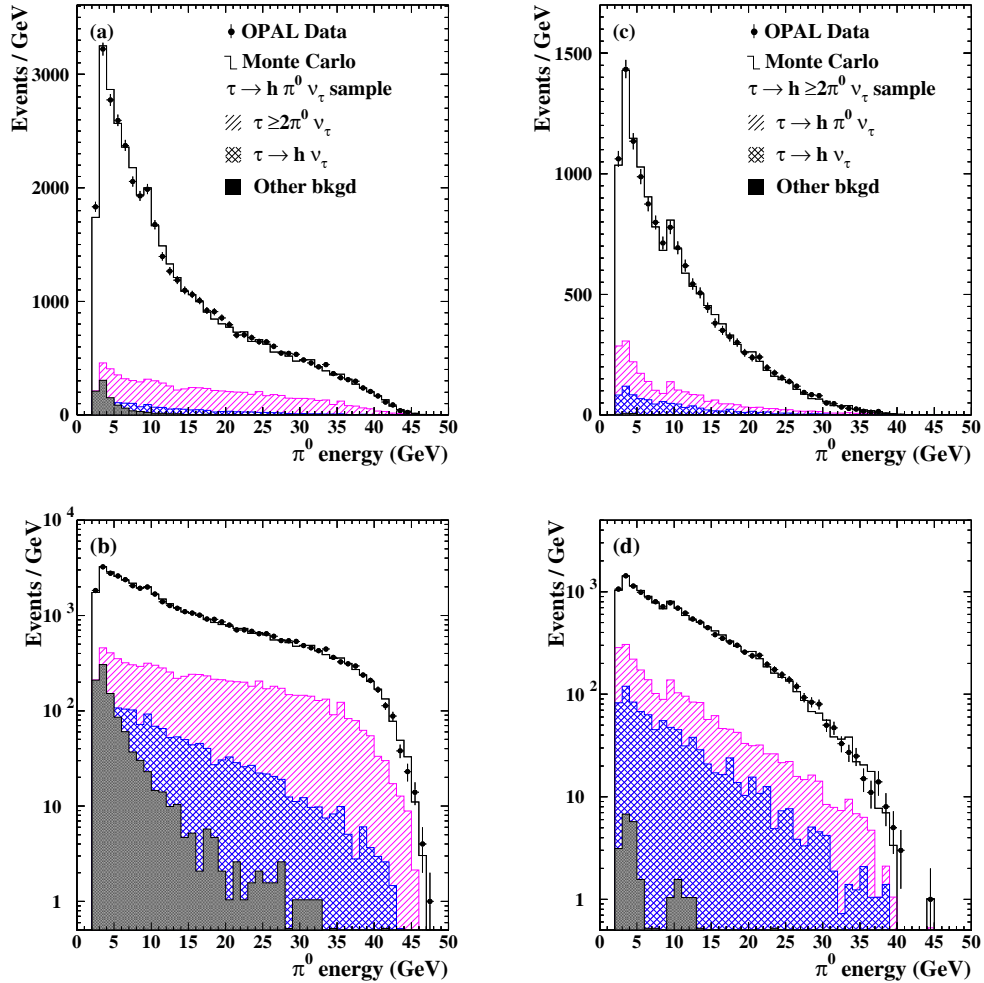


Figure 6.9: The energy distribution of reconstructed  $\pi^0$ 's shown in both linear and logarithmic scales. (a) and (b) show the energy of  $\pi^0$ 's in  $\tau^- \rightarrow h^- \pi^0 \nu_\tau$  jets. (c) and (d) show the energy of  $\pi^0$ 's in  $\tau^- \rightarrow h^- \geq 2\pi^0 \nu_\tau$  jets. The structure observed at 9.0 GeV corresponds to the one-cluster  $\pi^0$  threshold, an artifact of the  $\pi^0$  identification algorithm.

# Chapter 7

## Background rejection

This chapter deals with background decays present in the  $\tau^- \rightarrow h^- \nu_\tau$ ,  $\tau^- \rightarrow h^- \pi^0 \nu_\tau$  and  $\tau^- \rightarrow h^- \geq 2\pi^0 \nu_\tau$  samples. The first section describes the requirements placed on each sample to reduce the level of the  $\tau$  and non- $\tau$  backgrounds. In the second section, the methods used to measure the remaining  $\tau$  backgrounds in each sample are presented. The third section gives the results of the background measurements.

### 7.1 $\tau$ background rejection

The type of backgrounds present in each sample are dependent on the sample itself. These backgrounds can be from  $\tau$  decays or non- $\tau$  decays (described in section 4.2) that have survived to this stage of the analysis. Therefore requirements are placed on each sample separately to target the specific backgrounds.

In particular, the  $\tau^- \rightarrow h^- \nu_\tau$  sample has contamination from  $\tau^- \rightarrow e^- \bar{\nu}_e \nu_\tau$  and  $\tau^- \rightarrow \mu^- \bar{\nu}_\mu \nu_\tau$  decays. This contamination is reduced by requiring

$$E/p < 0.75,$$

$$p/E_{\text{beam}} > 0.05,$$

$$N^{\text{MB}} = 0,$$

where  $E_{\text{beam}}$  is the energy of the LEP beam and  $N^{\text{MB}}$  is the number of layers hit in a good region (see Appendix A) of the muon barrel detector. Figure 7.1 shows the  $E/p$  distribution for  $\tau^- \rightarrow h^- \nu_\tau$  selected one-prong jets with all other requirements applied. In addition, backgrounds from  $e^+e^- \rightarrow e^+e^-$  and  $e^+e^- \rightarrow \mu^+\mu^-$  events in

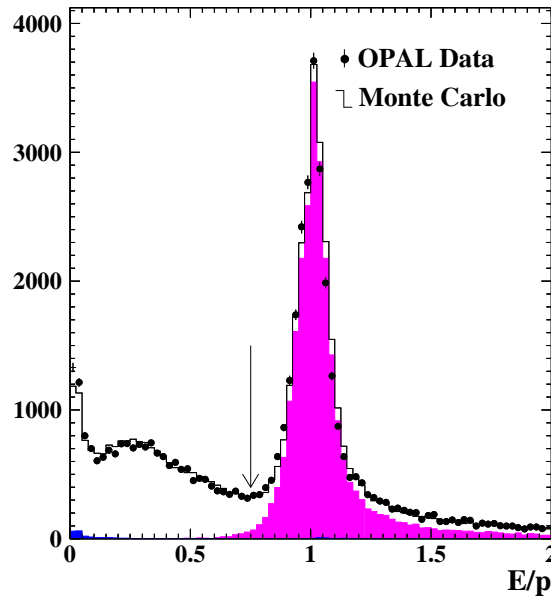


Figure 7.1: The  $E/p$  distribution for jets selected to have zero  $\pi^0$  candidates. All other background requirements have been applied. The lightly shaded area corresponds to the  $\tau^- \rightarrow e^- \bar{\nu}_e \nu_\tau$  background decays and the dark shaded area near the origin shows the  $\tau^- \rightarrow \mu^- \bar{\nu}_\mu \nu_\tau$  background decays. The  $E/p < 0.75$  requirement is indicated.

the  $\tau^- \rightarrow h^- \nu_\tau$  sample are rejected. These events are rejected by considering the acoplanarity angle<sup>1</sup> between the two jets in an event where the primary track in each jet has  $p > 30$  GeV, shown in figure 7.2. In figure 7.2 an excess of jets in the data can

---

<sup>1</sup>The acoplanarity angle is defined to be the supplement of the angle between the two jets in the transverse plane of the event.

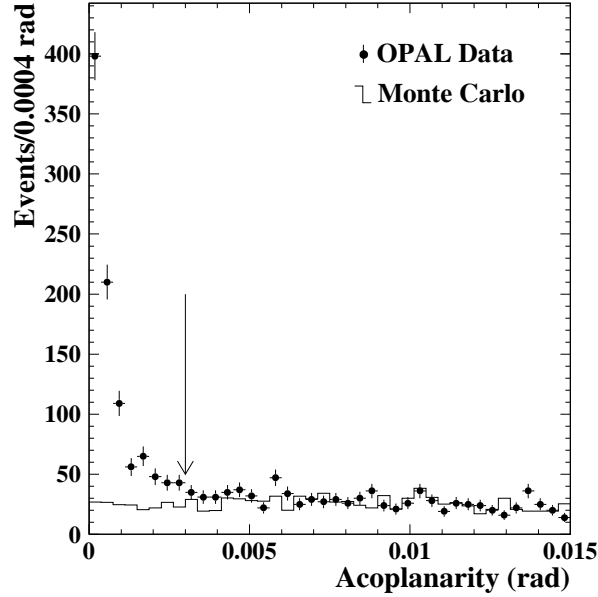


Figure 7.2: The acoplanarity distribution for  $\tau^- \rightarrow h^- \nu_\tau$  selected jets in events where the primary track in each jet has  $p > 30$  GeV. The acoplanarity requirement of 0.003 radians is indicated.

be clearly seen at acoplanarity values less than 0.003 radians. Events that meet the momentum requirements above and where the acoplanarity angle between the two jets in the event is less than 0.003 radians are removed.

In the  $\tau^- \rightarrow h^- \pi^0 \nu_\tau$  and  $\tau^- \rightarrow h^- \geq 2\pi^0 \nu_\tau$  samples the main backgrounds are due to misidentification of other signal channels. In the  $\tau^- \rightarrow h^- \pi^0 \nu_\tau$  and the  $\tau^- \rightarrow h^- \geq 2\pi^0 \nu_\tau$  samples, the background is reduced by requiring the invariant jet mass to be less than 2.0 GeV. In the  $\tau^- \rightarrow h^- \pi^0 \nu_\tau$  sample, the invariant jet mass is also required to be greater than 0.4 GeV. The invariant mass distributions of the  $\tau^- \rightarrow h^- \pi^0 \nu_\tau$  and  $\tau^- \rightarrow h^- \geq 2\pi^0 \nu_\tau$  samples are shown in figure 7.3.

A number of  $\tau^- \rightarrow h^- \pi^0 \nu_\tau$  decays are mistakenly selected into the  $\tau^- \rightarrow h^- \geq 2\pi^0 \nu_\tau$  sample. The total energy of the  $\pi^0$ 's from the  $\tau^- \rightarrow h^- \pi^0 \nu_\tau$  decays is relatively



low and this contamination is reduced by requiring

$$\frac{E_{\pi^0}^{\text{total}}}{p} > 0.8,$$

where  $E_{\pi^0}^{\text{total}}$  is the energy sum of all  $\pi^0$ 's identified in the jet and  $p$  is the momentum of the primary track.

## 7.2 Estimation of $\tau$ backgrounds

The backgrounds from  $\tau^- \rightarrow e^- \bar{\nu}_e \nu_\tau$  and  $\tau^- \rightarrow \mu^- \bar{\nu}_\mu \nu_\tau$  decays in each sample are measured using distributions previously unused in the selection process. A region in each distribution that is dominated by the background is used to make the measurement. The data and Monte Carlo distributions in the background-dominated region are compared and any deviations between the two are assumed to be caused by the background in question. If the ratio of data to Monte Carlo in the background region is different from unity then the number of background jets is rescaled by this ratio in the background calculation. The error of this correction factor is the combined statistical errors of the data and Monte Carlo. The uncertainties on the correction factors are included in the background errors (including the case where the correction factor is unity).

The  $\tau^- \rightarrow e^- \bar{\nu}_e \nu_\tau$  background is estimated using the energy loss ( $dE/dx$ ) in the jet drift chamber. Figure 7.4 shows the  $dE/dx$  distribution in the data and Monte Carlo for jets selected with one  $\pi^0$  and  $p < 5$  GeV. The ratios of data to Monte Carlo  $\tau^- \rightarrow e^- \bar{\nu}_e \nu_\tau$  background jets are calculated using jets that have  $9.25 < dE/dx < 12.0$  keV/cm. The ratio obtained in each sample is used as a correction factor and is shown in Table 7.1. Appendix B.1 gives a more detailed description of this method.

The  $\tau^- \rightarrow \mu^- \bar{\nu}_\mu \nu_\tau$  background in the  $\tau^- \rightarrow h^- \nu_\tau$  sample is measured by creating

Selection	Background	
	$\tau^- \rightarrow e^- \bar{\nu}_e \nu_\tau$	$\tau^- \rightarrow \mu^- \bar{\nu}_\mu \nu_\tau$
$\tau^- \rightarrow h^- \nu_\tau$	$1.30 \pm 0.18$	$1.39 \pm 0.26$
$\tau^- \rightarrow h^- \pi^0 \nu_\tau$	$1.04 \pm 0.06$	$0.91 \pm 0.28$
$\tau^- \rightarrow h^- \geq 2\pi^0 \nu_\tau$	$0.80 \pm 0.28$	

Table 7.1: Correction factors used to scale the  $\tau^- \rightarrow e^- \bar{\nu}_e \nu_\tau$  and  $\tau^- \rightarrow \mu^- \bar{\nu}_\mu \nu_\tau$  backgrounds.

a sample of  $\tau^- \rightarrow \mu^- \bar{\nu}_\mu \nu_\tau$  jets in both data and Monte Carlo. The efficiency of the muon chamber requirements to reject  $\tau^- \rightarrow \mu^- \bar{\nu}_\mu \nu_\tau$  is measured using these samples and the ratio of the efficiencies is used as the Monte Carlo scaling factor for  $\tau^- \rightarrow \mu^- \bar{\nu}_\mu \nu_\tau$  background in the  $\tau^- \rightarrow h^- \nu_\tau$  sample. The  $\tau^- \rightarrow \mu^- \bar{\nu}_\mu \nu_\tau$  contamination in the  $\tau^- \rightarrow h^- \pi^0 \nu_\tau$  sample is measured by identifying tracks with hits in the muon chambers, since the muon chambers were not used in this selection. The ratio of data to Monte Carlo is used as the scaling factor for  $\tau^- \rightarrow \mu^- \bar{\nu}_\mu \nu_\tau$  background in the  $\tau^- \rightarrow h^- \pi^0 \nu_\tau$  sample. Appendix B.2 gives a more detailed description of these correction factors.

### 7.3 Background results

Table 7.2 shows the estimated backgrounds in each selection. In addition to the  $\tau^- \rightarrow e^- \bar{\nu}_e \nu_\tau$  and  $\tau^- \rightarrow \mu^- \bar{\nu}_\mu \nu_\tau$  decays, there is background from  $\tau^- \rightarrow h^- K^0 X \nu_\tau$  decays where X is any number of neutral particles in the final state. There is also background from other tau decays, labelled as ‘‘Other background’’ in Table 7.2, which are mainly tau decays to  $\eta$  (27%) and  $\omega$  modes (60%), with lesser contributions coming from decays with three charged hadrons in the final state (13%). Both the  $\tau^- \rightarrow h^- K^0 X \nu_\tau$  and other tau decays are measured from Monte Carlo information.

Background	Selections		
	$\tau^- \rightarrow h^- \nu_\tau$	$\tau^- \rightarrow h^- \pi^0 \nu_\tau$	$\tau^- \rightarrow h^- \geq 2\pi^0 \nu_\tau$
$\tau^- \rightarrow e^- \bar{\nu}_e \nu_\tau$	$1.43 \pm 0.20\%$	$1.59 \pm 0.11\%$	$1.67 \pm 0.59\%$
$\tau^- \rightarrow \mu^- \bar{\nu}_\mu \nu_\tau$	$1.57 \pm 0.29\%$	$0.68 \pm 0.21\%$	$0.02 \pm 0.04\%$
$\tau^- \rightarrow h^- K^0 X \nu_\tau$	$1.80 \pm 0.14\%$	$1.57 \pm 0.11\%$	$1.81 \pm 0.15\%$
Other background	$0.07 \pm 0.02\%$	$0.53 \pm 0.03\%$	$3.32 \pm 0.24\%$
Total	$4.88 \pm 0.38\%$	$4.37 \pm 0.26\%$	$6.82 \pm 0.65\%$

Table 7.2: The corrected backgrounds as a percentage of each selection.

The errors are calculated from the uncertainties in the efficiency matrix and the background branching ratio from the PDG [2]. The background uncertainties in each selection, shown in Table 7.2, are used in calculating the systematic errors. An additional modelling uncertainty, described in Section 8.3, is added to the  $\tau^- \rightarrow h^- K^0 X \nu_\tau$  decays.

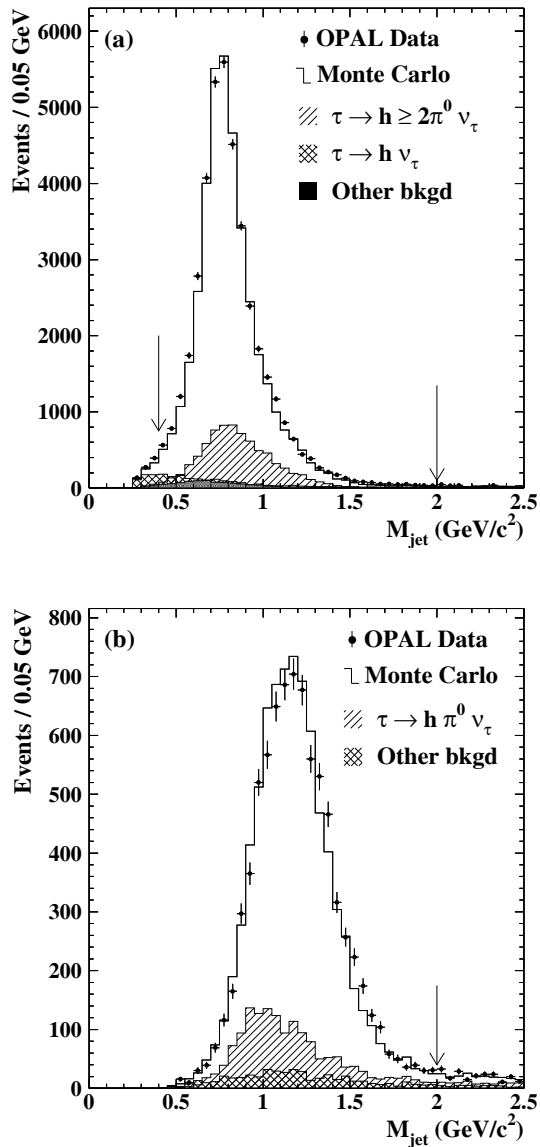


Figure 7.3: The invariant mass distribution of jets identified as  $\tau^- \rightarrow h^- \pi^0 \nu_\tau$  (a) and  $\tau^- \rightarrow h^- \geq 2\pi^0 \nu_\tau$  (b). The mass cuts are indicated on the plots. In figure (a) the diagonally hatched area is  $\tau^- \rightarrow h^- \geq 2\pi^0 \nu_\tau$  jets, the cross hatched area is  $\tau^- \rightarrow h^- \nu_\tau$  jets and the dark shaded area is other background. In figure (b) the diagonally hatched area is  $\tau^- \rightarrow h^- \pi^0 \nu_\tau$  jets and the cross hatched area is other background.

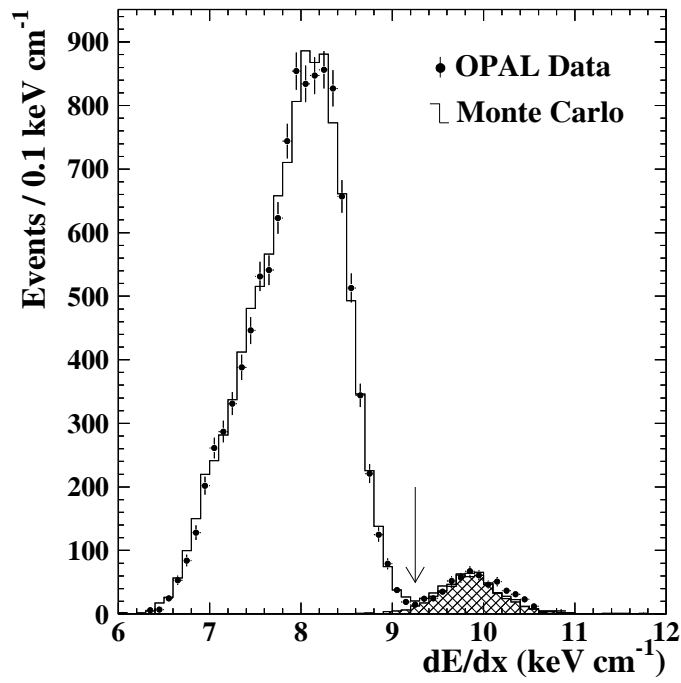


Figure 7.4: The  $dE/dx$  distribution used to measure the  $\tau^- \rightarrow e^- \bar{\nu}_e \nu_\tau$  background in the  $\tau^- \rightarrow h^- \pi^0 \nu_\tau$  sample. A background-dominated region is created by selecting jets with  $9.25 < dE/dx < 12.0$  keV/cm (indicated on the histogram). The cross hatched region corresponds to the  $\tau^- \rightarrow e^- \bar{\nu}_e \nu_\tau$  background events.

# Chapter 8

## Results

This chapter describes the calculation of the  $\tau^- \rightarrow h^- \nu_\tau$ ,  $\tau^- \rightarrow h^- \pi^0 \nu_\tau$  and  $\tau^- \rightarrow h^- \geq 2\pi^0 \nu_\tau$  branching ratios. The first section outlines the method of calculating the branching ratios. The second section combines results from previous sections and gives the branching ratio results. The last section describes the sources of the systematic errors on the branching ratios and the results of the systematic error calculations.

### 8.1 Branching ratio calculations

#### 8.1.1 Branching ratio for a single decay channel

The branching ratio of the  $\tau$  lepton to a final state  $x$  (eg.  $\tau^- \rightarrow X \nu_\tau$  decay) is defined as

$$B_X \equiv \frac{N_X}{N_\tau} \quad (8.1)$$

where  $N_X$  is the number of  $\tau^- \rightarrow X \nu_\tau$  decays in a sample containing  $N_\tau$  taus. In practice, the sample of tau decays will contain background from other events. Thus the true number of  $\tau$ 's in the sample ( $N_\tau$ ) is given by

$$N_\tau = (1 - f^{non-\tau}) N_\tau^{\text{sel}} \quad (8.2)$$

where  $f^{non-\tau}$  is the fraction of background events present in a sample of  $N_\tau^{\text{sel}}$  taus. In addition, the efficiency for selecting  $\tau^- \rightarrow X \nu_\tau$  decays must be considered. The efficiency to detect  $\tau^- \rightarrow X \nu_\tau$  decays is given by

$$\epsilon = \frac{N_X^{\text{sel}}}{N_X} \quad (8.3)$$

where  $N_X$  is the total number of  $\tau^- \rightarrow X \nu_\tau$  decays and  $N_X^{\text{sel}}$  is the number of selected  $\tau^- \rightarrow X \nu_\tau$  decays. Consequently equation 8.1 can be rewritten as

$$B_X = \frac{N_X^{\text{sel}}}{N_\tau^{\text{sel}}(1 - f^{non-\tau})\epsilon} \quad (8.4)$$

and the branching ratio can be calculated from observed quantities.

### 8.1.2 Branching ratio for multiple decay channels

In this work three selections are applied to identify the  $0\pi^0$ ,  $1\pi^0$  and  $\geq 2\pi^0$  decays, which we refer to as the “signal” channels. The  $0\pi^0$  selection does not exclusively select  $\tau^- \rightarrow h^- \nu_\tau$  decays because  $\tau^- \rightarrow h^- \pi^0 \nu_\tau$  and  $\tau^- \rightarrow h^- \geq 2\pi^0 \nu_\tau$  decays as well as other tau decays (“background” channels) appear in the  $0\pi^0$  sample. Hence the number of events selected by the  $0\pi^0$  selection is given as

$$N^{\text{sel}} = \sum_s N_s^{\text{sel}} + \sum_b N_b^{\text{sel}}$$

or alternately, with the aid of equation 8.3, as

$$N^{\text{sel}} = \sum_s \epsilon_s N_s + \sum_b \epsilon_b N_b \quad (8.5)$$

where  $s$  is the index over all signal channels,  $b$  is the index over all background channels,  $N_s$  ( $N_b$ ) is the number of signal (background) events and  $\epsilon_s$  ( $\epsilon_b$ ) is the efficiency to detect signal (background) decays. Dividing equation 8.5 by  $N_\tau$  and

substituting equations 8.1 and 8.2 gives

$$\frac{N^{\text{sel}}}{(1 - f^{\text{non-}\tau}) N_{\tau}^{\text{sel}}} = \sum_s \epsilon_s B_s + \sum_b \epsilon_b B_b \quad (8.6)$$

where  $B_s$  and  $B_b$  are the branching ratios of the signal and background decays.

Now the formalism can be extended to the three selections,  $\tau^- \rightarrow h^- \nu_{\tau}$ ,  $\tau^- \rightarrow h^- \pi^0 \nu_{\tau}$  and  $\tau^- \rightarrow h^- \geq 2\pi^0 \nu_{\tau}$  by adding an index  $i$  to equation 8.6,

$$\epsilon_{i1} B_1 + \epsilon_{i2} B_2 + \epsilon_{i3} B_3 + \sum_{k=4}^M \epsilon_{ik} B_k \mathcal{F}_k = \frac{N_i^{\text{sel}}}{N_{\tau}^{\text{sel}} (1 - f^{\text{non-}\tau})} \quad (8.7)$$

where  $\epsilon_{ij}$  ( $j = 1, 2, 3$ ) are the efficiencies for selecting signal  $j$  using selection  $i$  and  $\epsilon_{ik}$  ( $k = 4, \dots, M$ ) are the efficiencies for selecting the  $\tau$  background modes using selection  $i$ .  $B_j$  ( $j = 1, 2, 3$ ) corresponds to the branching ratios of the  $\tau^- \rightarrow h^- \nu_{\tau}$ ,  $\tau^- \rightarrow h^- \pi^0 \nu_{\tau}$  and  $\tau^- \rightarrow h^- \geq 2\pi^0 \nu_{\tau}$  channels respectively and  $B_k$  ( $k = 4, \dots, M$ ) are the branching ratios of the backgrounds. The  $\mathcal{F}_k$  factors are the background correction factors that are described in section 7.2 and shown in Table 7.1.  $N_i^{\text{sel}}$  is the number of data events that pass the selection  $i$ . The  $\tau$  background branching ratios are taken from the PDG [2] and  $f^{\text{non-}\tau}$  is given in Table 4.6.

The selection efficiencies ( $\epsilon_{ij}$ ) for both signal and background are determined directly from Monte Carlo and are given in Table 8.1. The efficiency for detecting decay channel  $j$  in selection  $i$  is defined as

$$\epsilon_{ij} \equiv \frac{N_{ij}}{N_j} \quad (8.8)$$

and the uncertainty on the efficiency is given by the binomial error as

$$\sigma_{\epsilon_{ij}} = \sqrt{\frac{\epsilon_{ij}(1 - \epsilon_{ij})}{N_j}} \quad (8.9)$$

where  $N_{ij}$  is the number of  $j$  decays identified by selection  $i$  and  $N_j$  is the total number of  $j$  decays.



Selection	Selection efficiency from MC		
	$\tau^- \rightarrow h^- \nu_\tau$	$\tau^- \rightarrow h^- \pi^0 \nu_\tau$	$\tau^- \rightarrow h^- \geq 2\pi^0 \nu_\tau$
$0\pi^0$	$0.5502 \pm 0.0024$	$0.1003 \pm 0.0010$	$0.0249 \pm 0.0008$
$1\pi^0$	$0.0455 \pm 0.0010$	$0.5985 \pm 0.0016$	$0.4273 \pm 0.0025$
$\geq 2\pi^0$	$0.0005 \pm 0.0001$	$0.0237 \pm 0.0005$	$0.2730 \pm 0.0023$

Selection	Number selected ( $N_i^{\text{sel}}$ )	Fraction selected ( $n_i$ )
$\tau^- \rightarrow h^- \nu_\tau$	18547	0.0938
$\tau^- \rightarrow h^- \pi^0 \nu_\tau$	40537	0.2061
$\tau^- \rightarrow h^- \geq 2\pi^0 \nu_\tau$	6802	0.0336

Channel	Branching Ratio (%)
$\tau^- \rightarrow h^- \nu_\tau$	$11.98 \pm 0.13 \pm 0.16$
$\tau^- \rightarrow h^- \pi^0 \nu_\tau$	$25.89 \pm 0.17 \pm 0.29$
$\tau^- \rightarrow h^- \geq 2\pi^0 \nu_\tau$	$9.91 \pm 0.31 \pm 0.27$

Sample	$\tau^- \rightarrow h^- \pi^0 \nu_\tau$	$\tau^- \rightarrow h^- \geq 2\pi^0 \nu_\tau$
$\tau^- \rightarrow h^- \nu_\tau$	-0.430	0.167
$\tau^- \rightarrow h^- \pi^0 \nu_\tau$		-0.470

Table 8.1: Summary of results. The first table shows the efficiencies for identifying the signals for each selection. The second table shows the number of jets and background-subtracted fractions for each data selection. The branching ratio results are given in the third table and the fourth gives the statistical correlations between the branching ratios.

Equation 8.7 can be written in matrix form as

$$[\epsilon][B] = [n]. \quad (8.10)$$

where  $[\epsilon]$  is a  $3 \times 3$  dimensional matrix of all signal efficiencies,  $[B]$  is a  $3 \times 1$  dimensional matrix of the signal branching ratios and  $[n]$  is a  $3 \times 1$  dimensional matrix with entries

$$n_i = \frac{N_i^{\text{sel}}}{N_\tau^{\text{sel}}(1 - f^{\text{non-}\tau})} - \sum_{k=4}^M \epsilon_{ik} B_k \mathcal{F}_k \quad (8.11)$$

containing the fraction of events in each selection after the background is subtracted.

If  $[\epsilon]$  is an invertible matrix, then the branching ratios,  $[B]$ , can be solved as

$$[B] = [\epsilon]^{-1}[n] \quad (8.12)$$

where  $[\epsilon]^{-1}$  is the inverse of the efficiency matrix.

The solution of equation 8.12 gives the branching ratios in the  $\tau$  pair selected sample. However, the  $\tau$  pair selection does not select all decay modes equally and introduces relative biases between the  $\tau$  decays. These biases are studied using the Monte Carlo sample and are calculated as *bias factors*. These bias factors are used to correct the biases in the branching ratios from the  $\tau$  pair selected sample by

$$B_i^{\text{true}} = \frac{B_i^{\text{sel}}}{F^{\text{bias}}}.$$

where  $B_i^{\text{sel}}$  is the branching ratio from the  $\tau$  pair selected sample,  $B_i^{\text{true}}$  is the unbiased corrected branching ratio and  $F^{\text{bias}}$  is the bias factor for decay channel  $i$ . The bias factors are  $0.989 \pm 0.002$ ,  $1.019 \pm 0.001$  and  $1.013 \pm 0.002$  for the  $\tau^- \rightarrow h^- \nu_\tau$ ,  $\tau^- \rightarrow h^- \pi^0 \nu_\tau$  and  $\tau^- \rightarrow h^- \geq 2\pi^0 \nu_\tau$  decays, respectively. A more thorough description of the bias factors is given in Appendix C.

The statistical uncertainty on equation 8.12 can be calculated explicitly. Branching ratio  $i$  from equation 8.12 is written explicitly as

$$B_i = \sum_{j=1}^3 \epsilon_{ij}^{-1} \left( \frac{N_j^{\text{sel}}}{N_\tau^{\text{sel}}(1 - f_{\text{non-}\tau})} - \sum_{k=4}^M \epsilon_{jk} B_k \mathcal{F}_k \right). \quad (8.13)$$

The statistical uncertainty on  $B_i$ , that comes from the uncertainty on the first term inside the parentheses in equation 8.13, is calculated to be

$$\sigma_{B_i}^2(\text{stat}) = \frac{1}{(1 - f_{\text{non-}\tau})^2} \sum_{j=1}^3 (\epsilon_{ij}^{-1} \sigma_j^{\text{stat}})^2 \quad (8.14)$$

where

$$\sigma_j^{\text{stat}} = \sqrt{\frac{f_j^{\text{sel}}(1 - f_j^{\text{sel}})}{N_\tau^{\text{sel}}}} \quad (8.15)$$

and  $f_j^{\text{sel}} \equiv N_j^{\text{sel}}/N_\tau^{\text{sel}}$ .

## 8.2 Results

The  $\tau$  pair selection identifies 190728  $\tau$  candidates ( $N_\tau^{\text{sel}}$ ). The number of data events ( $N_i^{\text{sel}}$ ) is found to be 18547, 40537 and 6802 for the  $\tau^- \rightarrow h^- \nu_\tau$ ,  $\tau^- \rightarrow h^- \pi^0 \nu_\tau$  and  $\tau^- \rightarrow h^- \geq 2\pi^0 \nu_\tau$  selections respectively. The fraction of data events ( $n_i$ ), after background subtraction is shown in Table 8.1.

The branching ratios for  $\tau^- \rightarrow h^- \nu_\tau$ ,  $\tau^- \rightarrow h^- \pi^0 \nu_\tau$ , and  $\tau^- \rightarrow h^- \geq 2\pi^0 \nu_\tau$  are calculated using equation 8.7 and are shown in Table 8.1. The statistical error is calculated using equation 8.14, while the systematic error is discussed in section 8.3. The measurements of these branching ratios are correlated. The correlation coefficients between branching ratios calculated using the statistical errors on each branching ratio are given in Table 8.1 and discussed in more detail in Appendix D.

	Systematic error for each selection (%)		
	$\tau^- \rightarrow h^- \nu_\tau$	$\tau^- \rightarrow h^- \pi^0 \nu_\tau$	$\tau^- \rightarrow h^- \geq 2\pi^0 \nu_\tau$
MC statistics	0.11	0.17	0.14
Signal BR uncertainty	0.01	0.05	0.03
Bias factors	0.02	0.03	0.02
Unmodelled channels	0.00	0.02	0.04
Non- $\tau$ backgrounds	0.02	0.04	0.01
$\tau^- \rightarrow e^- \bar{\nu}_e \nu_\tau$	0.04	0.07	0.08
$\tau^- \rightarrow \mu^- \bar{\nu}_\mu \nu_\tau$	0.05	0.08	0.01
$\tau^- \rightarrow h^- K^0 X \nu_\tau$	0.06	0.07	0.04
Other backgrounds	0.00	0.03	0.03
$a_1$ modelling	0.01	0.13	0.15
1-cluster $\pi^0$ threshold	0.03	0.02	0.03
2-cluster $\pi^0$ threshold	0.03	0.11	0.11
Anode plane cut	0.00	0.05	0.03
Photon conversions	0.06	0.03	0.02
Energy smearing	0.01	0.01	0.03
Radiative clusters	0.03	0.00	0.00
Energy scale	0.03	0.03	0.04
Total	0.16	0.29	0.27

Table 8.2: Systematic errors.

### 8.3 Systematic errors

The systematic errors on the branching ratios are shown in Table 8.2. There are two types of systematic errors. The first type, although considered a systematic error, are statistical in nature as they are derived from the Monte Carlo sample. The second type of systematic error include uncertainties associated with the modelling of the physical processes (such as the decay of the  $a_1$  resonance) or the modelling of the detectors response (such as photon conversions). We briefly describe the individual contributions to the systematic errors.

### 8.3.1 Monte Carlo systematic errors

The first section of Table 8.2 gives the errors due to Monte Carlo statistics, signal branching ratio uncertainties, bias factors and unmodelled signal channels. The error on the branching ratios due to the Monte Carlo statistical error is directly calculated from the uncertainties on the elements of inverse efficiency matrix (see Appendix E).

The systematic error on  $B_i$  is found from equation 8.13 and given by

$$\sum_{j=1}^3 (\sigma_{\epsilon_{ij}^{-1}} n_j)^2. \quad (8.16)$$

There is a covariance matrix for each element of the inverse efficiency matrix made up of contributions from all the statistical errors in the efficiency matrix. A conservative Monte Carlo statistical uncertainty is quoted here that uses essentially the “diagonal” error for each inverse matrix element. If the full covariance matrices for each element of the inverse efficiency matrix are used then the Monte Carlo statistical errors are slightly reduced.

The selection efficiencies depend on the relative branching ratios of the individual decay modes. The efficiency for detecting  $\tau^- \rightarrow h^- \nu_\tau$  is an average of the efficiencies for selecting  $\tau^- \rightarrow \pi^- \nu_\tau$  and  $\tau^- \rightarrow K^- \nu_\tau$  weighted by their relative branching ratios. Similarly, the efficiency for detecting  $\tau^- \rightarrow h^- \pi^0 \nu_\tau$  is an average of the efficiencies for selecting  $\tau^- \rightarrow \pi^- \pi^0 \nu_\tau$  and  $\tau^- \rightarrow K^- \pi^0 \nu_\tau$  weighted by their relative branching ratios. The same method is used for the  $\tau^- \rightarrow h^- \geq 2\pi^0 \nu_\tau$  efficiency where the decay modes are listed in Table 5.1. The signal branching ratios were calculated using the PDG branching ratios and uncertainties [2]. The dependence of the efficiency and the decay branching ratios on the signal branching ratios was evaluated and included as a systematic uncertainty.

A small correction must be applied to the branching ratios to correct the slight

bias introduced by the  $\tau$  pair selection criteria as discussed in Appendix C. The dependence of the bias factor on the  $\tau$  pair selection and on the branching ratios of each channel is found to be relatively small. In addition, other Monte Carlo samples using a different electromagnetic shower model give similar results. The systematic error on each branching ratio is calculated directly using the bias factor error.

The second section of Table 8.2 gives the errors due to the non- $\tau$  and  $\tau$  backgrounds. The systematic errors on the branching ratios due to non- $\tau$  and  $\tau$  backgrounds are calculated from the uncertainties given in Tables 4.6 and 7.2, respectively. The  $\tau$  background uncertainty is calculated from equation 8.13 as

$$\sigma_{B_i}^2(\tau - \text{bkgrd}) = \sum_{k=4}^M [(\sigma_{\epsilon_{ik}} B_k \mathcal{F}_k)^2 + (\epsilon_{ik} \sigma_{B_k} \mathcal{F}_k)^2 + (\epsilon_{ik} B_k \sigma_{\mathcal{F}_k})^2] \quad (8.17)$$

where  $\sigma_{\epsilon_{ik}}$ ,  $\sigma_{B_k}$  and  $\sigma_{\mathcal{F}_k}$  is the uncertainty on each background efficiency, background branching ratio and background correction factor respectively.

### 8.3.2 Instrumental systematic errors

The instrumental systematic errors are given in the third section of Table 8.2. The Monte Carlo used in this analysis did not include some decay modes defined as signals by the PDG [2]. Table 5.1 shows these decay modes. The systematic effect of the  $\tau^- \rightarrow h^- 4\pi^0 \nu_\tau$  mode on the  $\tau^- \rightarrow h^- \pi^0 \nu_\tau$  and  $\tau^- \rightarrow h^- \geq 2\pi^0 \nu_\tau$  samples is calculated using the PDG branching ratio and the assumption that the efficiency for  $\tau^- \rightarrow h^- 4\pi^0 \nu_\tau$  is the same as that for  $\tau^- \rightarrow h^- 3\pi^0 \nu_\tau$ . The uncertainty for each of these modes is assumed to be 50% of their respective branching ratios. The total systematic error is calculated from these uncertainties.

The  $a_1 \rightarrow \pi^- 2\pi^0$  decay was simulated using the IMR model, as described in reference [49]. The IMR model gives a better description of the isospin analogue state

$a_1^- \rightarrow \pi^- \pi^+ \pi^-$  data primarily because of the inclusion of the polynomial background term [48]. The uncertainty in the contribution of the polynomial background was measured in [49] to be approximately 17%. The systematic error in the branching ratios due to the uncertainty in the  $a_1$  model is conservatively estimated by varying the normalization of the polynomial background by  $\pm 50\%$  ( $3\sigma$ ).

The Monte Carlo models the hadronic showering in  $\tau$  decays reasonably well. The thresholds for the neutral clusters, one-cluster and two-cluster  $\pi^0$ 's, as well as other requirements, have been carefully studied (see Appendix F) to avoid any poorly modelled regions due to low energy hadronic clusters. However, as the energy thresholds are lowered, deviations between the data and Monte Carlo appear since clusters close to the track from hadronic interactions are accepted into the  $\pi^0$ -finding algorithm. The lower energy thresholds of both the one and two cluster  $\pi^0$  cases are varied to estimate the systematic error due to the Monte Carlo modelling of energy deposition in the electromagnetic calorimeter. The lower energy threshold of the one-cluster  $\pi^0$  case is varied from 2.0 to 3.0 GeV and the energy threshold of the two-cluster  $\pi^0$  case is varied from 2.6 to 4.0 GeV. The maximum variation from each nominal branching ratio is taken as the systematic error in each case.

The effect of tracks passing close to the anode plane of the OPAL jet chamber is considered as a source of systematic error, shown in Appendix G. The Monte Carlo does not perfectly model the position of tracks close to the anode plane. The branching ratios were recalculated by removing tracks within  $0.25^\circ$  of the anode plane. The resulting change in the branching ratios is taken as the systematic error.

Approximately 5% of the identified  $\pi^0$ 's are composed of a neutral cluster and a photon conversion. Although the Monte Carlo does a reasonable job of modelling conversions, there are minor discrepancies between data and Monte Carlo. The ra-

tio of data to Monte Carlo jets with an identified conversion pair is found to be  $0.985 \pm 0.013$ . The branching ratios are calculated with Monte Carlo jets containing a conversion weighted to simulate a  $\pm 3\sigma$  ( $\pm 4\%$ ) change in conversion identification efficiency. The maximum variation from each nominal branching ratio is taken as the systematic error. The sensitivity of the results to photon conversions is also checked by rejecting jets with an identified photon conversion and recalculating the branching ratios. The maximum variation in each branching ratio was taken as the systematic error.

The energy of each electromagnetic calorimeter cluster in the Monte Carlo is smeared as discussed in section 6.3.2. The uncertainty due to this smearing is assessed by varying the amount of smearing applied by  $\pm 20\%$ . The change in the branching ratios is taken as the systematic error.

Clusters were considered to be due to radiative photons if the mass of the track and cluster was greater than 3 GeV (see section 6.4). These clusters are ignored by the  $\pi^0$ -algorithm by default. This requirement was removed and the change in the branching ratios was taken as the systematic error.

The energy scale uncertainty reflects the uncertainty in the electromagnetic calorimeter calibration between Monte Carlo and data. To determine the systematic uncertainty the clusters are rescaled by  $\pm 0.2\%$  and the largest effect on the branching ratios is taken as the systematic uncertainty.

The systematic errors are added in quadrature and the total is given in Table 8.2.



# Chapter 9

## Discussion

The  $\tau^- \rightarrow h^- \nu_\tau$  branching ratio is measured to be  $(11.98 \pm 0.13 \pm 0.16)\%$  and is compared with other published results and the re-evaluated world average in figure 9.1. The world average branching ratio ( $B_{\text{WA}}$ ) is a weighted average of the experimental results and is given by

$$B_{\text{WA}} = \frac{\sum B_{\text{exp}}/\sigma_{\text{exp}}^2}{\sum 1/\sigma_{\text{exp}}^2}$$

where  $B_{\text{exp}}$  are the experimental results and  $\sigma_{\text{exp}}$  is the error on each experimental result. The  $\tau^- \rightarrow h^- \nu_\tau$  branching ratio agrees well with the PDG average of  $(11.95 \pm 0.14)\%$ <sup>1</sup> [2] but is slightly above the recent CLEO measurement of  $(11.52 \pm 0.13)\%$  [50] and the theoretical prediction of  $(11.65 \pm 0.06)\%$  made by Decker and Finkemeier [11].

The  $\tau^- \rightarrow h^- \nu_\tau$  branching ratio and the OPAL tau lifetime [51] is used to measure the ratio of the tau to muon charged current coupling constants as described in section 2.4. The  $\pi^- \rightarrow \mu^- \bar{\nu}_\mu$  and  $K^- \rightarrow \mu^- \bar{\nu}_\mu$  branching ratios, the masses of the tau, muon and the pion, and the lifetime of the pion are taken from the PDG [2].

---

<sup>1</sup>The  $\tau^- \rightarrow h^- \nu_\tau$  branching ratio is calculated by taking the PDG average branching ratio of the  $\tau^- \rightarrow h^- \geq 0 K_L^0 \nu_\tau$  mode and subtracting the average branching ratios of the decays involving the  $K_L^0$ .

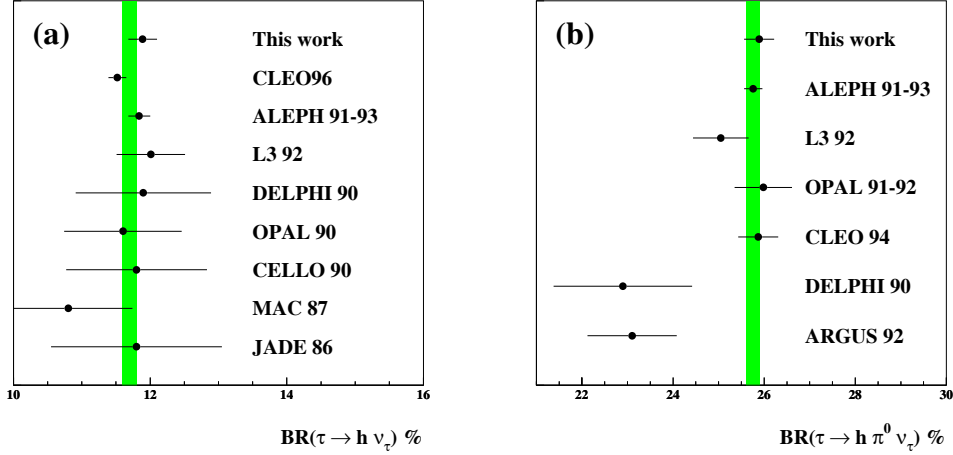


Figure 9.1: The branching ratios for the  $\tau^- \rightarrow h^- \nu_\tau$  and  $\tau^- \rightarrow h^- \pi^0 \nu_\tau$  decay modes for this work are compared with previous measurements. The solid band in each plot is the re-evaluated world average for that channel. The error bars shown include both systematic and statistical uncertainties.

The ratio  $g_\tau/g_\mu$ , using equation 2.18, is found to be

$$\frac{g_\tau}{g_\mu} = 1.018 \pm 0.010,$$

where the error on  $g_\tau/g_\mu$  is dominated by the uncertainties in the  $\tau^- \rightarrow h^- \nu_\tau$  branching ratio and the OPAL  $\tau$  lifetime [51]. In figure 9.2 the  $\tau^- \rightarrow h^- \nu_\tau$  branching ratio is plotted against the tau lifetime. The Standard Model prediction is shown as the shaded band with a width reflecting the uncertainty in  $m_\tau$ . The solid point uses the  $\tau^- \rightarrow h^- \nu_\tau$  branching ratio from this work and the OPAL tau lifetime. The open circle uses the PDG tau lifetime [2] and the re-evaluated  $\tau^- \rightarrow h^- \nu_\tau$  world average branching ratio that includes the  $\tau^- \rightarrow h^- \nu_\tau$  branching ratio result from this work, the CLEO measurement and the previous PDG world average results. These latter numbers give  $g_\tau/g_\mu = 1.003 \pm 0.005$ .

The ratio of  $g_\tau/g_\mu$  can also be measured by comparing the  $\tau^- \rightarrow e^- \bar{\nu}_e \nu_\tau$  and

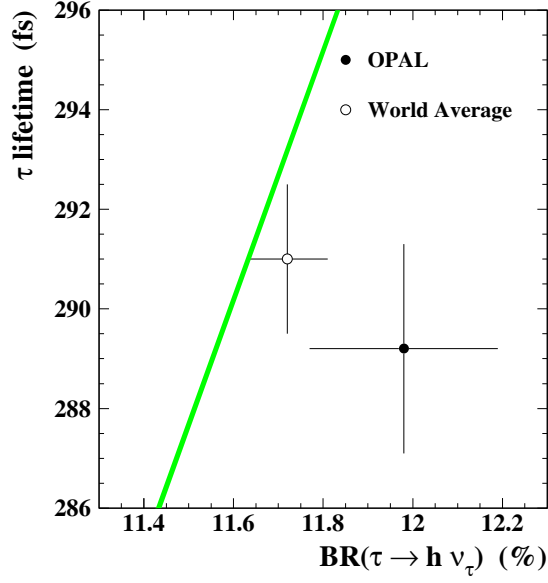


Figure 9.2: The tau lifetime is plotted as a function of  $\tau^- \rightarrow h^- \nu_\tau$  branching ratio. The shaded band shows the Standard Model prediction assuming lepton universality and its width reflects the uncertainty associated with the tau mass. The solid point uses the  $\tau^- \rightarrow h^- \nu_\tau$  branching ratio obtained in this measurement and the OPAL tau lifetime. The open circle uses the recalculated world average for the  $\tau^- \rightarrow h^- \nu_\tau$  branching ratio and the PDG tau lifetime.

$\mu \rightarrow e^- \bar{\nu}_e \nu_\mu$  decays. Using the PDG values for the  $\tau^- \rightarrow e^- \bar{\nu}_e \nu_\tau$  and  $\tau$  lifetime gives  $g_\tau/g_\mu = 1.000 \pm 0.003$ . Although this result is more precise, the two measurements are complementary. The measurement using the  $\tau^- \rightarrow \pi^- \nu_\tau$  and  $\pi^- \rightarrow \mu^- \bar{\nu}_\mu$  decays probes the couplings to a longitudinal W boson, while the measurement using the  $\tau^- \rightarrow e^- \bar{\nu}_e \nu_\tau$  and  $\mu \rightarrow e^- \bar{\nu}_e \nu_\mu$  decays probes the couplings to a transverse W.

The decay  $\tau^- \rightarrow h^- \nu_\tau$  is sensitive to the presence of supersymmetric physics beyond the Standard Model. Supersymmetry [52] introduces an underlying symmetry,  $R$ -parity<sup>2</sup> between fermions and bosons. As a result, *sparticles*, the supersymmetric

---

<sup>2</sup> $R$ -parity is defined as  $R = -1^{3B+L+2S}$  where  $B$  is the baryon number,  $L$  is lepton number and

partners to the Standard Model particles are predicted to exist. The Standard Model particles are even under  $R$ -parity and the supersymmetric sparticles are odd under  $R$ -parity. There is an extension to supersymmetry that does not conserve  $R$ -parity. In this model, the  $\tau^- \rightarrow h^- \nu_\tau$  and  $h^- \rightarrow \mu^- \bar{\nu}_\mu$  widths have an additional term due to the exchange of a down-type supersymmetric quark or *squark* ( $\tilde{d}^k$ ).

Using the formalism developed in [54], the coupling of the  $\tau$  to the  $\tilde{d}^k$  ( $\lambda'_{31k}$ ) and the coupling of the muon to the  $\tilde{d}^k$  ( $\lambda'_{21k}$ ) is given as

$$\frac{|\lambda'_{31k}|^2 - |\lambda'_{21k}|^2}{m^2(\tilde{d}^k)} = 2\sqrt{2}G_F V_{ud} \left[ \frac{2m_\mu^2}{m_\tau^2} \frac{B(\tau^- \rightarrow h^- \nu_\tau)}{H_\pi} - 1 - \frac{H_K}{H_\pi} \right].$$

where  $k$  is an index indicating the lepton generation. Making the assumption that only one coupling is non-zero leads to the following 95% confidence level limits, calculated using  $m(\tilde{d}^k) = 100$  GeV, of

$$|\lambda'_{31k}| < 0.15 \quad \text{and} \quad |\lambda'_{21k}| < 0.09$$

using the OPAL  $\tau^- \rightarrow h^- \nu_\tau$  and tau lifetime [51] measurements and

$$|\lambda'_{31k}| < 0.09 \quad \text{and} \quad |\lambda'_{21k}| < 0.07$$

using the world average  $\tau^- \rightarrow h^- \nu_\tau$  branching ratio and tau lifetime. The limit on  $\lambda'_{21k}$  set using this method is competitive with the present best limit derived from pion decay to electrons and muons [54]. Limits on  $\lambda'_{31k}$  have been obtained previously using the decay  $\tau^- \rightarrow \pi^- \nu_\tau$  [53]. Our new calculation using  $\tau^- \rightarrow h^- \nu_\tau$  has several advantages over this method. Firstly,  $B(\tau^- \rightarrow h^- \nu_\tau)$  is more precisely known than  $B(\tau^- \rightarrow \pi^- \nu_\tau)$ . Additionally,  $B(\tau^- \rightarrow h^- \nu_\tau)$  is a directly measured quantity making the limits more experimentally compelling than those derived from  $\tau^- \rightarrow \pi^- \nu_\tau$ .

---

$S$  is the spin.

The  $\tau^- \rightarrow h^- \pi^0 \nu_\tau$  branching ratio is measured to be  $(25.89 \pm 0.17 \pm 0.29) \%$  and is compared to other published branching ratios in figure 9.1. Some of the branching ratios shown have been corrected by the PDG in order to treat the kaon backgrounds in a uniform manner. The  $\tau^- \rightarrow h^- \pi^0 \nu_\tau$  branching ratio result measured in this work agrees well with the PDG average  $(25.76 \pm 0.15\%)$  and the previous measurements.

The Conserved Vector Current hypothesis [9] can be used to predict the  $\tau^- \rightarrow \pi^- \pi^0 \nu_\tau$  branching ratio from low energy  $e^+e^- \rightarrow \pi^+\pi^-$  data. A number of predictions for the  $\tau^- \rightarrow \pi^- \pi^0 \nu_\tau$  branching ratio have been made [55, 10]. A recent review by Eidelman and Ivanchenko [56] predicted the branching ratio to be  $(24.25 \pm 0.77)\%$ . The  $\tau^- \rightarrow h^- \pi^0 \nu_\tau$  branching ratio measured in this work can be compared to the CVC prediction by subtracting the  $\tau^- \rightarrow K^- \pi^0 \nu_\tau$  branching ratio [2] giving a  $\tau^- \rightarrow \pi^- \pi^0 \nu_\tau$  branching ratio of  $(25.73 \pm 0.31)\%$ . The result measured here is consistent (within two standard deviations) with the CVC prediction.

The  $\tau^- \rightarrow h^- \geq 2\pi^0 \nu_\tau$  branching ratio is measured to be  $(9.91 \pm 0.31 \pm 0.27) \%$ , which is in good agreement with the PDG average for the  $\tau^- \rightarrow h^- \geq 2\pi^0 \nu_\tau$  branching ratio of  $(10.47 \pm 0.35)\%$  [2]. The PDG number quoted is the sum of the average values for the branching ratios of the tau decay to the  $h^- 2\pi^0 \nu_\tau$ ,  $h^- 3\pi^0 \nu_\tau$ ,  $h^- 4\pi^0 \nu_\tau$ ,  $\pi^- \bar{K}^0 \nu_\tau$  and  $K^- \bar{K}^0 \nu_\tau$  modes.

# Chapter 10

## Conclusions

The branching ratios of  $\tau^- \rightarrow h^- \nu_\tau$ ,  $\tau^- \rightarrow h^- \pi^0 \nu_\tau$  and  $\tau^- \rightarrow h^- \geq 2\pi^0 \nu_\tau$  decays have been measured with the OPAL detector at LEP. The branching ratios are

$$\begin{aligned} \text{B}(\tau^- \rightarrow h^- \nu_\tau) &= (11.98 \pm 0.13 \pm 0.16) \% \\ \text{B}(\tau^- \rightarrow h^- \pi^0 \nu_\tau) &= (25.89 \pm 0.17 \pm 0.29) \% \\ \text{B}(\tau^- \rightarrow h^- \geq 2\pi^0 \nu_\tau) &= (9.91 \pm 0.31 \pm 0.27) \% \end{aligned}$$

where the first error is statistical and the second error is systematic. The precision of these measurements is better than previous OPAL measurements [57] and supersede those results. The previous OPAL results are based on a subset of the data used in this work.

The  $\tau^- \rightarrow h^- \nu_\tau$  branching ratio measured in this work is compared to a recent theoretical prediction and is found to be in good agreement. The ratio of the charged current coupling constants of muons and taus using the  $\tau^- \rightarrow h^- \nu_\tau$  branching ratio is found to be  $g_\mu/g_\tau = (1.018 \pm 0.010)$ , consistent with lepton universality. The  $\tau^- \rightarrow h^- \nu_\tau$  branching ratio is used to place limits on supersymmetric  $R$ -parity violating Yukawa couplings. The limit found here is competitive with other current methods and uses the  $\tau^- \rightarrow h^- \nu_\tau$  branching ratio directly. The  $\tau^- \rightarrow h^- \pi^0 \nu_\tau$  branching ratio found in this work is in good agreement with the previous results and also with the

Conserved Vector Current prediction. Finally, the  $\tau^- \rightarrow h^- \geq 2\pi^0 \nu_\tau$  branching ratio measured in this work is found to be 1.2 standard deviations below the current PDG world average.

# Bibliography

- [1] S. L. Glashow, *Nucl. Phys.*, **22** (1961), p.579.  
S. Weinberg, *Phys. Rev. Lett.*, **19** (1967), p.1264.  
A. Salam in Elementary Particle Theory.  
ed. N. Svartholm. (Almqvist and Wiksell, Stockholm, 1968).
- [2] The Particle Data Group, R. M. Barnett *et al.*, *Phys. Rev.* **D54** (1996).
- [3] CDF Collab., F. Abe *et al.*, FERMILAB-PUB-97-284-E (1997).  
D0 Collab., S. Abachi *et al.*, *Phys. Rev. Lett.* **79** (1997) 1197.
- [4] The LEP Electroweak Working Group and the SLD Heavy Flavour Working Group,  
A combination of Preliminary Electroweak Measurements and Constraints on the Standard Model. CERN-PPE/97-154, (1997)
- [5] G. Arnison *et al.*, *Phys. Lett.*, 122B (1983), p.103.  
M. Banner *et al.*, *Phys. Lett.*, 122B (1983), p.476.
- [6] G. Arnison *et al.*, *Phys. Lett.*, 126B (1983), p.398.  
P. Bagnaia *et al.*, *Phys. Lett.*, 129B (1983), p.130.
- [7] P. W. Higgs, *Phys. Lett.* , **12** (1964), p.132.  
*Phys. Rev. Lett.*, **13** (1964), p.508.  
*Phys. Rev.*, **145** (1966), p.1156.
- [8] M. Kobayashi and T. Maskawa, *Prog. Theor. Phys.*, **49**, (1973), p.652.  
N. Cabibbo, *Phys. Rev. Lett.*, **10**, (1963), p.531.
- [9] R. Feynman and M. Gell-Mann, *Phys. Rev.* **109** (1958) p.103.
- [10] Yung-Su Tsai, *Phys. Rev.* **D4** (1971) p.2821.  
F. J. Gilman and S.H. Rhie, *Phys. Rev.* **D31** (1985) p.1066.  
S. I. Eidelman and V. N. Ivanchenko, *Phys. Lett.* **B257** (1991) p.437.  
W. J. Marciano, *Phys. Rev.* **D45** (1992) p.721.  
R. J. Sobie, *Z. Phys.* **C65** (1995) p.79.



- [11] R. Decker and M. Finkemeier, *Phys. Lett.* **B316** (1993) p.403.  
R. Decker and M. Finkemeier, *Phys. Lett.* **B334** (1994) p.199.
- [12] The ALEPH Collab., D. Decamp *et al.*, *Nucl. Instr. Meth.* **A294** (1990) p.121.
- [13] The DELPHI Collab., *Nucl. Instr. Meth.* **A303** (1991) p.233.
- [14] The L3 Collab., B. Adeva *et al.*, *Nucl. Instr. Meth.* **A289** (1990) p.35.
- [15] F. J. Hasert *et al.*, *Phys. Lett.* **46B** (1973) p.138.  
F. J. Hasert *et al.*, *Nucl. Phys.* **B73** (1974) p.1.
- [16] J. P. Delahaye, A. Krusche, CERN-LEP-NOTE-408, (1982).
- [17] L. Knudsen *et al.*, *Phys. Lett.*, **B270** (1991), p.97.  
L. Arnaudon *et al.*, *Phys. Lett.*, **B284** (1992), p.431.
- [18] OPAL Collab., K. Ahmet *et al.*, *Nucl. Instrum. and Meth.* **A305** (1991) p.275.
- [19] P. P. Allport *et al.*, *Nucl. Instrum. and Meth.* **A324** (1993) p.34.  
P. P. Allport *et al.*, *Nucl. Instrum. and Meth.* **A346** (1994) p.476.
- [20] A. Ji-Gang *et al.*, *Nucl. Instr. and Meth.*, **A267** (1988), p.386.  
A. Ji-Gang *et al.*, *Nucl. Instr. and Meth.*, **A267** (1988), p.396.
- [21] J. R. Carter *et al.*, *Nucl. Instr. and Meth.*, **A286** (1990), p.99.
- [22] M. Hauschild *et al.*, *Nucl. Instrum. and Meth.* **A314** (1992) p.74.
- [23] H. A. Bethe and W. Heitler, *Proc. Roy. Soc.* **A146** (1934), p.83.  
D. Perkins, *Introduction to high energy physics*, (3rd ed.)  
(Addison-Wesley Publishing Company. Menlo Park, 1987).
- [24] G. Battistoni *et al.*, *Nucl. Instrum. and Meth.* **164** (1979) 57.
- [25] SF57 lead glass from Schott Glaswerke, Germany.  
Properties: 75% by weight PbO, density  $5.54 \text{ g cm}^{-3}$ ,  $X_0 = 1.50 \text{ cm}$  and refractive index 1.8467 at 586 nm.
- [26] CEREN-25 lead glass, from Corning France.  
Properties: 55% by weight PbO, density  $4.06 \text{ g cm}^{-3}$ ,  $X_0 = 2.51 \text{ cm}$  and refractive index 1.708 at 400 nm.
- [27] Ping Hu. "A Study of the Response of the OPAL Calorimeter to Hadrons",  
MSc Thesis, University of Victoria, (1995).
- [28] D. C. Imrie *et al.*, *Nucl. Instrum. Meth.* **A283** (1989) p.515.

- [29] The OPAL Si-W group, B.E. Anderson *et al.*, *IEEE Trans. Nucl. Sci.* **41** (1994) p.845.
- [30] S. Jadach, B.F.L. Ward and Z. Wąs, *Comp. Phys. Comm.* **79** (1994) p.503.
- [31] S. Jadach, Z. Wąs, R. Decker and J. H. Kühn, *Comp. Phys. Comm.* **76** (1993) p.361.
- [32] J. Allison *et al.*, *Nucl. Instrum. and Meth.* **A317** (1992) p.47.
- [33] R. Brun *et al.*, GEANT 3, Report DD/EE/84-1, CERN (1989).
- [34] A. Buijss. “The OPAL DST (OD) processor in ROPE”, OPAL publication 16/OFFL-0318, 1994.
- [35] P. Poffenberger, “Arrays for Reweighting the Dynamics of Monte Carlo Generated tau to 3pi nu-tau Decays.” OPAL **TN526**, 1997.
- [36] OPAL Collab., G. Alexander *et al.*, *Z. Phys.* **C52** (1991) p.175.
- [37] T. Tsukamoto. “Tau pair analysis in 1990” OPAL **TN026**, 1990.
- [38] OPAL Collab., G. Alexander *et al.*, *Phys. Lett.* **B369** (1996) p.163.
- [39] R. J. Sobie. Private Communication.
- [40] OPAL Collab., G. Alexander *et al.*, *Z. Phys.* **C70** (1996) p.357.
- [41] U. Amaldi, *Physica Scripta*, **23** (1981), p.409.
- [42] G. Nilsson *et al.*, *Nuc. Phys.*, **B195** (1982), p.203.
- [43] A. Astbury, R. Keeler, P. Poffenberger, R. Sobie and M. Vincter. “A New Clustering Algorithm for  $\tau$  decays.” OPAL **TN139**, 1993.
- [44] R. Sobie. “A New Clustering Algorithm for  $\tau$  decays: II.” OPAL **TN186**, 1993.
- [45] R. L. Carrington *et al.* *Nucl. Instrum. and Meth.*, **163**, (1979), p.203.
- [46] The OPAL collaboration, “Analysis of the decay  $\tau^\pm \rightarrow \rho^\pm \nu_\tau$ .” OPAL **PN062**, 1992.
- [47] M. G. Vincter. “A study of the momentum and ECAL energy resolution of the OPAL detector.” OPAL **TN274**. 1995.
- [48] N. Isgur, C. Morningstar and C. Reader, *Phys. Rev.* **D39** (1989) p.1357.
- [49] OPAL Collab., K. Ackerstaff *et al.*, *Z.Phys.* **C75** (1997) p.593.

- [50] CLEO Collab., A. Anastassov *et al.*, *Phys.Rev.* **D55** (1997) p.2559.
- [51] OPAL Collab., G. Alexander *et al.*, *Phys. Lett.* **B374** (1996) p.341.
- [52] J. Ellis, G. L. Fogli, and E. Lisi, *Nucl. Phys.* **B393** (1993) p.3.
- [53] G. Bhattacharyya and D. Choudhury, *Mod. Phys. Lett.* **A10** (1995) p.1699.  
G. Bhattacharyya, “A Brief Review of R-Parity Violating Couplings”, presented at the workshop on Physics Beyond the Standard Model: Beyond the Desert: Accelerator and Nonaccelerator Approaches, Tegernsee, Germany, 8-14 Jun 1997 (Hep-ph/9709395).
- [54] V. Barger, G.F. Giudice and T. Han, *Phys. Rev.* **D40** (1989) p.2987.
- [55] J. H. Kühn and A. Santamaria, *Z. Phys.* **C48** (1990) p.445.
- [56] S. I. Eidelman and V. N. Ivanchenko., *Nucl. Phys. Proc. Suppl.* **55C** (1997) p.181.
- [57] OPAL Collab., G. Alexander *et al.*, *Phys. Lett.* **B328** (1994) p.207.

# Appendix A

## Muon geometry cuts

The muon barrel (MB) detector is used to identify  $\tau^- \rightarrow \mu^- \bar{\nu}_\mu \nu_\tau$  events. The MB detector does not completely cover the barrel region of the OPAL detector. As a result a restricted fiducial region, where the muon detection efficiency of the MB detector is very high and uniform, is defined for this analysis. The regions <sup>1</sup> excluded are:

- $\phi_{\text{MB}} \geq 0.0$  and  $\phi_{\text{MB}} < 60.0$  and  $|\cos \theta_{\text{MB}}| > 0.67$ ;
- $\phi_{\text{MB}} \geq 60.0$  and  $\phi_{\text{MB}} < 125.0$  and  $|\cos \theta_{\text{MB}}| > 0.48$ ;
- $\phi_{\text{MB}} \geq 125.0$  and  $\phi_{\text{MB}} < 205.0$  and  $|\cos \theta_{\text{MB}}| > 0.67$ ;
- $\phi_{\text{MB}} \geq 205.0$  and  $\phi_{\text{MB}} < 237.0$  and  $|\cos \theta_{\text{MB}}| > 0.61$ ;
- $\phi_{\text{MB}} \geq 237.0$  and  $\phi_{\text{MB}} < 303.0$  and  $|\cos \theta_{\text{MB}}| > 0.43$ ;
- $\phi_{\text{MB}} \geq 303.0$  and  $\phi_{\text{MB}} < 342.0$  and  $|\cos \theta_{\text{MB}}| > 0.41$ ;
- $\phi_{\text{MB}} \geq 342.0$  and  $\phi_{\text{MB}} < 360.0$  and  $|\cos \theta_{\text{MB}}| > 0.67$ ;

---

<sup>1</sup> $\cos \theta_{\text{MB}}, \phi_{\text{MB}}$  are respectively the  $\theta$  and  $\phi$  of a track extrapolated to the MB inner face.

These cuts remove approximately 22.4% of the MB acceptance.

In addition, there are inactive regions in the MB chambers where there are internal support structures. Each chamber subtends  $13^\circ$  in the  $r - \phi$  plane so that these inactive regions are removed by requiring that

$$0.0^\circ < \text{mod}(\phi_{\text{MB}}, 13.0^\circ) < 10.5^\circ$$

$$12.5^\circ < \text{mod}(\phi_{\text{MB}}, 13.0^\circ) < 13.0^\circ$$

in the barrel region ( $|\cos \theta| < 0.67$ ) of the OPAL detector. The MB chamber configuration is different at the two vertical locations so these cuts are not applied in these regions.

# Appendix B

## Background estimate

The  $\tau^- \rightarrow e^- \bar{\nu}_e \nu_\tau$  and  $\tau^- \rightarrow \mu^- \bar{\nu}_\mu \nu_\tau$  backgrounds are measured in each selection. These backgrounds are measured using data and Monte Carlo distributions unused in any of the selections. The backgrounds are isolated in a region of these distributions and any difference between data and Monte Carlo is used as a correction factor.

### B.1 $\tau^- \rightarrow e^- \bar{\nu}_e \nu_\tau$ background correction factor

The  $\tau^- \rightarrow e^- \bar{\nu}_e \nu_\tau$  background is measured in all three selections using the  $dE/dx$  distribution. Figure B.1 shows the  $dE/dx$  distributions for jets in the  $\tau^- \rightarrow h^- \nu_\tau$  and  $\tau^- \rightarrow h^- \geq 2\pi^0 \nu_\tau$  samples, the  $dE/dx$  distribution for the  $\tau^- \rightarrow h^- \pi^0 \nu_\tau$  sample is shown in figure 7.4. The momentum of the electrons in this background is relatively low, therefore a requirement that the primary track momentum is less than 5 GeV is placed on each jet used in these measurements. The Monte Carlo distributions in figures B.1 (a) and (b) and 7.4 are normalized to the number of jets in data.

It can be seen that  $dE/dx$  is well modelled in these distributions except that the data shows differences in the right hand peaks ( $\tau^- \rightarrow e^- \bar{\nu}_e \nu_\tau$  background dominated region). The  $\tau^- \rightarrow e^- \bar{\nu}_e \nu_\tau$  background is measured in the right-hand peak ( $9.25 \leq dE/dx \leq 12.0 \text{ keVcm}^{-1}$ ) of the distributions in figures B.1 (a) and (b) and 7.4. The

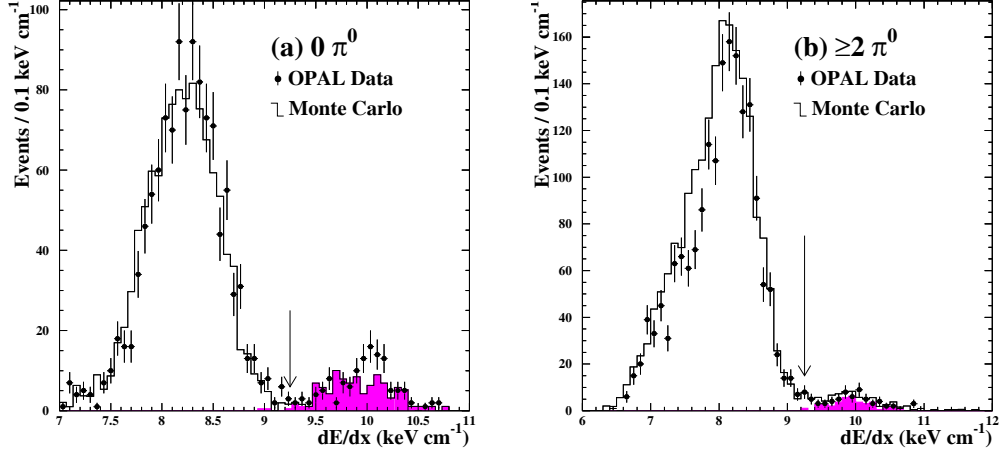


Figure B.1:  $dE/dx$  distribution used to measure the  $\tau^- \rightarrow e^- \bar{\nu}_e \nu_\tau$  background in the  $\tau^- \rightarrow h^- \nu_\tau$  (a) and  $\tau^- \rightarrow h^- \geq 2\pi^0 \nu_\tau$  (b) samples. The primary track of the jets in these samples have momentum less than 5 GeV. The shaded area corresponds to the  $\tau^- \rightarrow e^- \bar{\nu}_e \nu_\tau$  background.

total number of Monte Carlo jets in this region is  $N_{\text{total}}^{\text{MC}}$  where

$$N_{\text{total}}^{\text{MC}} = N_{\text{other}}^{\text{MC}} + N_{e^-}^{\text{MC}}$$

and  $N_{e^-}^{\text{MC}}$  ( $N_{\text{other}}^{\text{MC}}$ ) is the number of  $\tau^- \rightarrow e^- \bar{\nu}_e \nu_\tau$  (other) jets. The number of data jets is  $N_{\text{total}}^{\text{data}}$ . Assuming that the modelling of the “other” jets is good, then we have

$$N_{e^-}^{\text{data}} = N_{\text{total}}^{\text{data}} - N_{\text{other}}^{\text{MC}}. \quad (\text{B.1})$$

The number of  $\tau^- \rightarrow e^- \bar{\nu}_e \nu_\tau$  background jets in data is expressed as

$$R = \frac{N_{e^-}^{\text{data}}}{N_{e^-}^{\text{MC}}} = \frac{N_{\text{total}}^{\text{data}} - N_{\text{other}}^{\text{MC}}}{N_{e^-}^{\text{MC}}} \quad (\text{B.2})$$

where  $R$  is the *correction factor*. Table B.1 gives the values of  $N_{\text{other}}^{\text{MC}}$ ,  $N_{e^-}^{\text{MC}}$  and  $N_{\text{total}}^{\text{data}}$  used to calculate the  $\tau^- \rightarrow e^- \bar{\nu}_e \nu_\tau$  correction factor in each sample.

Variable	$\tau^- \rightarrow h^- \nu_\tau$	$\tau^- \rightarrow h^- \pi^0 \nu_\tau$	$\tau^- \rightarrow h^- \geq 2\pi^0 \nu_\tau$
$N_{\text{total}}^{\text{data}}$	$129.00 \pm 11.36$	$539.00 \pm 23.22$	$68.00 \pm 8.25$
$N_{\text{total}}^{\text{MC}}$	$100.71 \pm 10.04$	$518.31 \pm 22.77$	$71.57 \pm 8.46$
$N_{e^-}^{\text{MC}}$	$95.27 \pm 9.76$	$477.34 \pm 21.85$	$55.31 \pm 7.44$
$R$	$1.30 \pm 0.18$	$1.04 \pm 0.06$	$0.80 \pm 0.28$

Table B.1: Data and Monte Carlo values used to calculate the  $\tau^- \rightarrow e^- \bar{\nu}_e \nu_\tau$  correction factors.

## B.2 $\tau^- \rightarrow \mu^- \bar{\nu}_\mu \nu_\tau$ background correction factor

### $\tau^- \rightarrow h^- \nu_\tau$ selection

In the  $\tau^- \rightarrow h^- \nu_\tau$  selection  $\tau^- \rightarrow \mu^- \bar{\nu}_\mu \nu_\tau$  background jets are rejected if there is a muon signal ( $N^{\text{MB}} > 0$ ) in the MB detector. An estimate of the  $\tau^- \rightarrow \mu^- \bar{\nu}_\mu \nu_\tau$  background in the  $\tau^- \rightarrow h^- \nu_\tau$  selection is made by studying the *inefficiency* of MB to detect muons.

To measure the  $\tau^- \rightarrow \mu^- \bar{\nu}_\mu \nu_\tau$  background in the  $\tau^- \rightarrow h^- \nu_\tau$  selection a pure sample of  $\tau^- \rightarrow \mu^- \bar{\nu}_\mu \nu_\tau$  jets is created in both data and Monte Carlo by requiring each jet to have:

- Number of good charged tracks per jet equal to 1 and no conversion tracks;
- Track momentum greater than 2.5 GeV;
- Number of neutral clusters equal to zero;
- Acoplanarity between jet and opposite jet in event greater than 0.005;
- Energy associated to charged track less than 0.8 GeV;
- Number of HCAL layers hit equal to 9 and number of hits per layer less than 1.2;



- Muon barrel coverage (see appendix A) is good and  $\text{mod}(\phi_{\text{track}}, 13^\circ) < 10.5^\circ$ .

The purity of this sample is estimated from Monte Carlo to be  $99.73 \pm 0.03\%$ .

Figure B.2 shows the MB response for the muon control sample. The fraction of

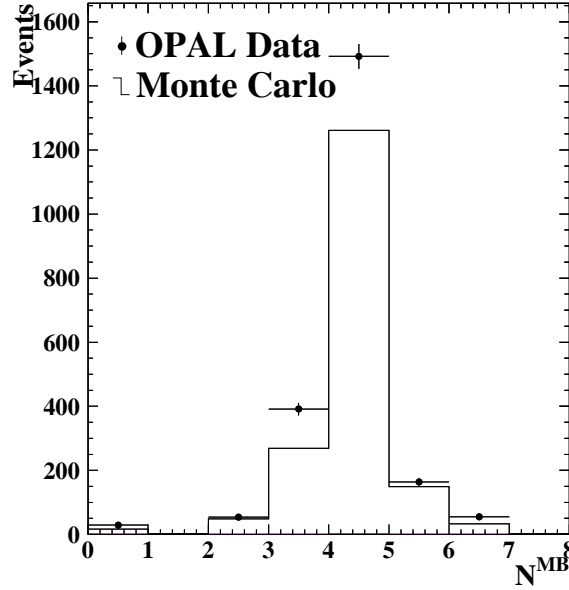


Figure B.2: MB response to the muon control sample used to estimate the  $\tau^- \rightarrow \mu^- \bar{\nu}_\mu \nu_\tau$  correction factor in the  $\tau^- \rightarrow h^- \nu_\tau$  sample.

events with  $N^{\text{MB}} = 0$  is calculated for both the data ( $\epsilon_{\text{data}}$ ) and Monte Carlo ( $\epsilon_{\text{MC}}$ ) muon control samples and

$$\epsilon = \frac{N_\mu^0}{N_\mu}$$

where  $N_\mu^0$  is the number of muon control sample jets that have 0 MB layers hit and  $N_\mu$  is the total number of jets in the muon control sample. A correction factor ( $R$ ) is calculated as

$$R = \frac{\epsilon_{\text{data}}}{\epsilon_{\text{MC}}} \quad (\text{B.3})$$

and is used to quantify the inefficiency of MB to reject  $\tau^- \rightarrow \mu^- \bar{\nu}_\mu \nu_\tau$  jets. The fraction of  $\tau^- \rightarrow \mu^- \bar{\nu}_\mu \nu_\tau$  jets in the data  $\tau^- \rightarrow h^- \nu_\tau$  selection is calculated by multiplying the known  $\tau^- \rightarrow \mu^- \bar{\nu}_\mu \nu_\tau$  contamination from Monte Carlo by  $R$ . Table B.2 gives the numbers used to calculate  $R$  in the  $\tau^- \rightarrow h^- \nu_\tau$  selection.

Variable	Monte Carlo	Data
$N_{\text{MBhits}}^0$	17.04	29
$N_{\text{total}}$	1778.58	2187
$\epsilon$	$0.00960 \pm 0.00231$	$0.0133 \pm 0.00245$
$R$	$1.39 \pm 0.26$	

Table B.2: Values used to calculate  $R$  in the  $\tau^- \rightarrow h^- \nu_\tau$  selection.

### $\tau^- \rightarrow h^- \pi^0 \nu_\tau$ selection

The  $N^{\text{MB}}$  distribution, unused in the  $\tau^- \rightarrow h^- \pi^0 \nu_\tau$  selection, is used to measure the  $\tau^- \rightarrow \mu^- \bar{\nu}_\mu \nu_\tau$  contamination. The  $\tau^- \rightarrow \mu^- \bar{\nu}_\mu \nu_\tau$  background is estimated by studying the efficiency of MB to detect muons within the  $\tau^- \rightarrow h^- \pi^0 \nu_\tau$  selection. The energy of a  $\pi^0$  reconstructed in a  $\tau^- \rightarrow \mu^- \bar{\nu}_\mu \nu_\tau$  jet is typically less than 10 GeV. Therefore the  $\tau^- \rightarrow \mu^- \bar{\nu}_\mu \nu_\tau$  background is studied in  $\tau^- \rightarrow h^- \pi^0 \nu_\tau$  jets where the  $\pi^0$  energy is less than 10 GeV.

A high purity muon control sample cannot be created within the  $\tau^- \rightarrow h^- \pi^0 \nu_\tau$  selection, the best  $\tau^- \rightarrow \mu^- \bar{\nu}_\mu \nu_\tau$  purity that can be achieved is about 50%. The effect of the high hadron content in the muon control sample is corrected by studying the MB response in two control samples. The first sample (hadron sample) has a very low  $\tau^- \rightarrow \mu^- \bar{\nu}_\mu \nu_\tau$  content and is used to study the MB response to hadrons in the Monte Carlo. The second sample (muon sample) has a  $\tau^- \rightarrow \mu^- \bar{\nu}_\mu \nu_\tau$  content of about 50% and studies the MB response to muons.

The data to Monte Carlo ratio for the hadron sample ( $R_1$ ) can be written as

$$R_1 = N_{\pi 1}^{\text{data}} / N_{\pi 1}^{\text{MC}} \quad (\text{B.4})$$

where  $N_{\pi 1}^{\text{data}}$  ( $N_{\pi 1}^{\text{MC}}$ ) is the number of data (Monte Carlo)  $\tau^- \rightarrow h^- \pi^0 \nu_\tau$  jets in this sample. Similarly,  $R_2$ , the data to Monte Carlo ratio for the muon sample can be written as

$$R_2 = \frac{N_{\pi 2}^{\text{data}} + N_{\mu 2}^{\text{data}}}{N_{\pi 2}^{\text{MC}} + N_{\mu 2}^{\text{MC}}} \quad (\text{B.5})$$

where  $N_{\pi 2}^{\text{data}}$  ( $N_{\pi 2}^{\text{MC}}$ ) is the number of data (Monte Carlo)  $\tau^- \rightarrow h^- \pi^0 \nu_\tau$  jets and  $N_{\mu 2}^{\text{data}}$  ( $N_{\mu 2}^{\text{MC}}$ ) is the number of data (Monte Carlo)  $\tau^- \rightarrow \mu^- \bar{\nu}_\mu \nu_\tau$  jets. Equation B.5 can be rewritten with the aid of equation B.4 as

$$R_2 = \frac{R_1 \cdot N_{\pi 2}^{\text{MC}} + R \cdot N_{\mu 2}^{\text{MC}}}{N_{\pi 2}^{\text{MC}} + N_{\mu 2}^{\text{MC}}} \quad (\text{B.6})$$

where ‘‘R’’ is the correction factor between the data and Monte Carlo  $\tau^- \rightarrow \mu^- \bar{\nu}_\mu \nu_\tau$  backgrounds and is solved as

$$R = \frac{R_2 \cdot (N_{\pi 2}^{\text{MC}} + N_{\mu 2}^{\text{MC}}) - R_1 \cdot N_{\pi 2}^{\text{MC}}}{N_{\mu 2}^{\text{MC}}}. \quad (\text{B.7})$$

The hadron sample is created by requiring:

- The primary track muon barrel coverage is good;
- The  $N^{\text{MB}}$  is greater than zero;
- The energy associated to the primary charged track is greater than 0.75 GeV;
- The  $\pi^0$  energy is less than 10 GeV.

These requirements give a hadron sample of 308 jets with a  $4.07 \pm 0.03\%$   $\tau^- \rightarrow \mu^- \bar{\nu}_\mu \nu_\tau$  contamination. Figure B.3(a) shows the MB response to the hadron sample. In

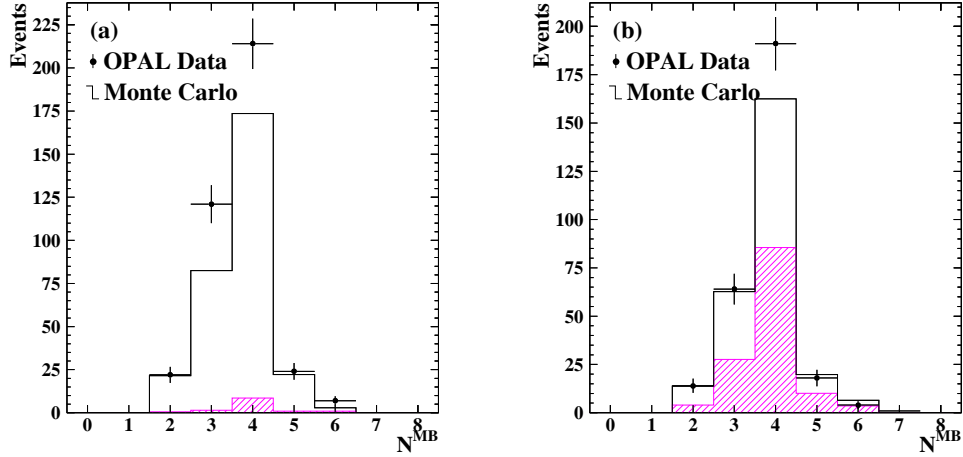


Figure B.3: Figure (a) shows the number of muon barrel layers hit for the  $\tau^- \rightarrow h^- \pi^0 \nu_\tau$  hadron sample. Similarly (b) shows the distribution for the  $\tau^- \rightarrow h^- \pi^0 \nu_\tau$  muon sample. The  $\tau^- \rightarrow \mu^- \bar{\nu}_\mu \nu_\tau$  backgrounds are shown as the dark areas.

figure B.3(a) there are  $302.59 \pm 17.40$  Monte Carlo jets and  $388.00 \pm 19.70$  data jets giving  $R_1 = 1.28 \pm 0.08$ .

The muon sample is created by using the same muon barrel and  $\pi^0$  energy requirements as the hadron sample and requiring energy associated to the charged track to be less than 0.75 GeV. The MB response to the muon sample is shown in figure B.3(b). In figure B.3(b) there are  $265.25 \pm 16.29$  Monte Carlo jets and  $292.00 \pm 17.09$  data jets giving  $R_2 = 1.10 \pm 0.08$ . The  $\tau^- \rightarrow \mu^- \bar{\nu}_\mu \nu_\tau$  background correction factor for the  $\tau^- \rightarrow h^- \pi^0 \nu_\tau$  selection is calculated, using equation B.7, to be  $R = 0.93 \pm 0.26$ .

### $\tau^- \rightarrow h^- \geq 2\pi^0 \nu_\tau$ selection

In the  $\tau^- \rightarrow h^- \geq 2\pi^0 \nu_\tau$  selection the  $\tau^- \rightarrow \mu^- \bar{\nu}_\mu \nu_\tau$  background is negligible ( $0.02 \pm 0.03\%$  and 4 jets). Hence an estimation the  $\tau^- \rightarrow h^- \geq 2\pi^0 \nu_\tau$   $\tau^- \rightarrow \mu^- \bar{\nu}_\mu \nu_\tau$  background is not made.

### B.3 $K_L^0$ backgrounds

The  $\tau^- \rightarrow h^- K_L^0 X \nu_\tau$  background in the one-prong sample is primarily  $\tau^- \rightarrow h^- K_L^0 \nu_\tau$  and  $\tau^- \rightarrow h^- K_L^0 \pi^0 \nu_\tau$  decays, where the branching ratios to these modes is  $(0.76 \pm 0.06)\%$  and  $(0.39 \pm 0.06)\%$ , respectively. The efficiency for selecting these decays into the one-prong sample is approximately 99%. These decays appear in all three samples.

The numbers of decays in each sample is shown in Table B.3. In the  $\tau^- \rightarrow h^- \nu_\tau$

Mode	Selection			Total
	$\tau^- \rightarrow h^- \nu_\tau$	$\tau^- \rightarrow h^- \pi^0 \nu_\tau$	$\tau^- \rightarrow h^- \geq 2\pi^0 \nu_\tau$	
$\tau^- \rightarrow h^- K_L^0 \nu_\tau$	403 (604)	480	41	924
$\tau^- \rightarrow h^- K_L^0 \pi^0 \nu_\tau$	60 (110)	619	164	872

Table B.3: The final number of  $\tau^- \rightarrow h^- K_L^0 X \nu_\tau$  decays in each sample.

sample the  $E/p$  removes a significant number of  $\tau^- \rightarrow h^- K_L^0 X \nu_\tau$  decays and the number of decays prior to applying the  $E/p$  cut is shown in brackets. No cuts remove any decays from the  $\tau^- \rightarrow h^- \pi^0 \nu_\tau$  and  $\tau^- \rightarrow h^- \geq 2\pi^0 \nu_\tau$  samples.

The relative distribution of the  $\tau^- \rightarrow h^- K_L^0 X \nu_\tau$  decays between the selections depends on the energy deposited by the hadron in the electromagnetic calorimeter. Similarly for the removal of  $\tau^- \rightarrow h^- K_L^0 X \nu_\tau$  decays from the  $\tau^- \rightarrow h^- \nu_\tau$  sample. We test the modelling of energy deposited by a hadron by creating a pure sample of charged pions. In figure B.4, the momentum, electromagnetic energy and the  $E/p$  spectra are shown. Poor modelling of the electromagnetic calorimeter energy could result in a redistribution of the  $\tau^- \rightarrow h^- K_L^0 X \nu_\tau$  decays from one sample to another. We studied this by varying the contributions of the  $\tau^- \rightarrow h^- K_L^0 \nu_\tau$  channel to the  $\tau^- \rightarrow h^- \nu_\tau$  and  $\tau^- \rightarrow h^- \pi^0 \nu_\tau$  selections by  $\pm 10\%$  and  $\mp 10\%$ , respectively. Also,

the contributions of the  $\tau^- \rightarrow h^- K_L^0 \pi^0 \nu_\tau$  channel to the  $\tau^- \rightarrow h^- \nu_\tau$ ,  $\tau^- \rightarrow h^- \pi^0 \nu_\tau$  and  $\tau^- \rightarrow h^- \geq 2\pi^0 \nu_\tau$  selections are varied by  $\mp 25\%$ ,  $\pm 10\%$  and  $\mp 25\%$ , respectively.

Further the  $E/p$  cut used in the  $\tau^- \rightarrow h^- \nu_\tau$  sample is sensitive to the modelling of the electromagnetic calorimeter energy. As a result a further 10% uncertainty was assigned to the  $\tau^- \rightarrow h^- K_L^0 X \nu_\tau$  background in this sample. The total error on the  $\tau^- \rightarrow h^- K_L^0 X \nu_\tau$  decays in the three samples is shown in Table B.4.

Selection	Base Error	$\tau^- \rightarrow h^- K_L^0 \nu_\tau$ Normalization	$\tau^- \rightarrow h^- K_L^0 \nu_\tau$ Relative	$\tau^- \rightarrow h^- K_L^0 \pi^0 \nu_\tau$ Relative	Total Error
$\tau^- \rightarrow h^- \nu_\tau$	0.03	0.04	0.02	0.02	0.06
$\tau^- \rightarrow h^- \pi^0 \nu_\tau$	0.04	0	0.01	0.06	0.07
$\tau^- \rightarrow h^- \geq 2\pi^0 \nu_\tau$	0.02	0	0.00	0.04	0.04

Table B.4: The various contributions to the  $\tau^- \rightarrow h^- K_L^0 X \nu_\tau$  background systematic error.

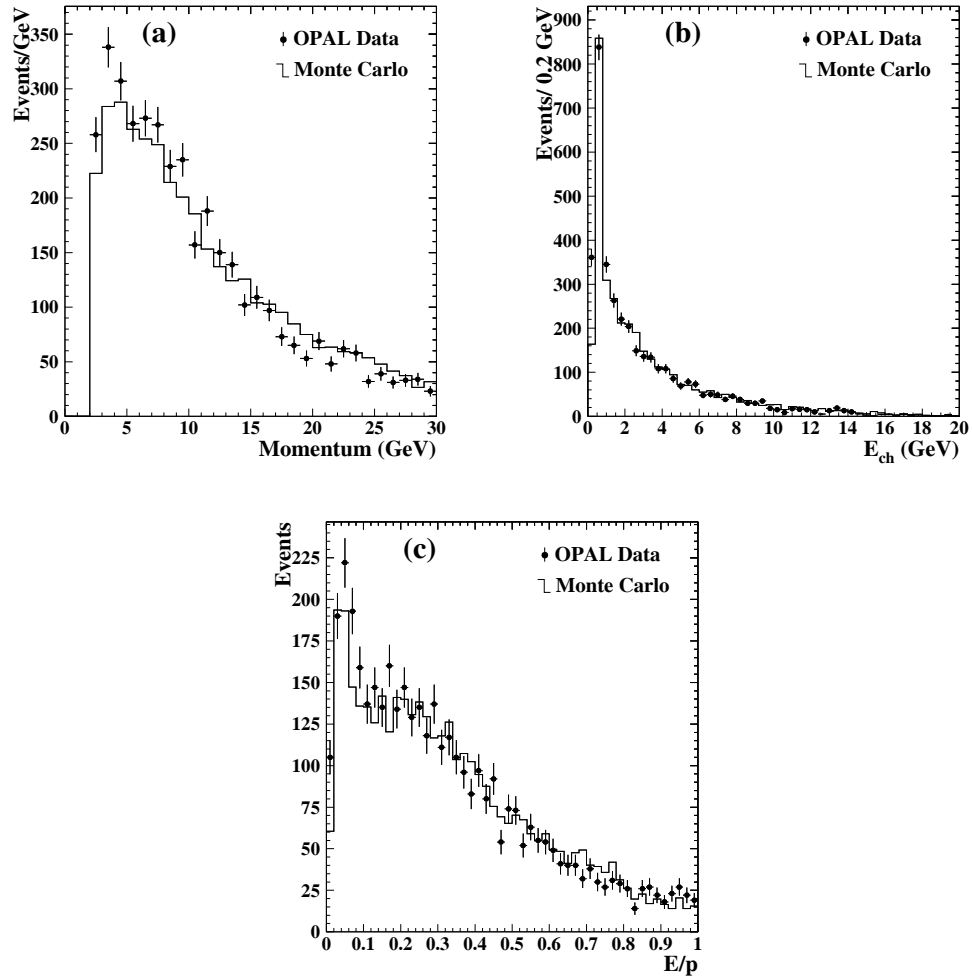


Figure B.4: (a) shows the momentum spectrum of pions in the control sample. (b) shows the electromagnetic calorimeter energy spectrum and (c) shows the  $E/p$  spectrum of pions in the control sample.

# Appendix C

## Bias factor calculation

The  $\tau$  pair selection, discussed in section 4.2, does not select all  $\tau$  decay modes with an equal probability. This leads to a *bias* in the  $\tau$  pair selection to select certain decay modes over others, which is quantified as a set of *bias factors*. The bias factors are calculated from a set of Monte Carlo samples, shown in Table C.1, that include the set used in this analysis (see section 4.1).

Run Number	Detector	$\tau$ events generated
1513	1993	297991 at $E_{CM} = 91.2$ GeV
1515	1993	200000 at $E_{CM} = 89.2$ GeV
1516	1993	200000 at $E_{CM} = 93.2$ GeV
1520	1994	443970 at $E_{CM} = 91.2$ GeV
1536	1994	750000 at $E_{CM} = 91.2$ GeV

Table C.1: The various Monte Carlo samples used in the bias factor calculations.

The Monte Carlo samples 1515 and 1516 are similar to 1513 except that they were generated at different centre-of-mass energies. The Monte Carlo samples 1520 and 1536 use slightly different detector configurations, which were not important for this work, but they use a modified electromagnetic shower algorithm and also have slightly different branching ratios for the decay of the  $\tau$ .



The bias factor of decay mode “ $i$ ” ( $F_i^{\text{bias}}$ ) is defined as

$$F_i^{\text{bias}} \equiv \frac{B_i^{\text{after}}}{B_i^{\text{before}}} \quad (\text{C.1})$$

where  $B_i^{\text{before}}$  ( $B_i^{\text{after}}$ ) is the branching ratio of decay “ $i$ ” before (after) the  $\tau$  pair selection. The branching ratios are defined by equation 8.1 and so equation C.1 can be written as

$$F_i^{\text{bias}} = \frac{N_i^{\text{after}}/N_\tau^{\text{after}}}{N_i^{\text{before}}/N_\tau^{\text{before}}} \quad (\text{C.2})$$

where  $N_i^{\text{after}}$  ( $N_i^{\text{before}}$ ) is the number of decay “ $i$ ” after (before) the  $\tau$  pair selection and  $N_\tau^{\text{after}}$  ( $N_\tau^{\text{before}}$ ) is the total number of  $\tau$ 's after (before) the  $\tau$  pair selection. The uncertainty on the numerator and denominator of equation C.2 is given by the binomial error as

$$\sigma_{B_i} = \sqrt{\frac{B_i(1 - B_i)}{N_\tau}} \quad (\text{C.3})$$

where  $B_i$  is the branching ratio of decay “ $i$ ” and  $N_\tau$  is the total number of  $\tau$ 's used to calculate  $B_i$ . The total statistical error on equation C.2 is calculated using the binomial error of the numerator and denominator.

Studies of the errors on the bias factors using toy Monte Carlo show that the error given in equation C.3 slightly overestimates the true error. This is a result of not including the correlation between the branching ratio in the numerator and the branching ratio in the denominator in equation C.2 when the errors are calculated. A branching ratio calculated from a  $\tau$  pair selected sample of  $\tau$  events ( $B_i^{\text{sel}}$ ) is corrected to the unbiased branching ratio ( $B_i^{\text{true}}$ ) by

$$B_i^{\text{true}} = \frac{B_i^{\text{sel}}}{F_i^{\text{bias}}}.$$

The bias factors from each Monte Carlo in Table C.1 are shown in Table C.2. In

general the results from the five different Monte Carlos are consistent with each other.

An estimate on the systematic variation of each bias factor is made by varying the requirements dependent on the centre-of-mass energy in Monte Carlo 1513. This is achieved by rescaling the centre-of-mass energy in Monte Carlo 1513 by  $\pm 1.0\%$  and recalculating the bias factor for each decay mode. As the centre-of-mass energy is scaled the central values of the Monte Carlo 1513 bias factors move by less than the statistical error value. The bias factors' variation due to energy scaling is small compared to the statistical errors and the the statistical errors on the bias factors given in are considered sufficient to describe the total bias factor errors.

The bias factor for each signal channel, defined in Table 5.1, is calculated as the weighted average of the bias factors that contribute to each signal channel. Table C.3 gives the signal bias factors.

Decay Mode	MC1513	MC1515	MC1516	MC1520	MC1536
$\tau^- \rightarrow e^- \bar{\nu}_e \nu_\tau$	1.002 ± 0.003	.996 ± 0.005	.999 ± 0.005	1.003 ± 0.002	1.004 ± 0.003
$\tau^- \rightarrow \mu^- \bar{\nu}_\mu \nu_\tau$	.988 ± 0.003	.996 ± 0.005	1.024 ± 0.005	.985 ± 0.003	.987 ± 0.003
$\tau^- \rightarrow \pi^- \nu_\tau$	.988 ± 0.004	.993 ± 0.007	.990 ± 0.007	.985 ± 0.003	.991 ± 0.003
$\tau^- \rightarrow \pi^- \pi^0 \nu_\tau$	1.021 ± 0.003	1.016 ± 0.005	1.011 ± 0.005	1.021 ± 0.002	1.019 ± 0.002
$\tau^- \rightarrow \pi^- \pi^+ \pi^- \nu_\tau$	.982 ± 0.004	.978 ± 0.007	.967 ± 0.007	.994 ± 0.003	.990 ± 0.004
$\tau^- \rightarrow \pi^- 2\pi^0 \nu_\tau$	1.015 ± 0.004	1.011 ± 0.007	1.005 ± 0.007	1.014 ± 0.003	1.013 ± 0.004
$\tau^- \rightarrow K^- \nu_\tau$	.986 ± 0.014	.934 ± 0.024	.985 ± 0.024	.996 ± 0.012	1.017 ± 0.012
$\tau^- \rightarrow \pi^- \pi^+ \pi^- \pi^0 \nu_\tau$	.970 ± 0.006	.979 ± 0.010	.953 ± 0.010	.965 ± 0.004	.958 ± 0.005
$\tau^- \rightarrow \pi^- 3\pi^0 \nu_\tau$	1.003 ± 0.011	1.062 ± 0.018	1.038 ± 0.019	1.008 ± 0.007	.998 ± 0.009
$\tau^- \rightarrow 3\pi^- 2\pi^+ \nu_\tau$	.784 ± 0.036	.667 ± 0.058	.771 ± 0.066	.782 ± 0.034	.793 ± 0.040
$\tau^- \rightarrow 3\pi^- 2\pi^+ \pi^0 \nu_\tau$	.733 ± 0.070	.443 ± 0.100	.530 ± 0.098	.805 ± 0.064	.624 ± 0.066
$\tau^- \rightarrow \pi^- \pi^+ \pi^- 2\pi^0 \nu_\tau$	.945 ± 0.018	1.009 ± 0.031	.915 ± 0.031	.945 ± 0.015	.966 ± 0.016
$\tau^- \rightarrow \pi^- \pi^+ \pi^- 3\pi^0 \nu_\tau$	.896 ± 0.076	.880 ± 0.151	.755 ± 0.100	.829 ± 0.042	.928 ± 0.032
$\tau^- \rightarrow K^- 2\pi^0 \nu_\tau$	1.013 ± 0.037	1.125 ± 0.062	1.104 ± 0.077	1.045 ± 0.043	1.042 ± 0.037
$\tau^- \rightarrow K^- \pi^0 K_L^0 \nu_\tau$	.567 ± 0.167	.826 ± 0.308	.933 ± 0.381	.999 ± 0.033	1.026 ± 0.041
$\tau^- \rightarrow K^- \pi^0 K_S^0(2\pi^0) \nu_\tau$	1.474 ± 0.330	.620 ± 0.506	1.866 ± 0.004	1.000 ± 0.062	1.108 ± 0.081
$\tau^- \rightarrow K^- \pi^0 K_S^0(\text{other}) \nu_\tau$	.970 ± 0.211	.465 ± 0.402	1.493 ± 0.334	1.006 ± 0.040	.952 ± 0.051
$\tau^- \rightarrow \pi^- \pi^0 \eta(2\gamma) \nu_\tau$	1.063 ± 0.046	.997 ± 0.079	.953 ± 0.079	1.123 ± 0.038	1.043 ± 0.042
$\tau^- \rightarrow \pi^- \pi^0 \eta(3\pi^0) \nu_\tau$	1.034 ± 0.051	1.012 ± 0.092	.982 ± 0.087	.974 ± 0.040	1.012 ± 0.046
$\tau^- \rightarrow \pi^- K_L^0 K_L^0 \nu_\tau$	.967 ± 0.083	.904 ± 0.153	1.244 ± 0.120	1.066 ± 0.054	.958 ± 0.070
$\tau^- \rightarrow \pi^- K K \nu_\tau$	.917 ± 0.036	.967 ± 0.062	1.226 ± 0.067	1.007 ± 0.023	1.024 ± 0.029
$\tau^- \rightarrow \pi^- \pi^0 K_L^0 \nu_\tau$	1.017 ± 0.022	1.043 ± 0.038	1.009 ± 0.041	1.015 ± 0.030	.979 ± 0.024
$\tau^- \rightarrow \pi^- \pi^0 \gamma \nu_\tau$	1.006 ± 0.048	.976 ± 0.085	.734 ± 0.083	.999 ± 0.039	1.038 ± 0.044
$\tau^- \rightarrow \pi^- \pi^0 K_S^0(2\pi^0) \nu_\tau$	1.086 ± 0.041	1.159 ± 0.069	1.004 ± 0.074	1.152 ± 0.058	1.018 ± 0.043
$\tau^- \rightarrow \pi^- \pi^0 K_S^0(\text{other}) \nu_\tau$	.999 ± 0.026	.940 ± 0.045	1.035 ± 0.045	1.011 ± 0.036	.975 ± 0.029
$\tau^- \rightarrow \pi^- \pi^0 \eta(\text{other}) \nu_\tau$	.992 ± 0.054	.908 ± 0.099	.800 ± 0.085	.956 ± 0.043	.986 ± 0.047
$\tau^- \rightarrow (\pi \pi K)^- \nu_\tau$	.983 ± 0.015	.987 ± 0.028	.967 ± 0.028	.960 ± 0.022	.974 ± 0.017
$\tau^- \rightarrow K^- K_L^0 \nu_\tau$	n/a	n/a	n/a	1.033 ± 0.024	.992 ± 0.038
$\tau^- \rightarrow K^- K_S^0(2\pi^0) \nu_\tau$	n/a	n/a	n/a	1.083 ± 0.046	1.072 ± 0.072
$\tau^- \rightarrow K^- K_S^0(\text{other}) \nu_\tau$	n/a	n/a	n/a	.980 ± 0.030	.968 ± 0.044
$\tau^- \rightarrow K^* \rightarrow K^- \pi^0 \nu_\tau$	1.013 ± 0.017	1.042 ± 0.030	1.033 ± 0.029	.992 ± 0.014	1.012 ± 0.016
$\tau^- \rightarrow K^* \rightarrow \pi^- K_L^0 \nu_\tau$	.993 ± 0.017	.995 ± 0.031	.949 ± 0.032	.996 ± 0.014	.988 ± 0.016
$\tau^- \rightarrow K^* \rightarrow \pi^- K_S^0(2\pi^0) \nu_\tau$	1.073 ± 0.033	.964 ± 0.057	.973 ± 0.064	1.059 ± 0.027	1.049 ± 0.030
$\tau^- \rightarrow K^* \rightarrow \pi^- K_S^0(\text{other}) \nu_\tau$	.987 ± 0.020	1.091 ± 0.035	.862 ± 0.036	1.006 ± 0.017	.951 ± 0.019
$\tau^- \rightarrow \pi^- K_L^0 K_S^0(2\pi^0) \nu_\tau$	1.062 ± 0.095	1.093 ± 0.157	.778 ± 0.266	1.020 ± 0.073	1.043 ± 0.089
$\tau^- \rightarrow \pi^- K_L^0 K_S^0(\text{other}) \nu_\tau$	.913 ± 0.062	.983 ± 0.099	.982 ± 0.107	.976 ± 0.046	1.005 ± 0.055
$\tau^- \rightarrow \pi^- K_S^0(2\pi^0) K_S^0(2\pi^0) \nu_\tau$	1.152 ± 0.315	1.394 ± 0.402	1.866 ± 0.004	.871 ± 0.211	1.266 ± 0.213
$\tau^- \rightarrow \pi^- K_S^0(2\pi^0) K_S^0(\text{other}) \nu_\tau$	1.018 ± 0.105	.929 ± 0.232	1.704 ± 0.110	1.007 ± 0.082	1.036 ± 0.093
$\tau^- \rightarrow \pi^- K_S^0(\text{other}) K_S^0(\text{other}) \nu_\tau$	.757 ± 0.106	1.007 ± 0.189	.564 ± 0.131	.908 ± 0.073	.964 ± 0.099

Table C.2: The bias factors for all decay modes in each Monte Carlo sample. The errors shown are statistical.

Signal Channel	Bias Factor
$\tau^- \rightarrow h^- \nu_\tau$	$0.989 \pm 0.002$
$\tau^- \rightarrow h^- \pi^0 \nu_\tau$	$1.019 \pm 0.001$
$\tau^- \rightarrow h^- \geq 2\pi^0 \nu_\tau$	$1.013 \pm 0.002$

Table C.3: The  $\tau^- \rightarrow h^- \nu_\tau$ ,  $\tau^- \rightarrow h^- \pi^0 \nu_\tau$  and  $\tau^- \rightarrow h^- \geq 2\pi^0 \nu_\tau$  bias factors.

# Appendix D

## Statistical correlations

The branching ratios are solved by

$$[B] = [\epsilon]^{-1}[n]$$

where  $[B]$  is the branching ratio matrix,  $[\epsilon]^{-1}$  is the inverse of the efficiency matrix and  $[n]$  is a matrix that contains the fraction of data selected by each selection. The statistical error matrix between the three branching ratios is given by<sup>1</sup>

$$\begin{bmatrix} \sigma_1^2 & \text{COV}_{12} & \text{COV}_{13} \\ \text{COV}_{12} & \sigma_2^2 & \text{COV}_{23} \\ \text{COV}_{13} & \text{COV}_{23} & \sigma_3^2 \end{bmatrix} = \begin{bmatrix} \frac{\partial B_1}{\partial n_1} & \frac{\partial B_1}{\partial n_2} & \frac{\partial B_1}{\partial n_3} \\ \frac{\partial B_2}{\partial n_1} & \frac{\partial B_2}{\partial n_2} & \frac{\partial B_2}{\partial n_3} \\ \frac{\partial B_3}{\partial n_1} & \frac{\partial B_3}{\partial n_2} & \frac{\partial B_3}{\partial n_3} \end{bmatrix} \begin{bmatrix} \sigma_{n_1}^2 & 0 & 0 \\ 0 & \sigma_{n_2}^2 & 0 \\ 0 & 0 & \sigma_{n_3}^2 \end{bmatrix} \begin{bmatrix} \frac{\partial B_1}{\partial n_1} & \frac{\partial B_2}{\partial n_1} & \frac{\partial B_3}{\partial n_1} \\ \frac{\partial B_1}{\partial n_2} & \frac{\partial B_2}{\partial n_2} & \frac{\partial B_3}{\partial n_2} \\ \frac{\partial B_1}{\partial n_3} & \frac{\partial B_2}{\partial n_3} & \frac{\partial B_3}{\partial n_3} \end{bmatrix} \quad (\text{D.1})$$

where  $\sigma_i$  is the statistical error on branching ratio  $i$ ,  $\text{cov}_{ij}$  is the covariance between branching ratio  $i$  and  $j$ ,  $\sigma_{n_i}$  is the statistical error on fraction  $n_i$  given by equation 8.15 and  $\partial B_i/\partial n_j$  is the uncertainty on branching ratio  $i$  due to fraction  $n_j$ .

The correlation parameter  $\rho_{ij}$  between branching ratios  $i$  and  $j$  is given by

$$\rho_{ij} = \frac{\text{COV}_{ij}}{\sigma_i \sigma_j}.$$

---

<sup>1</sup>See, for example: Lyons, Louis. "Statistics for nuclear and particle physicists." Cambridge University Press, 1986.

The correlation matrix in this analysis is given by

Sample	$\tau^- \rightarrow h^- \pi^0 \nu_\tau$	$\tau^- \rightarrow h^- \geq 2\pi^0 \nu_\tau$
$\tau^- \rightarrow h^- \nu_\tau$	-0.430	0.167
$\tau^- \rightarrow h^- \pi^0 \nu_\tau$		-0.470

Table D.1: The correlation coefficients between each measurement.

# Appendix E

## Error on inverse matrix

The inverse of the efficiency matrix is used to extract the branching ratios. The uncertainty on each inverse efficiency matrix element is needed to evaluate the systematic errors on the branching ratios. These uncertainties are evaluated from the known uncertainties of the efficiency matrix in the following manner.

If we consider an invertible efficiency matrix  $[\epsilon]$  with elements  $\epsilon_{ij} \pm \sigma_{ij}$  then

$$[\epsilon][\epsilon]^{-1} = \mathbf{I} \quad (\text{E.1})$$

where  $[\epsilon]^{-1}$  is the inverse efficiency matrix with elements  $\epsilon_{ij}^{-1} \pm \sigma_{\epsilon_{ij}^{-1}}$  and  $\mathbf{I}$  is the unit matrix. Taking the derivative of both sides of equation E.1 results in

$$\delta[\epsilon][\epsilon]^{-1} + [\epsilon]\delta[\epsilon]^{-1} = [0]$$

that is rearranged as

$$\delta[\epsilon]^{-1} = -([\epsilon]^{-1}\delta[\epsilon][\epsilon]^{-1}) . \quad (\text{E.2})$$

The uncertainty on each element of  $[\epsilon]^{-1}$  ( $\sigma_{\epsilon_{ij}^{-1}}$ ) is given by

$$\sigma_{\epsilon_{ij}^{-1}} = \sum_{a,b} |\epsilon_{ia}^{-1} \delta\epsilon_{ab} \epsilon_{bj}^{-1}|^2 \quad (\text{E.3})$$

where the  $\epsilon_{ij}$  are all uncorrelated. If we make the substitution,  $\delta\epsilon_{ab} = \sigma_{ab}$ , in equation E.3 we get

$$\sigma_{\epsilon_{ij}^{-1}} = \sum_{a,b} |\epsilon_{ia}^{-1} \sigma_{ab} \epsilon_{bj}^{-1}|^2. \quad (\text{E.4})$$

Equation E.4 gives the expression for the uncertainty on element  $\epsilon_{ij}^{-1}$  in terms of the elements of the inverse matrix  $[\epsilon]^{-1}$  and the original uncertainties of matrix  $[\epsilon]$ .

This formula is checked with a simple simulation. Each element of the efficiency matrix ( $\epsilon_{ij}$ ), given in Table E.1, is modified by

$$\epsilon_{ij}^{\text{new}} = \epsilon_{ij} + S \sigma_{ij}$$

where  $\epsilon_{ij}^{\text{new}}$  is the new value of  $\epsilon_{ij}$ ,  $S$  is a gaussian distributed number between  $-1$  and  $1$  and  $\sigma_{ij}$  is the uncertainty on  $\epsilon_{ij}$ . The inverse efficiency matrix is repeatedly

Selection	Selection efficiency from MC		
	$\tau^- \rightarrow h^- \nu_\tau$	$\tau^- \rightarrow h^- \pi^0 \nu_\tau$	$\tau^- \rightarrow h^- \geq 2\pi^0 \nu_\tau$
$0\pi^0$	$0.5502 \pm 0.0024$	$0.1003 \pm 0.0010$	$0.0249 \pm 0.0008$
$1\pi^0$	$0.0455 \pm 0.0010$	$0.5985 \pm 0.0016$	$0.4273 \pm 0.0025$
$\geq 2\pi^0$	$0.0005 \pm 0.0001$	$0.0237 \pm 0.0005$	$0.2730 \pm 0.0023$

Table E.1: The efficiency matrix.

calculated with each element of the efficiency matrix modified independently. The resulting distribution for each element  $\epsilon_{ij}^{-1}$  is plotted in figure E.1.



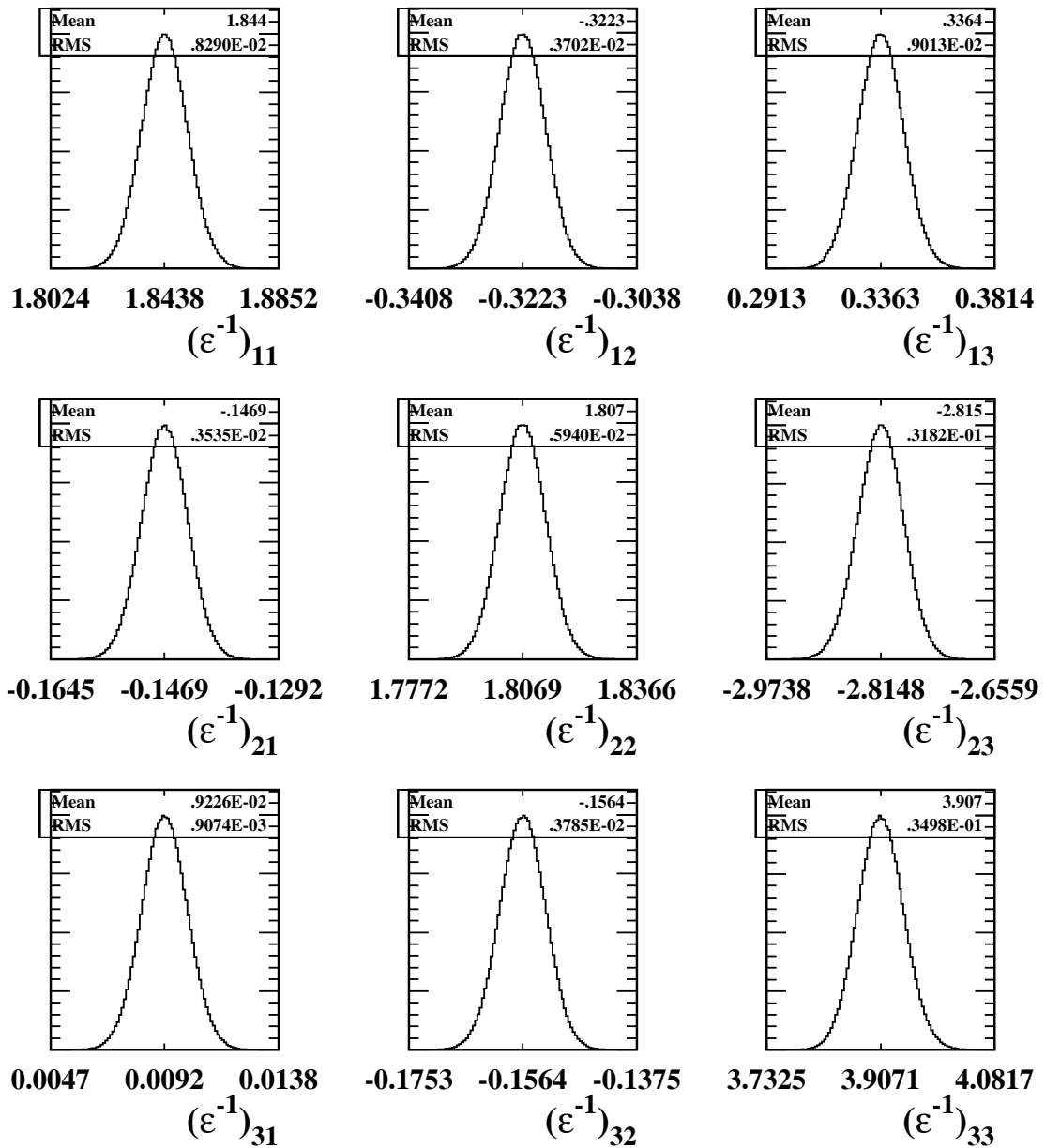


Figure E.1: The individual elements of the inverse efficiency matrix as calculated from the modified efficiency matrix.

The mean values and RMS errors from the histograms in figure E.1 are summarized in Table E.2. The values in Table E.2 can be compared directly with the

Selection	Mean and RMS		
	$\tau^- \rightarrow h^- \nu_\tau$	$\tau^- \rightarrow h^- \pi^0 \nu_\tau$	$\tau^- \rightarrow h^- \geq 2\pi^0 \nu_\tau$
$\tau^- \rightarrow h^- \nu_\tau$	$1.844 \pm 0.008$	$-0.322 \pm 0.004$	$0.336 \pm 0.009$
$\tau^- \rightarrow h^- \pi^0 \nu_\tau$	$-0.147 \pm 0.004$	$1.807 \pm 0.006$	$-2.815 \pm 0.032$
$\tau^- \rightarrow h^- \geq 2\pi^0 \nu_\tau$	$0.009 \pm 0.001$	$-0.156 \pm 0.004$	$3.907 \pm 0.035$

Table E.2: The mean values and RMS errors of the inverse efficiency matrix elements as calculated from the modified efficiency matrix.

inverse of the efficiency matrix, given in Table E.3. The uncertainty on each element in Table E.3 is calculated using equation E.4. The values in Tables E.2 and E.3 are

Selection	Inverse efficiency		
	$\tau^- \rightarrow h^- \nu_\tau$	$\tau^- \rightarrow h^- \pi^0 \nu_\tau$	$\tau^- \rightarrow h^- \geq 2\pi^0 \nu_\tau$
$\tau^- \rightarrow h^- \nu_\tau$	$1.8438 \pm 0.0083$	$-0.3223 \pm 0.0037$	$0.3363 \pm 0.0090$
$\tau^- \rightarrow h^- \pi^0 \nu_\tau$	$-0.1469 \pm 0.0035$	$1.8069 \pm 0.0059$	$-2.8148 \pm 0.0318$
$\tau^- \rightarrow h^- \geq 2\pi^0 \nu_\tau$	$0.0092 \pm 0.0009$	$-0.1564 \pm 0.0038$	$3.9071 \pm 0.0349$

Table E.3: The Inverse of the efficiency matrix.

seen to agree. Therefore it is concluded that equation E.4, that gives the uncertainty on each element of the inverse of the efficiency matrix, is valid.

# Appendix F

## Cut variations

The neutral clusters and the cluster associated to the charged track in each jet are candidates to be  $\pi^0$ 's. Whether these clusters are identified as  $\pi^0$ 's or not depends on the energy of the cluster or pair of clusters. The threshold for a single neutral cluster to be a  $\pi^0$  (one-cluster  $\pi^0$ ) is set nominally at 2.2 GeV. The minimum energy that a  $\pi^0$  reconstructed from a pair of clusters (two-cluster  $\pi^0$ ) can have is set to 3.0 GeV.

By varying the one-cluster and two-cluster  $\pi^0$  thresholds and recalculating the  $\tau^- \rightarrow h^- \nu_\tau$ ,  $\tau^- \rightarrow h^- \pi^0 \nu_\tau$  and  $\tau^- \rightarrow h^- \geq 2\pi^0 \nu_\tau$  branching ratios, their systematic effect can be found. Each threshold is varied independently with the other held at its nominal value and the branching ratios are calculated with the correction factors in Table 7.1 neglected.

Figure F.1 shows the  $\tau^- \rightarrow h^- \nu_\tau$ ,  $\tau^- \rightarrow h^- \pi^0 \nu_\tau$  and  $\tau^- \rightarrow h^- \geq 2\pi^0 \nu_\tau$  branching ratios for various one-cluster  $\pi^0$  energy thresholds. Figure F.2 shows the  $\tau^- \rightarrow h^- \nu_\tau$ ,  $\tau^- \rightarrow h^- \pi^0 \nu_\tau$  and  $\tau^- \rightarrow h^- \geq 2\pi^0 \nu_\tau$  branching ratios for various two-cluster  $\pi^0$  energy thresholds.

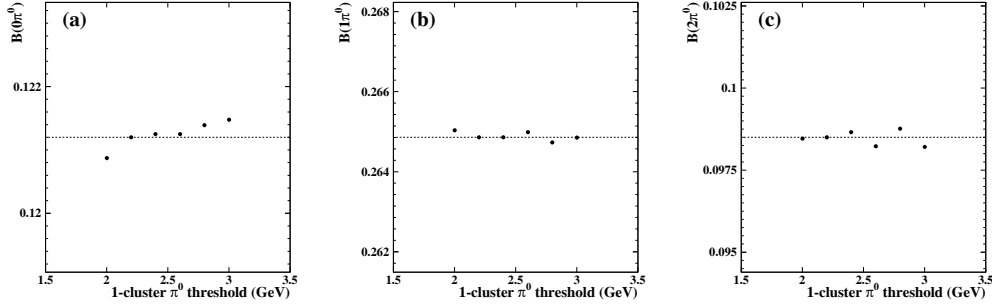


Figure F.1: Figure(a) shows the  $\tau^- \rightarrow h^- \nu_\tau$  branching ratio as a function of the one-cluster  $\pi^0$  energy cut. Similarly figures(b) and (c) show the  $\tau^- \rightarrow h^- \pi^0 \nu_\tau$  and  $\tau^- \rightarrow h^- \geq 2\pi^0 \nu_\tau$  branching ratios as a function of the one-cluster  $\pi^0$  energy cut.

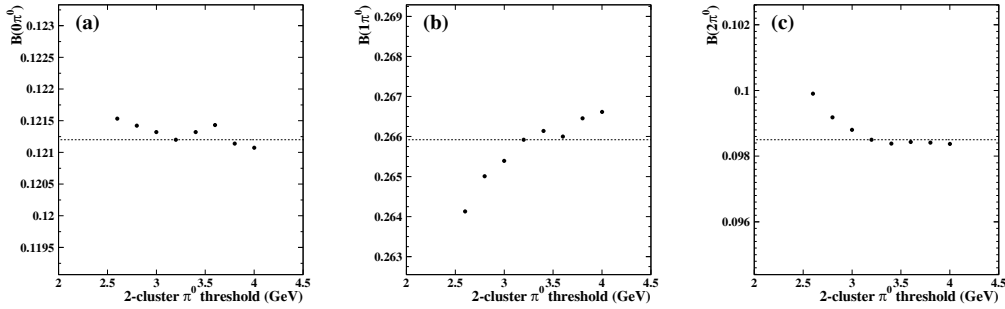


Figure F.2: Figure(a) shows the  $\tau^- \rightarrow h^- \nu_\tau$  branching ratio as a function of the two-cluster  $\pi^0$  energy cut. Similarly figures(b) and (c) show the  $\tau^- \rightarrow h^- \pi^0 \nu_\tau$  and  $\tau^- \rightarrow h^- \geq 2\pi^0 \nu_\tau$  branching ratios as a function of the two-cluster  $\pi^0$  energy cut.

# Appendix G

## Anode plane effects

The cylindrical OPAL jet chamber (CJ) consists of 24 sectors identical in the  $\phi$  direction. Each section subtends  $15^\circ$  in the  $\phi$  direction. Each section is bordered by a plane of cathode wires that run parallel to the beam at increasing radii and constant  $\phi$ . The anode planes consist of staggered wires running parallel to the beam at increasing radii and at constant  $\phi = 7.5^\circ$  within each sector. The ionization charge deposited in the jet chamber gas mixture by charged particles is collected on the wires of the anode plane.

The accuracy of the Monte Carlo simulation of the anode plane is checked by plotting the distribution of charge signed primary tracks within each  $15^\circ$  CJ sector as shown in figure G.1. The difference between Monte Carlo and data for negatively charged tracks can be clearly seen in figure G.1. The effect of this discrepancy is calculated by removing jets with a primary track within a  $0.25^\circ$  region about the anode plane from the selection process. This systematic check resulted in an uncertainty of  $\pm 0.05\%$  for  $B(\tau^- \rightarrow h^- \pi^0 \nu_\tau)$  and  $\pm 0.03\%$  for  $B(\tau^- \rightarrow h^- \geq 2\pi^0 \nu_\tau)$ .

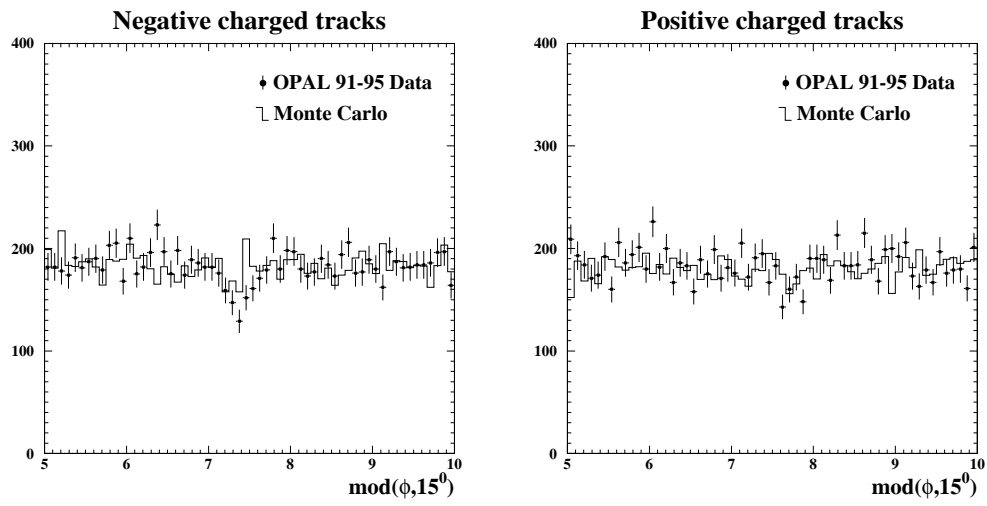


Figure G.1: The  $\phi$  coordinate of all charge signed primary tracks within each CJ sector in each sample.

## Vita

Surname: White  
Given Names: John Stephen  
Place of Birth: Newbury, Berkshire, England  
Date of Birth: 18th of June, 1966

### Educational Institutions Attended:

University of Victoria, Canada 1987-1991

### Degrees Awarded:

B.Sc. (Physics) University of Victoria, Canada 1991  
M.Sc. (Physics) University of Victoria, Canada 1994

### Honours and Awards:

NSERC Scholarship 1991  
NSERC Scholarship 1993

### Publications:

P. Jenni and J. White,  
Physics and Experimental Challenge of Future Hadron Colliders.  
*Proceedings of the 1993 Lake Louise Winter Institute.*,  
held in Lake Louise, Alberta, 21st to 27th of February, 1993.

OPAL Collab., K. Ackerstaff *et al.*,  
Measurement of the one-prong hadronic tau branching ratio at LEP,  
**CERN-PPE/97-152**, Dec 1997. 23pp. submitted to *Z. Phys. C*.

## Partial Copyright License

I hereby grant the right to lend my thesis to users of the University of Victoria Library, and to make single copies only for such users, or in response to a request from the Library of any other university or similar institution, on its behalf or for one of its users. I further agree that permission for extensive copying of this thesis for scholarly purposes may be granted by me or a member of the university designated by me. It is understood that copying or publication of this thesis for financial gain shall not be allowed without my written permission.

Title of Thesis:

**Testing Lepton Universality using One-Prong Hadronic Tau Decays**

Author: John Stephen White

---

---

(Date)